

For Reference

NOT TO BE TAKEN FROM THIS ROOM

Ex LIBRIS
UNIVERSITATIS
ALBERTAENSIS



THE UNIVERSITY OF ALBERTA

CONVERGING FLOW
OF A
VISCOELASTIC FLUID

by




HIN-SUM LAW

A THESIS

SUBMITTED TO THE FACULTY OF GRADUATE STUDIES AND RESEARCH
IN PARTIAL FULFILMENT OF THE REQUIREMENTS FOR THE DEGREE
OF MASTER OF SCIENCE
IN
CHEMICAL ENGINEERING

DEPARTMENT OF CHEMICAL ENGINEERING
EDMONTON, ALBERTA

SPRING, 1977



Digitized by the Internet Archive
in 2023 with funding from
University of Alberta Library

<https://archive.org/details/Law1977>

ABSTRACT

The converging flow patterns obtained when a 0.2% aqueous solution of Separan AP-30 flows from a large reservoir into capillary tubes of 0.2 and 0.3 cm diameter were studied by using a flow visualization technique. Detailed observations of the variation of converging flow patterns with flow rate and tube diameter were made. In addition complete velocity profiles were determined quantitatively at several positions upstream of the entrance.

In common with a number of earlier studies this work shows that the stable converging flow field is in the shape of a wine-glass stem with circulating flows developed in the corner regions. Comparison of the velocity profiles and flow patterns with available models show these to be largely inadequate. The initial cone semi-angle (ϕ_0) was found to be related to the inside diameter of the capillary tube and average flow velocity through the equation:

$$\phi_0 = 64.05 \left(\frac{D^2}{V} \right)^{0.60}$$

The centerline axial velocities within the central core could be expressed as:

$$V_{z,c} = 1.645 \exp \left(-4.04 \left(\frac{D^2}{V} \right)^{0.545} \left(\frac{z}{D} \right) \right)$$

Contrary to earlier studies, the velocity profiles showed considerable development prior to the contraction. At the contraction velocity at the centerline was 95-100% of the centerline velocity for fully developed tube flow.

ACKNOWLEDGEMENTS

The author wishes to acknowledge the assistance given by the following during the course of this work:

Professor Frederick A. Seyer, author's supervisor, for providing the necessary guidance and knowledge to complete this work.

Mr. Peter Catania for several helpful discussions and some of the Figures which had been prepared for his Ph.D. thesis. Also, much of the equipment and technique used in this work had been developed by Mr. Catania prior to the start of this experimental work.

Dr. Shapour Vossoughi for several discussions which were especially helpful.

The staff of the Workshop and the Instrument Shop, for their assistance of the experimental equipment.

Dow Chemical Company which has donated the Separan AP-30 used in this work.

Ms. Daphne Cornelius who typed this thesis.

TABLE OF CONTENTS

CHAPTER		PAGE
	LIST OF TABLES	<i>ix</i>
	LIST OF FIGURES	<i>x</i>
I	INTRODUCTION	1
	I.1 General	1
	I.2 Description of Converging Flow of Visco-elastic Fluids	6
II	THEORY	10
	II.1 Introduction	10
	II.2 Sink Flow Model	10
	II.3 K-1 Model	13
	II.4 Exponential Decay Model	16
III	EXPERIMENTAL EQUIPMENT AND PROCEDURE	19
	III.1 Experimental Apparatus	19
	III.1-1 Entrance Region	19
	III.1-2 Capillary Tubes	19
	III.1-3 Flow System	19
	III.2 Experimental Fluid	21
	III.2-1 Experimental Fluid	21
	III.2-2 Tracer Particles	22

CHAPTER		PAGE
III	III.3 Photographic Techniques	22
	III.3-1 Optical System	22
	a. Light Source	22
	b. Chopping Disc	24
	c. Photographic Assembly	27
	d. Reservoir	28
	III.3-2 Streak Photographs	28
	III.3-3 Analysis of Streak Photographs	32
	a. Local Axial Velocity Measurements	32
	b. Cone Angle Measurements	36
	c. Discussion of Error	36
	III.4 Procedure	39
	III.4-1 Preparation of Polymer Solution	39
	III.4-2 Centering of Capillary Tube	40
	III.4-3 Focusing on the Center of Capillary Tube	40
	III.4-4 Data Collection of Velocity Profiles	41
IV	RESULTS AND DISCUSSIONS	42
	IV.1 Axial Velocity Profiles	42
	IV.2 Cone Angles	53
	IV.2-1 Initial Cone semi-Angles	54
	IV.2-2 Upstream Cone semi-Angles Development	60

CHAPTER		PAGE
IV	IV.3 Central Core Velocities	64
	IV.3-1 Sink Flow Model	67
	IV.3-2 K-1 Model	71
	IV.3-3 Exponential Decay Model	72
V	CONCLUSIONS AND RECOMMENDATIONS	87
	V.1 Conclusions	87
	V.2 Recommendations	88
	NOMENCLATURE	90
	BIBLIOGRAPHY	93
APPENDICES		
A	Calibration of Instron	97
B	Rheological Properties of the Polymer Solution	100
C	Axial Velocity Profiles and Centerline Velocities	109
D	Cone Angles and Central Core Diameters	147
E	Stretch Rates Along Centerline	150
F	Sample Calculation	153

LIST OF TABLES

Table		Page
III-1	Time Intervals for Streak Analysis	25
III-2	Exposure Times and Apertures	27
IV-1	Flow Rates and Axial Locations for Velocity Profiles Measured	43
IV-2	Comparison of Wall Shear Stress at Contraction with Wall Shear Stress of Fully Developed Tube Flow	53
IV-3	Location of Origin for Sink Flow Model	67
IV-4	Parameters of K-1 Model	71
IV-5	Parameters of Exponential Decay Model	80
A-1	Calibration of Flow Rate	97
B-1	Rheological Properties of Standard Oils	105
B-2	Rheological Properties of Polymer Solution	107
C-1	Axial Velocity Data, 0.20 cm I.D. Capillary Tube, $Q = 0.1598 \text{ cm}^3/\text{sec}$	109
C-2	Axial Velocity Data, 0.20 cm I.D. Capillary Tube, $Q = 0.3196 \text{ cm}^3/\text{sec}$	114
C-3	Axial Velocity Data, 0.20 cm I.D. Capillary Tube, $Q = 0.6392 \text{ cm}^3/\text{sec}$	120
C-4	Axial Velocity Data, 0.30 cm I.D. Capillary Tube, $Q = 0.1598 \text{ cm}^3/\text{sec}$	125
C-5	Axial Velocity Data, 0.30 cm I.D. Capillary Tube, $Q = 0.3196 \text{ cm}^3/\text{sec}$	130
C-6	Axial Velocity Data, 0.30 cm I.D. Capillary Tube, $Q = 0.6392 \text{ cm}^3/\text{sec}$	136
C-7	Axial Centerline Velocity Data	144
D-1	Cone Angles and Central Core Diameters	147
E-1	Stretch Rates along Centerline	150

LIST OF FIGURES

Figure		Page
I-1	Free Extension	3
I-2	Velocity Field of the Converging Flow of Viscoelastic Fluid	8
II-1	Coordinate System used in Analysis; Sink Flow Model	11
II-2	Coordinate System used in Analysis; K-1 Model	14
III-1	Capillary Holding Device	20
III-2	Schematic of Optical System	23
III-3	Streak Photograph, 0.20 cm I.D. Capillary Tube, $Q = 0.6392 \text{ cm}^3/\text{sec}$, Extension Tube A	29
III-4	Streak Photograph, 0.20 cm I.D. Capillary Tube, $Q = 0.1598 \text{ cm}^3/\text{sec}$, Extension Tube C	30
III-5	Streak Photograph, 0.30 cm I.D. Capillary Tube, $Q = 0.1598 \text{ cm}^3/\text{sec}$, Extension Tube B	31
III-6	Streak Length along Several Streamlines	34
III-7	Typical Axial Velocity - Position Data	35
IV-1	Axial Velocity Profiles, 0.20 cm I.D. Capillary Tube, $Q = 0.1598 \text{ cm}^3/\text{sec}$	45
IV-2	Axial Velocity Profiles, 0.30 cm I.D. Capillary Tube, $Q = 0.6392 \text{ cm}^3/\text{sec}$	47
IV-3	Axial Centerline Velocity at Contraction versus Average Velocity at Contract	50
IV-4	Wall Shear Stress at Contraction versus Wall Shear Stress of Fully Developed Tube Flow.	52
IV-5	Initial Cone Semi-Angle versus $(D^3/\theta_0 Q)$	55
IV-6	Initial Cone Semi-Angle versus Average Velocity at Contraction	57
IV-7	Initial Cone Semi-Angle versus (D^2/V)	59
IV-8	Upstream Cone Semi-Angle Development; $Q = 0.1598 \text{ cm}^3/\text{sec}$	61

Figure		Page
IV-9	Upstream Cone Semi-Angle Development; Q = 0.3196 cm ³ /sec	62
IV-10	Upstream Cone Semi-Angle Development; Q = 0.6392 cm ³ /sec	63
IV-11	Upstream Cone Semi-Angle Development; K-1 Model; 0.20 cm I.D. Capillary Tube	65
IV-12	Upstream Cone Semi-Angle Development; K-1 Model; 0.30 cm I.D. Capillary Tube	66
IV-13	Centerline Velocity; Sink Flow Model; 0.20 cm I.D. Capillary Tube	69
IV-14	Centerline Velocity; Sink Flow Model; 0.30 cm I.D. Capillary Tube	70
IV-15	Typical Centerline Velocity; K-1 Model	73
IV-16	Typical Centerline Stretch Rate; K-1 Model	74
IV-17	Centerline Velocity; Exponential Decay Model	76
IV-18	Centerline Velocity; Exponential Decay Model	77
IV-19	Typical Axial Velocity; Exponential Decay Model	78
IV-20	Typical Axial Velocity (Metzner et al); Exponential Decay Model	79
IV-21	Parameter Vo of Exponential Decay Model versus Average Velocity at Contraction	81
IV-22	Parameter α of Exponential Decay Model	82
IV-23	Comparison of Centerline Velocity with Exponential Decay Model	84
IV-24	Comparison of Centerline Stretch Rate with Exponential Decay Model	85
A-1	Calibration of Instron Headspeed	98
B-1	Rheological Properties of Standard Oils	103
B-2	Rheological Properties of Separan AP-30, 0.2% (by weight)	104

INTRODUCTION

I.1 General

The converging flow of viscoelastic fluid is of interest in petroleum recovery schemes. In secondary recovery operations, fluid injection is commonly used as an external energy supplying the reservoir in order to recover the oil trapped in the porous rock. This external energy is needed because the initial natural energy in the reservoir such as the gravitational energy due to the difference in hydrostatic level of producing well and upper part of the reservoir will sooner or later be depleted. Polymer flooding is a fairly new fluid displacement technique, which has been shown to be more effective than water flooding to develop a stable high oil saturation zone simply because the polymer solution has higher viscosity than water (52). The mechanism of polymer flooding is not fully understood but is probably related to the flow behaviour of polymer solution in porous media. Actually, the type of flow through porous media is very similar to the converging flow into a capillary tube.

On the other hand, the converging flow of viscoelastic fluid is of interest in many polymer processing operations such as extrusion and fiber spinning. The converging flow is one of the extensional flows since the fluid elements are subjected to large stretching deformations while accelerating into the capillary tube. Extensional flows can be divided into two types as follows:

(i) forced extension

In flow of this type, the shape of the material being extended is forced by the operation being performed. For example, the calendering where the material is forced to conform to the shape of the rollers as it passes through them.

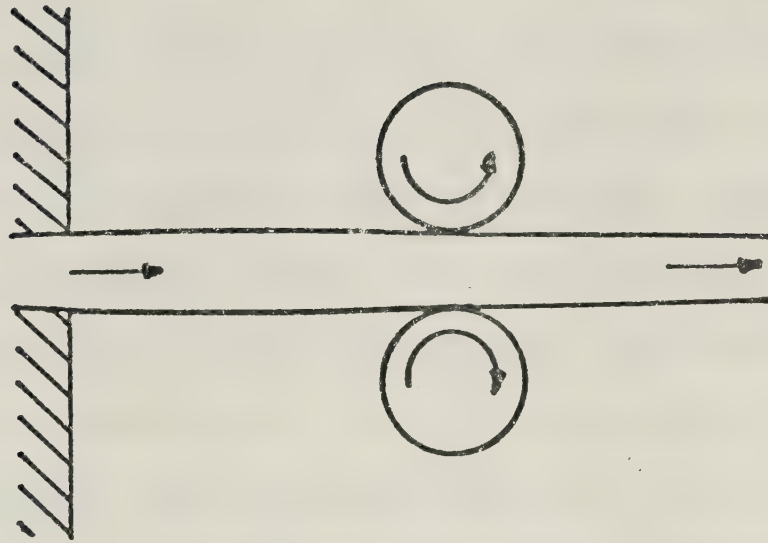
(ii) free extension

In flow of this type the shape of the extending material is not imposed by the operations, and the material chooses its shape subject to internal constraints. More commonly continuous operations involve this type of extension which the material being extended has a lateral interface with a low-viscosity substance or is in lateral contact with portions of the same material which are not undergoing extension. For example, the first case is illustrated in Figure (I-1a) for spinning where the low-viscosity substance is air, and the latter case is illustrated in Figure (I-1b) for extrusion of polymer solutions.

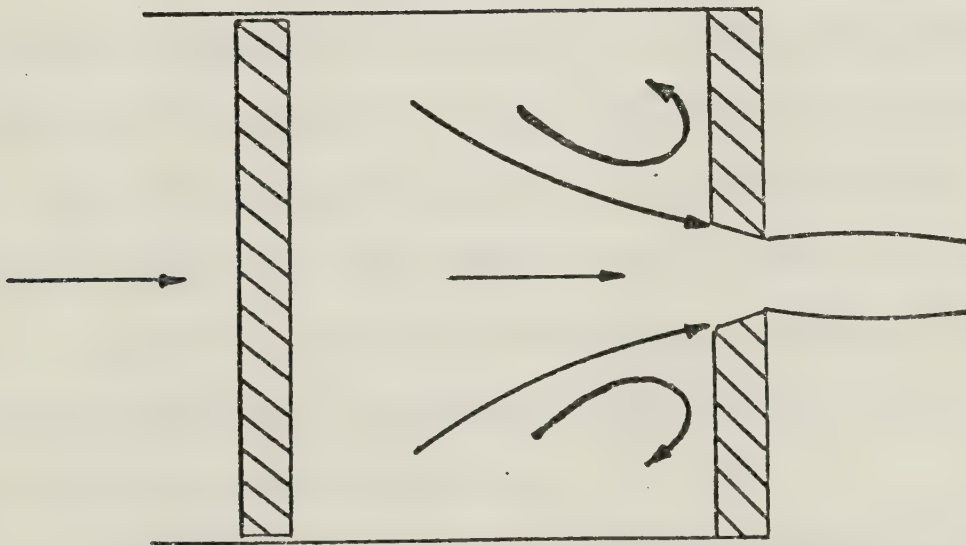
Since the converging flow is in the type of free extension, the experimental results of the converging flow may be similar or have application to fiber spinning and extrusion.

Almost all polymer extension flow problems of interest to the rheologist involve free extension rather than forced extension. The extensional rheology of polymeric fluids has been considered by many investigators such as Balakrishnan and Gordon (4), Balmer (7), Cogswell (13, 14), Denson (17), Kizior and Seyer (29), Metzner and Metzner (31), Murch (33) and Oliver (39) for various types of free extension. These studies include information on the extension viscosity which is defined

FIGURE I-1
FREE EXTENSION



a) Spinning



b) Extrusion

as the axial or normal stress in flow direction divided by the extensional strain rate. The extension viscosity was reported to be as much as a few orders of magnitude greater than the shear viscosity of the polymeric fluids (4, 31, 39).

In the past little attention has been devoted to quantitative measurements of the velocity profiles of the extensional flows and relating these velocities to the parameters such as flow rate, diameter of orifice or capillary tube and axial location along the direction of flow. The major majority of investigations of extensional flow have been concerned with the onset and prediction of flow instabilities because in many polymer processing operations, the rate of production is limited by the onset of flow instabilities. The studies of melt fracture, which is the name given to a gross distortion or waviness of extrudate deformations that are shown by polymer solutions and melts flow through capillaries or slits at output above a certain critical value, were reported by many investigators such as Bagley (2), Ballenger et al (5), Barnett (8), Blyler and Hart (9), den Otter (15), Giesekus (18), Han (22), Hurlimann and Knappe (23), McIntire (30), Pearson and Pickup (40), Rama Murthy (43), Rothenberger, McCoy and Denn (44), Southern and Paul (45), Tomita and Shimbo (46), Tordella (47, 48), Vinogradov and Manin (50) and White (56). Flow visualization techniques were commonly used by almost all of the investigators. In addition, Kase (28) theoretically studied the stability of melt spinning and Petrie and Denn (41) have published review of the instabilities in polymer processing.

A technique of measuring the velocity profiles of molten polymers during laminar flow was first represented by den Otter (16). Velocity profiles were measured for the flow of some polymeric melts

(low density polyethylene, two high density polyethylenes and a polydimethyl siloxane) through a rectangular slit. The velocities were determined by measuring the time needed for a particle to cover a distance of one millimeter with a stopwatch. The velocity profiles measured were in good agreement with those calculated from the flow curves made by assuming a simple power law relationship over the whole shear rate range. The velocities were found to be zero at the wall in all cases even during melt fracture for a low density polyethylene and a polydimethyl siloxane.

Metzner, et al (32) studied the kinematics of a converging velocity field in flow from a large reservoir into a small tube. The velocity profiles were measured photographically by using small air bubbles as tracers. More details of their study will be discussed in the next section.

Kanel (26) had studied the behavior of a viscoelastic fluid in "fiber spinning" and "Fano flows". "Fiber spinning" is a technique where the material is forced through a die at low velocity and is wound up at high velocity at some position downstream from the die. "Fano flow" is a thin column of fluid created by immersing one end of a thin glass tube in a reservoir containing polymer solution while the other end is connected to an evacuated vessel. When the level of the fluid dropped well below the tube end, a thin column of fluid would continue to flow upward and through the tube. By taking photographs of the extensional fluid column and making diameter measurements, Kanel suggested that the extensional flows were characterized by a history parameter P (when $P=1$ it was defined as K-1 model). When two flows have the same value of the parameter P , they were seen to have the same deformation history over time intervals during which they cover the same range of

extension rate. Kenel's (26) data and Weinberger's (54) data which Kenel used, indicated primarily a quadratic dependence of velocity on distance into the fluid column in Fano and fiber spinning flows. However a linear relationship which indicated a homogeneous steady extension was also noted in several instances. The solutions they used were different concentrations of Separan AP-30 in a 50% glycerine - 50% water mixture. In view of the generally high fluid viscosities and the absence of significant shearing due to the low viscosity of the surrounding air, Kanel has assumed a flat velocity profile in his study.

Kase (27) analyzed the velocity field within a molten spinning thread by solving the equations of continuity and momentum for Newtonian fluids. In solving the equations, the viscosity was assumed known. He obtained a solution for the axial velocity which was an exponential function of the axial location. With the same reason as mentioned above, Kase has also assumed a flat velocity profile in his study.

Although the above investigators have considered the velocity profiles within the extensional flow, only one of them (32) has measured the velocity profiles directly. Thus the goal of this study is to measure the velocity field in converging flow from a large reservoir into a small capillary tube. These results may have application to the petroleum recovery schemes and polymer processing operations.

I.2 Description of Converging Flows of Viscoelastic Fluids

A considerable number of experimental investigations have reported on the qualitative behavior of viscoelastic fluids such as molten polymers in capillary rheometers. Results of these investigations have indicated that at low flow rates, the materials show a full 180° convergence with no evidence of secondary flow as a Newtonian fluid does (6,19,43).

In other words, the flow at any point in the reservoir is directed toward the tube entrance. At higher flow rates, circulating flows develop in the corner regions, their size increases as flow rate increases (6, 24, 25, 32, 43). This velocity field of the converging flow of viscoelastic fluid is shown in Figure (I-2). At very high flow rate, a breakdown of this entrance velocity field occurs.

The sink flow model has been used previously to describe the velocity field within the central core for converging flow by Uebler (49) and Metzner, et al (32). In their work, the velocity profiles within the central flow core for 0.5% Separan AP-30 solution, which flowed from an 18" wide square reservoir into a 1.48 in I.D. tube, were measured with flow rates of 457, 915 and 1372 cm³/sec. The extent of the central core as measured by ϕ_0 in Figure (I-2) was 10° to 15° from the extended centerline of the tube. Within this region the streamlines were straight and if extrapolated downstream from the tube entrance, converged to a point on the centerline of the tube. Thus the flow kinematics of a viscoelastic fluid in this geometry was represented as that of a radial flow towards a virtual point sink located downstream from the tube entrance on the centerline of the tube. Uebler's results showed that the radial component of the fluid velocity within the central core was dependent only upon radial position; in other words, no shearing was present in that region.

The initial cone semi-angle (ϕ_0) in Figure (I-2), which is defined as the angle formed by the line tangent to the outermost streamline at the contraction, has been studied by Ballenger and White (6) and Oliver and Bragg (36, 37, 38). Ballenger and White have measured the initial cone semi-angle for the flow of low-density polyethylene, polystyrene, and isotactic polypropylene at 180°C in the reservoir approach

to a capillary extrusion rheometer. Initial cone semi-angle was related to the Weissenberg number which is defined as the ratio of the entrance pressure drop to the capillary wall shear stress. Oliver (36, 37, 38) has measured the initial cone semi-angle for three concentrations of 0.1%, 0.03% and 0.10% ET 597 solutions. Initial cone semi-angle was related to the average velocity of flow through orifice and the radius of the orifice. Cone angles were studied in a 3" wide square reservoir fitted with different orifices of diameters 0.1, 0.2, 0.5, 0.95 and 1.27 cm, and with average velocities of flow through the orifices from 7 to 800 cm/sec.

Even today the important aspect of this converging velocity field such as the dependence of axial velocity on axial location is not fully understood. For example, the flat velocity profile assumed within the central core by Metzner, et al (32) is suspect because of the high viscosity of the circulating region which surrounds the central core. Therefore, a detailed quantitative study of the velocity field of the converging flow of viscoelastic fluid is of interest in this study. In the present study, the velocity profiles, the cone semi-angles, and some rheological properties such as wall shear stress and stretch rate were measured for the converging flow field. This flow field was obtained by a 0.2% Separan AP-30 solution flowed from a 2.64 cm wide square reservoir into different capillary tubes of I.D. 0.20 and 0.30 cm with three different flow rates of 0.1598, 0.3196 and 0.6392 cm³/sec.

CHAPTER II

THEORY

II.1 Introduction

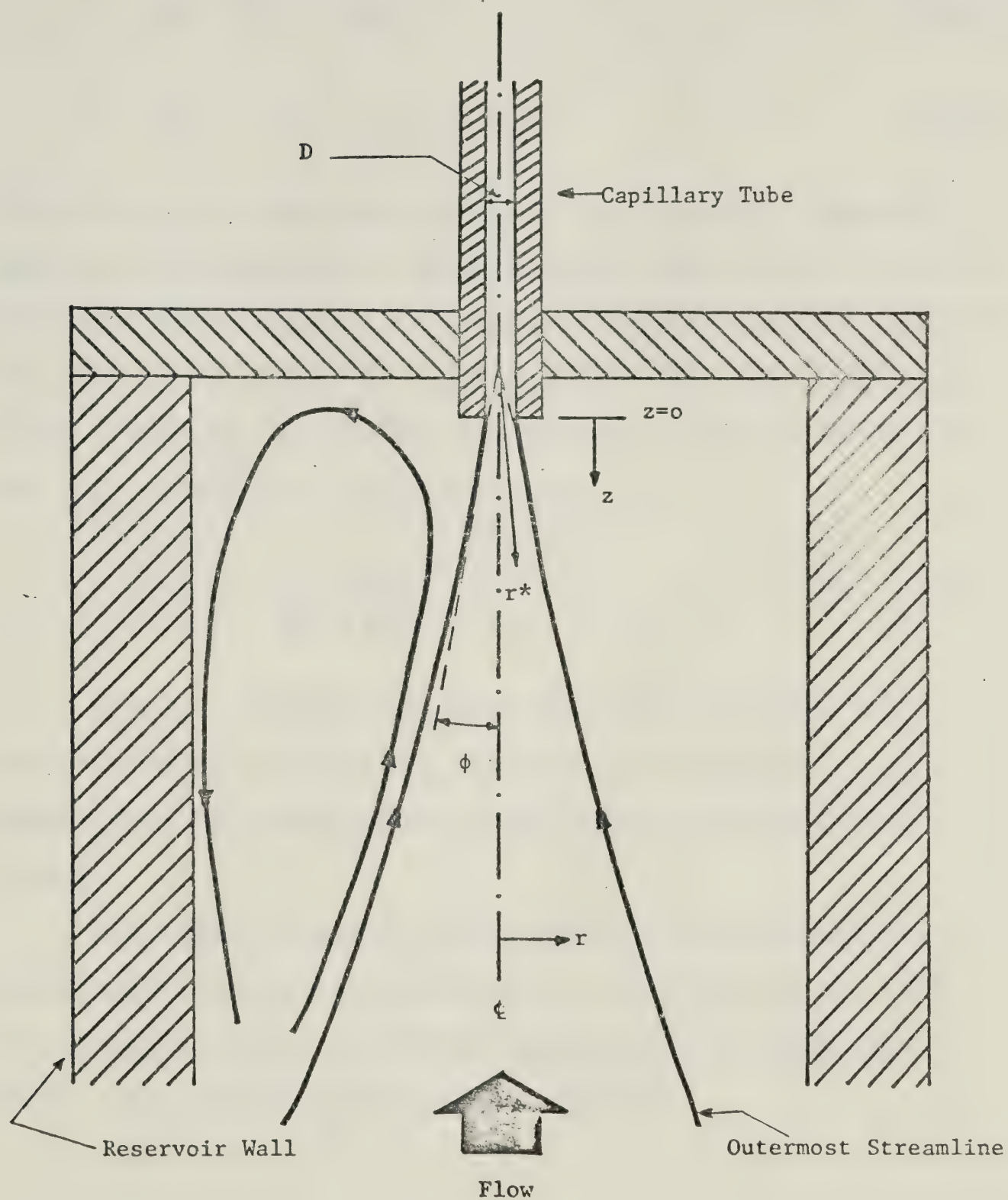
As mentioned in Chapter I, only a few investigators such as Metzner, et al (32), Kanel (26) and Kase (27) had studied the velocity profiles within extensional flow. The sink flow model suggested by Metzner, et al is considered first to analyze the results in this study because the type of converging flow and polymer solutions used in their study were nearly the same as this study. The empirical K-1 model represented by Kanel for "Fano flow" and "fiber spinning", and the exponential decay model represented by Kase for melt spinning are also considered because the shape of "Fano flow" and "melt spinning" are very similar to the shape of the central core in this study. Both of these are free extensions and have the diameter of the fluid column or core decreasing along the direction of flow. These three models will be discussed separately in the following sections.

II.2 Sink Flow Model

The velocity field within the central core can be analyzed employing a spherical polar coordinate system with its origin located downstream on the centerline of the capillary tube at a point determined by extending the converging streamlines to intersection. Distances upstream of this origin are denoted by r^* and the diameter of the capillary tube by D . The coordinate systems used for sink flow model, in analysis of the velocity field are shown in Figure (II-1).

FIGURE II-1

COORDINATE SYSTEMS USED IN ANALYSIS; SINK FLOW MODEL



The continuity equation for a symmetric flow field, in spherical coordinate system, becomes,

$$V_{r^*} r^{*2} = f(\phi) \quad (\text{II-1})$$

$$\text{if, } V_\theta = V_\phi = 0 \quad (\text{II-2})$$

where ϕ is the cone semi-angle, V_θ and V_ϕ are the velocity components in spherical coordinate system. Normalizing the radial velocity (V_{r^*}) with respect to average velocity (V) in the capillary tube and radial position (r^*) with respect to the capillary tube diameter (D), and replacing $f(\phi)$ by the constant Q^* (32, 33) which is proportional to the volumetric flow rate (Q), Equation (II-1) can be written as:

$$\left(\frac{V_{r^*}}{V} \right) = \frac{Q^*}{VD^2} \left(\frac{r^*}{D} \right)^{-2} \quad (\text{II-3})$$

Therefore, on logarithmic coordinates the slope of plot of the dimensionless radial velocity (V_{r^*}/V) versus the dimensionless radial position coordinate (r^*/D), will be equal to -2 if Equation (II-3) is correct.

In the study of Metzner, et al, Equation (II-3) applied to the central region where the cone semi-angle was less than or equal to 10° . In this region, Metzner, et al found that the velocity profiles at several axial locations upstream were nearly flat.

II.3 K-1 Model

By taking photographs of the fluid column in Fano and fiber spinning flows and making diameter measurements, Kanel (26) found that the diameter of the thread was often given by:

$$\frac{1}{d^p} = C_1' z + C_2' \quad (\text{II-4})$$

in which z is the axial position variable in a cylindrical coordinate system, d is the diameter of the fluid column, and p is a parameter. When $p=1$, it is the K-1 model, and Equation (II-4) can be written as:

$$\frac{1}{d} = C_1' z + C_2' \quad (\text{II-5})$$

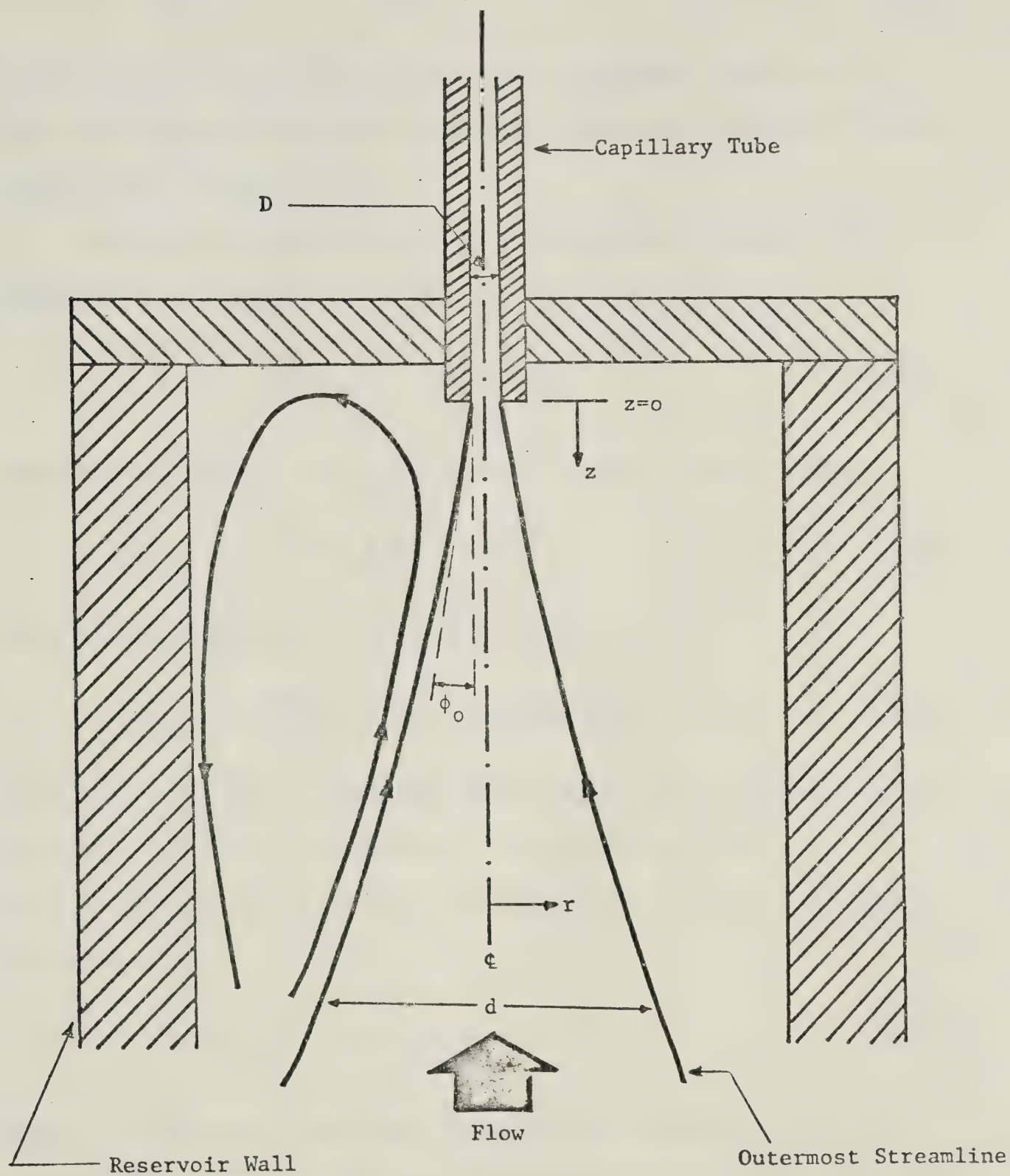
Considering the converging flow through a capillary tube, the axial position (z) can be normalized with respect to the diameter of the capillary tube (D). Then Equation (II-5) becomes:

$$\frac{1}{d} = C_1 \left(\frac{z}{D}\right) + C_2 \quad (\text{II-6})$$

Figure (II-2) shows the coordinate system used for K-1 model in analysis of the velocity field of the converging flow into a capillary tube. From Equation (II-6) and the geometry in Figure (II-2), one can express the slope of the tangent to the outermost streamline at any axial location as;

$$\begin{aligned} \tan \phi &= \frac{d}{dz} \left(\frac{d}{2}\right) \\ &= \frac{-\frac{C_1}{2D}}{\left[C_1 \left(\frac{z}{D}\right) + C_2\right]^2} \\ &= -\frac{C_1}{2D} d^2 \end{aligned} \quad (\text{II-7})$$

FIGURE II-2
 COORDINATE SYSTEM USED IN ANALYSIS; K-1 MODEL



At the contraction ($\frac{z}{D} = 0$), ϕ becomes the initial cone semi-angle (ϕ_0) and d becomes the diameter of the capillary tube (D). Then,

$$\tan \phi_0 = - \frac{C_1 D}{2} \quad (\text{II-8})$$

Equation (II-7) shows that on logarithmic coordinates the slope of a plot of the tangent of the cone semi-angle versus the diameter of central core (d) will be equal to +2.

Based on the flat velocity profile assumption by Kanel, the volumetric flow rate (Q) can be written as,

$$Q = \left(\frac{\pi d^2}{4}\right) V_z = \left(\frac{\pi d^2}{4}\right) V_{z,\zeta} \quad (\text{II-9})$$

Substituting Equation (II-6) into Equation (II-9), and rearranging:

$$V_{z,\zeta} = \frac{4Q}{\pi} [C_1 \left(\frac{z}{D}\right) + C_2]^2 \quad (\text{II-10})$$

Then, expanding Equation (II-10) in the form as:

$$V_{z,\zeta} = \frac{4Q}{\pi} [C_1^2 \left(\frac{z}{D}\right)^2 + 2C_1 C_2 \left(\frac{z}{D}\right) + C_2^2] \quad (\text{II-11})$$

Equation (II-11) shows a quadratic dependence of axial velocity on axial location (32,33), but this Equation is valid only for flat velocity profile. More formally, the volumetric flow rate (Q) can be expressed as:

$$Q = \int_0^{d/2} 2\pi r V_z dr \quad (\text{II-12})$$

where r is the radial coordinate in cylindrical coordinate system as shown in Figure (II-2). If the velocity profile is not flat, the axial velocity (V_z) is a function of the radial location (r) and the dependence (cf II-9) is no longer on d^2 . Therefore Equations (II-10) and (II-11)

are no longer quadratics. However it is still of interest to test whether a quadratic dependence on axial location gives a reasonable fit and an equation similar to (II-11) will be assumed such that:

$$V_{z,c} = K_1 + K_2 \left(\frac{z}{D}\right) + K_3 \left(\frac{z}{D}\right)^2 \quad (\text{II-13})$$

The parameters K_1 , K_2 and K_3 can be found from the least square fit of the centerline velocity data.

Differentiation of Equation (II-13) with respect to axial coordinate (z) shows the linear relationship of the dimensionless axial position coordinate $\left(\frac{z}{D}\right)$ and the stretch rate along the centerline as:

$$V_{z,z,c} = \left(\frac{K_2}{D}\right) + \left(\frac{2K_3}{D}\right) \left(\frac{z}{D}\right) \quad (\text{II-14})$$

II.4 Exponential Decay Model

The velocity field within a melt spinning was analyzed by Kase (27) by solving the Navier-Stokes equations with the following assumptions: (i) steady state; (ii) constant density; (iii) axial symmetry both in temperature and velocity field; (iv) negligible gravity force; (v) negligible inertia forces; (vi) a known temperature profile. With the above assumptions, the viscosity was assumed known and was given by the expressions:

$$\mu = \mu_0 e^{\beta z} (1 + cr^2) \quad (\text{II-15})$$

where z and r are distances in cylindrical coordinates. Substituting this viscosity into the Navier-Stokes equations, a solution of the axial velocity (V_z) have the expression:

$$V_z = V_0 e^{\alpha' z} (1 + a_2 r^2 + a_4 r^4 + a_6 r^6 + \dots) \quad (\text{II-16})$$

where V_0 is assumed independent of r .

The results of Kase showed that the velocity profile across the thread in any melt spinning could be assumed to be flat. In view of the generally high fluid viscosities and the absence of significant shearing, due to the low viscosity of the surrounding air, it would seem to be a reasonable assumption. In other words, it is reasonable to say that the values of $a_2, a_4, a_6 \dots$ are very small compared with unity. Therefore, Equation (II-16) can be written as:

$$V_z = V_0 e^{\alpha' z} \quad (\text{II-17})$$

Although the four parameters V_0, α', μ_0 and β in Equation (II-15) and (II-16) are functions of axial position (z), they can safely be assumed to be constants by Kase in his study (27).

Considering the converging flow through a capillary tube, the axial position (z) can be normalized with respect to the diameter of the capillary tube (D). Then Equation (II-17) becomes:

$$V_z = V_0 e^{\alpha \left(\frac{z}{D}\right)} \quad (\text{II-18})$$

Equation (II-18) shows that on semi-logarithmic coordinates, a plot of the axial velocity (V_z) versus the dimensionless axial location ($\frac{z}{D}$) will be a straight line with slope equal to α and intercept at $\frac{z}{D} = 0$ equal to V_0 .

Differentiation of Equation (II-18) with respect to axial position (z) yields:

$$v_{z,z} = v_o \frac{\alpha}{D} e^{\alpha(\frac{z}{D})} \quad (\text{II-19})$$

Equation (II-19) shows that the stretch rate is an exponential function of the dimensionless axial location ($\frac{z}{D}$).

These three models will be used to analyze the results in this study and will be discussed in Chapter IV.

CHAPTER III

EXPERIMENTAL EQUIPMENT AND PROCEDURE

III.1 Experimental Apparatus

III.1-1 Entrance Region

A reservoir of 2.64 cm internal width and 25.40 cm length was used as the entrance region. The internal length of the reservoir assured that the velocity distribution was fully developed prior to the location of the pressure tap which was located 10.20 cm from the anodized aluminium end plate of the reservoir. The reservoir was constructed of 2.54 cm thick transparent lucite plate in order to allow for flow visualization.

Shown in Figure (III-1) is the device for holding the capillary tubes in place at the end of the reservoir. This holding device was capable of withstanding maximum pressure of approximately 4.0×10^6 dynes/cm² in the reservoir.

III.1-2 Capillary Tubes

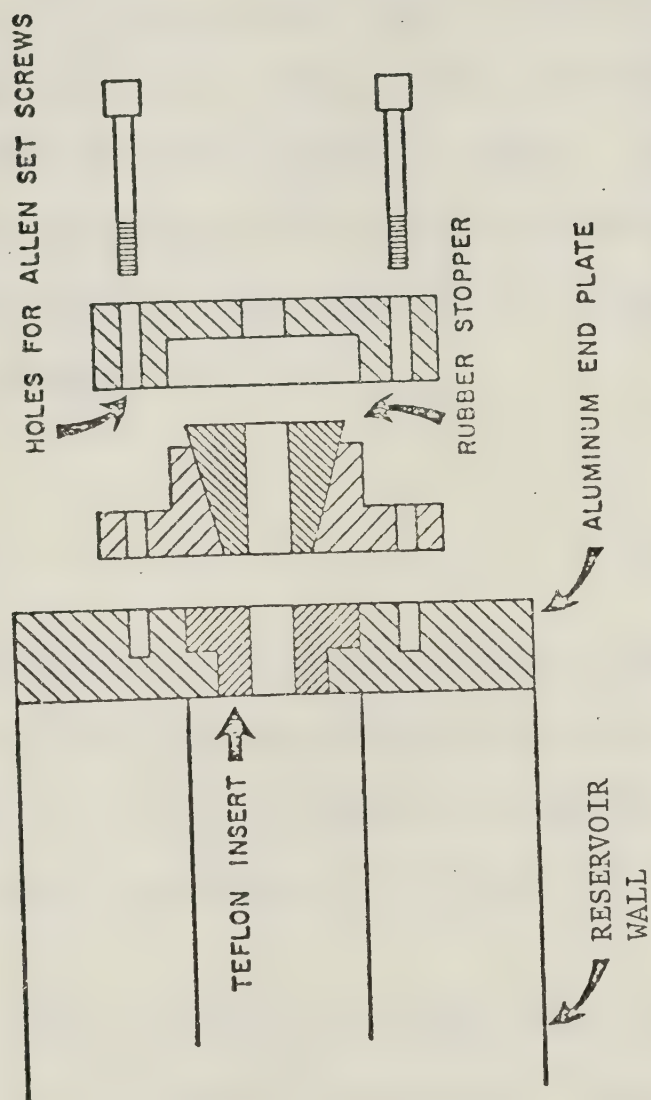
Two glass capillary tubes with I.D. of 0.20, and 0.30 cm \pm 0.00076 cm were used in this study. The capillary tubes were manufactured by Fischer-Porter. The length to diameter ratios (L/D) for the two capillary tubes were 54.96 and 55.04 for I.D. of 0.20, and 0.30 cm respectively.

III.1-3 Flow System

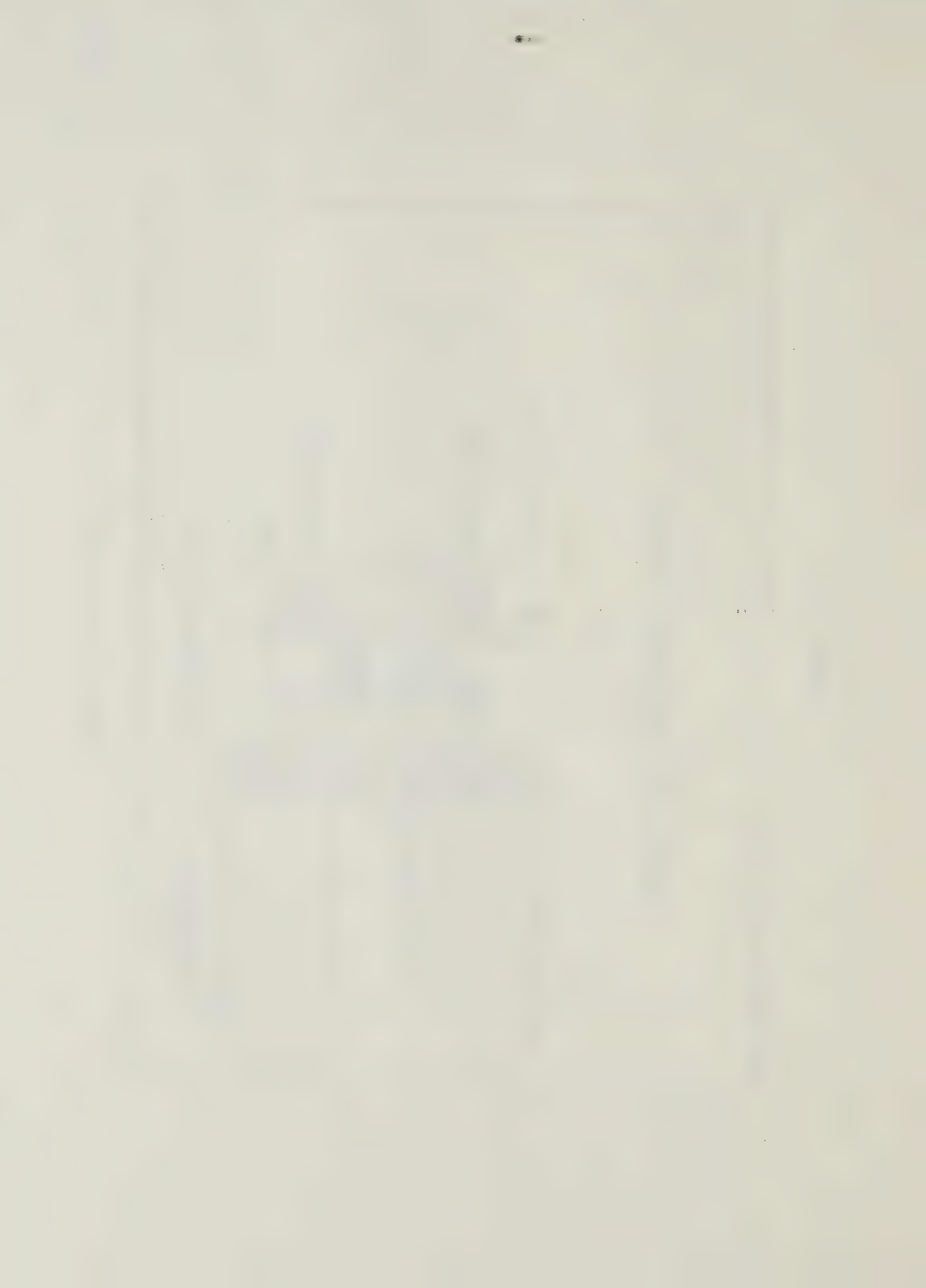
An Instron (Model TT-BM) and a stainless steel hydraulic cylinder of approximately 15.60 cm I.D. were used to provide a constant flow rate of the polymer solution. The calibration for the Instron,

FIGURE III-1

CAPILLARY HOLDING DEVICE



(Figure from Catania)



given in Appendix A, revealed that the flow rates calculated from knowledge of the Instron speed and the volumetrically measured flow rates were within 0.5% of each other.

When the piston was in its lowest position (the cylinder was nearly empty), there was still a clearance or space between the piston and the bottom of the cylinder. Before the cylinder was filled with polymer solution, a vacuum pump was used to eliminate air which would be trapped just below the piston. The air and any residual polymer solution in the space was drawn out by a vacuum pump into a flask. The polymer solution was then sucked into the cylinder by moving the piston upward. When the piston was in its highest position (the cylinder was full of polymer solution), it would stop automatically. This procedure was repeated each time for refilling the cylinder.

III.2 Experimental Fluid

III.2-1 Experimental Fluid

The experimental fluid was a 0.2% aqueous solution of Separan AP-30. Separan AP-30 is a partially hydrolyzed polyacrylamide with molecular weight between 2 and 3×10^6 and was supplied by the Dow Chemical Company. The rheological properties of the polymer solution are given in Appendix B.

A small amount of sodium bicarbonate was added to the polymer solution in order to protect it from bacterial degradation. Also, the polymer solution was used only once to ensure that the properties did not change from run to run owing to mechanical degradation.

III.2-2 Tracer Particles

Aluminium metal dust, manufactured by J.T. Baker Chemical Co., Lot number 2347, was used as tracer. Approximately 1 c.c. of these irregularly shaped particles were added to 300 lb. (136 Kg.) of the polymer solution. To prevent the particles from adhering to each other, they were dispersed with a glass rod in a small quantity of water (approximately 1 c.c.) before mixing with the polymer solution.

III.3 Photographic Techniques

III.3-1 Optical System

The main features of the optical system which consisted of a light source, a converging lens, a rotating chopping disc, a reservoir, and a photographic assembly are shown in Figure (III-2).

a. Light Source

The light source used in this study was a CHRISTIE xenon arc-lamp which operated from a three phase CHRISTIE silicon rectifier unit with a maximum output of 3300 watts D.C. at 100 amps. The set of converging mirrors in the lamphouse (Model BSF 50) were adjusted to direct the light beam with its maximum brightness and light uniformity through a narrow slit located on the wall of the reservoir. The procedures of adjusting those mirrors are shown in "Introductions for XENOLITE BSF Series Xenon Lamphouse". An adjustable horizontal slit placed immediately in front of the lamphouse lens, resulted in a light beam which was less in thickness than the slits on the chopping disc but wider than the approximately 0.41 mm wide slit on the wall of the reservoir.

FIGURE III-2

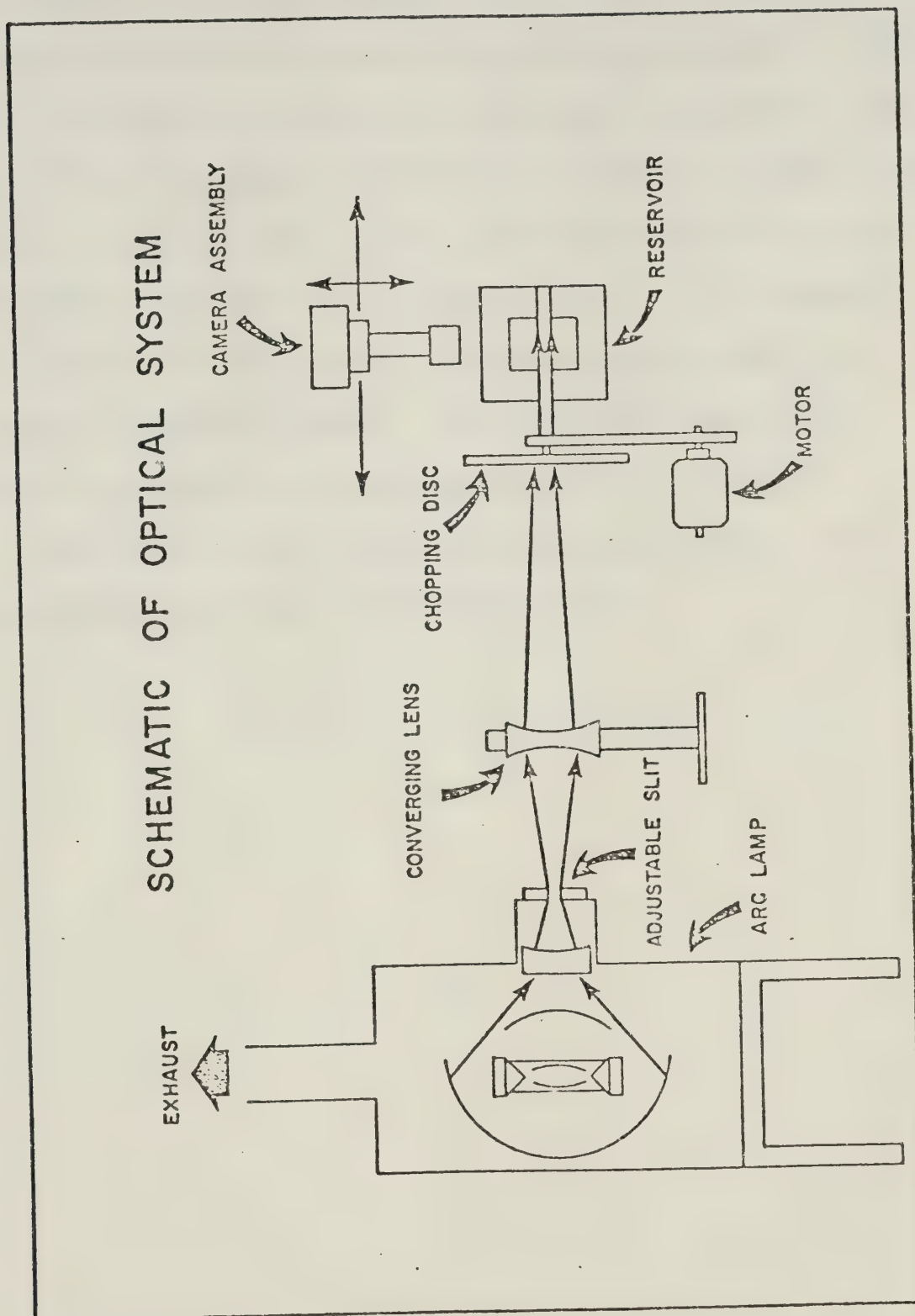


(Figure from Catania)

b. Chopping Disc

A paper disc, with 20 equal radial slits and spokes was clamped between two transparent lucite discs of 44.6 cm diameter. This chopping disc was located perpendicular to the light beam with its center in the plane of the light beam. The disc was driven by a variable speed drive in order to allow the time interval (the time for the slit to cut the beam of light) to be adjusted to a desired value. It is evident that higher flow rates required higher rotational speed in order to obtain reasonable lengths of streaks. The rotational speed of the chopping disc was measured by a stroboscope Type 1531-A STROBOTAC.

Table (III-1) lists the R.P.M. of the chopping disc used according to different capillary tubes and flow rates.

TABLE III-1

TIME INTERVALS FOR STREAK ANALYSIS

Diameter (cm)	Flow Rate (cm ³ /sec)	Speed of Chopping Disc R.P.M.	Time Interval x10 ³ (sec)	Extension Tube
0.20	0.1598	95.5	31.4	A
		109	27.5	A
		300.5	9.98	C
		304	9.87	C
0.3196	0.3196	68	44.12	A
		242	12.40	A
		265	11.32	A
		322.5	9.30	C
		344	8.72	C
0.6392	0.6392	364	8.24	C
		94	31.91	A
		344	8.72	A
		381	7.87	A

Continued.....

TABLE III-1 (continued)

Diameter (cm)	Flow Rate (cm ³ /sec)	Speed of Chopping Disc R.P.M.	Time Interval x10 ³ (sec)	Extension Tube
0.30	0.1598	69	43.50	B
		69.5	43.20	B
		70	42.90	B
0.30	0.3196	146	20.55	A
		221	13.57	B
		242	12.40	B
		265	11.32	B
	0.6392	196	15.31	A
		324	9.26	B
		344	8.72	B

c. Photographic Assembly

A Miranda 35 mm camera, located perpendicular to the light beam, was secured to Setco Building Blocks. This allowed the camera to be moved in planes parallel and perpendicular to the light beam. Three extension tubes, A. B. C. were used with a 1:2.8/105 mm lens and the resulting real magnifications on the film were approximately 0.73, 2.18, 2.73 respectively. Tri-X film with ASA speed of 400 was used. Approximate exposure times and apertures which were used in this study for each different extension tube are listed in Table (III-2).

TABLE (III-2)
EXPOSURE TIMES AND APERTURES

Extension Tube used	Exposure Time (sec)	Aperture
A	8	f:4
B	25	f:2.8
C	30	f:2.8

The exposure times listed in Table (III-2) were approximately the maximum exposure times before background light would cause loss of contrast or overexposure of the film. Therefore, actual exposure times were sometimes shorter than the values listed in Table (III-2), and were dependent on how much time was necessary until a few bright particles passed through the field of view.

d. Reservoir

To minimize reflections and aid in providing as much contrast as possible for photographing the streaks, the reservoir was painted black inside except for the light slits on the side and the top camera viewing area. Also, the portion of the capillary tube outside the reservoir was covered by putting a sheet of black paper in front of it. During an experimental run the room was in total darkness.

The upstream end of the capillary tube was made to project slightly into the upstream reservoir, so that the detailed velocity field could be studied photographically very near the capillary tube entry without the walls of the reservoir obscuring the view. The length of the capillary tubes protruding into the reservoir from the end plate were approximately 0.10 and 0.20 cm for tube I.D. of 0.20 and 0.30 cm respectively.

III.3-2 Streak Photographs

Over 1,000 photographs were taken for three different flow rates with each capillary tube. Typical streak photographs are shown in Figures (III-3), (III-4) and (III-5).

The flow field shown in Figure (III-3), was obtained with the 0.20 cm I.D. capillary tube at the largest flow rate of $0.6392 \text{ cm}^3/\text{sec}$ (flow moving from bottom to top) for which the velocity profiles were measured. The film exposure time was 8 sec. and the extension tube A was used. The time interval for a streak was 0.00787 sec. This figure shows the typical wine glass shaped core surrounded by large eddies.

The flow field shown in Figure (III-4), was obtained with the 0.20 cm I.D. capillary tube at a lowest flow rate of $0.1598 \text{ cm}^3/\text{sec}$

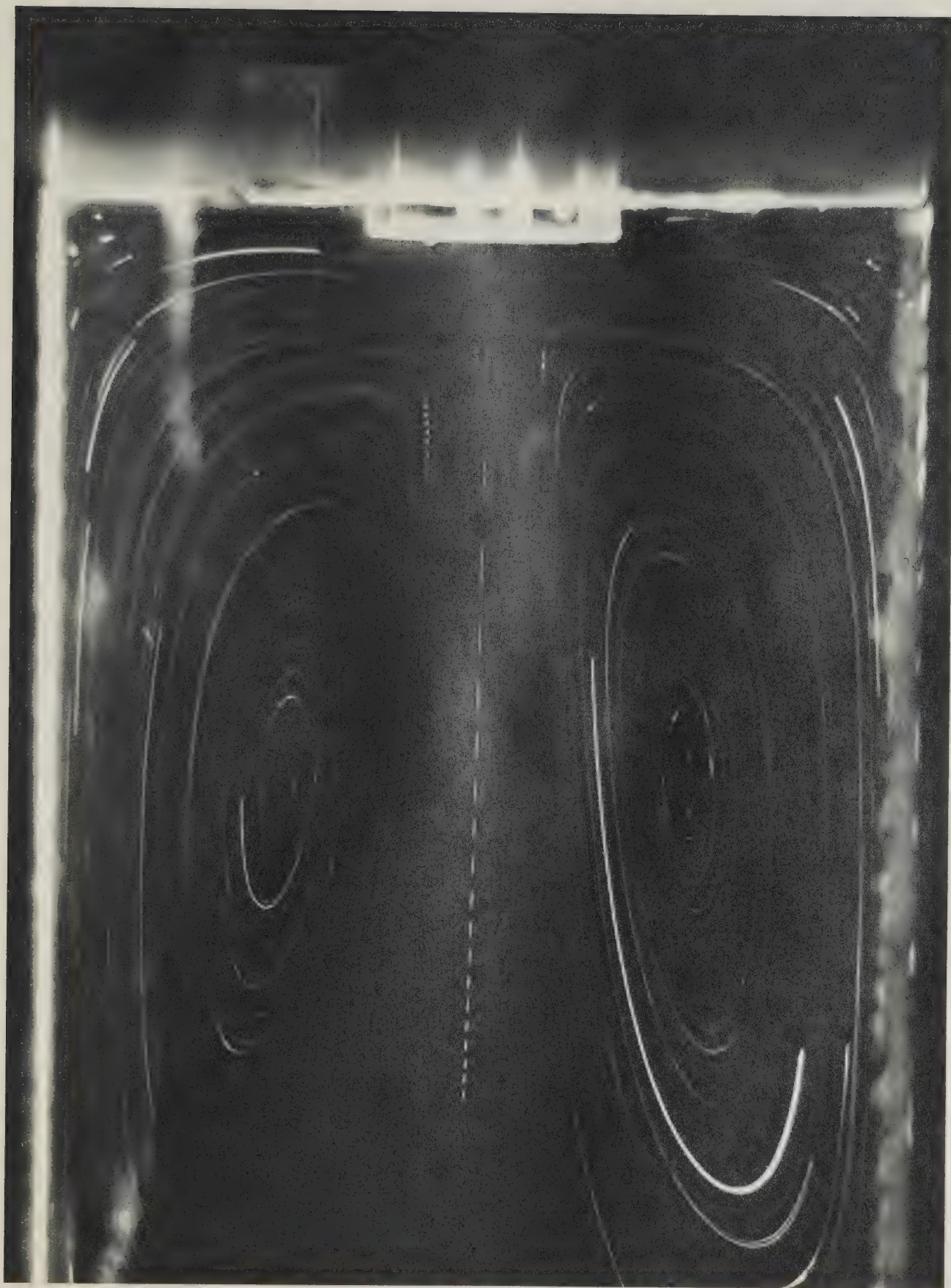


FIGURE III-3

Streak Photograph, 0.20 cm I.D.

$Q = 0.6392 \text{ cm}^3/\text{sec}$, Extension Tube A

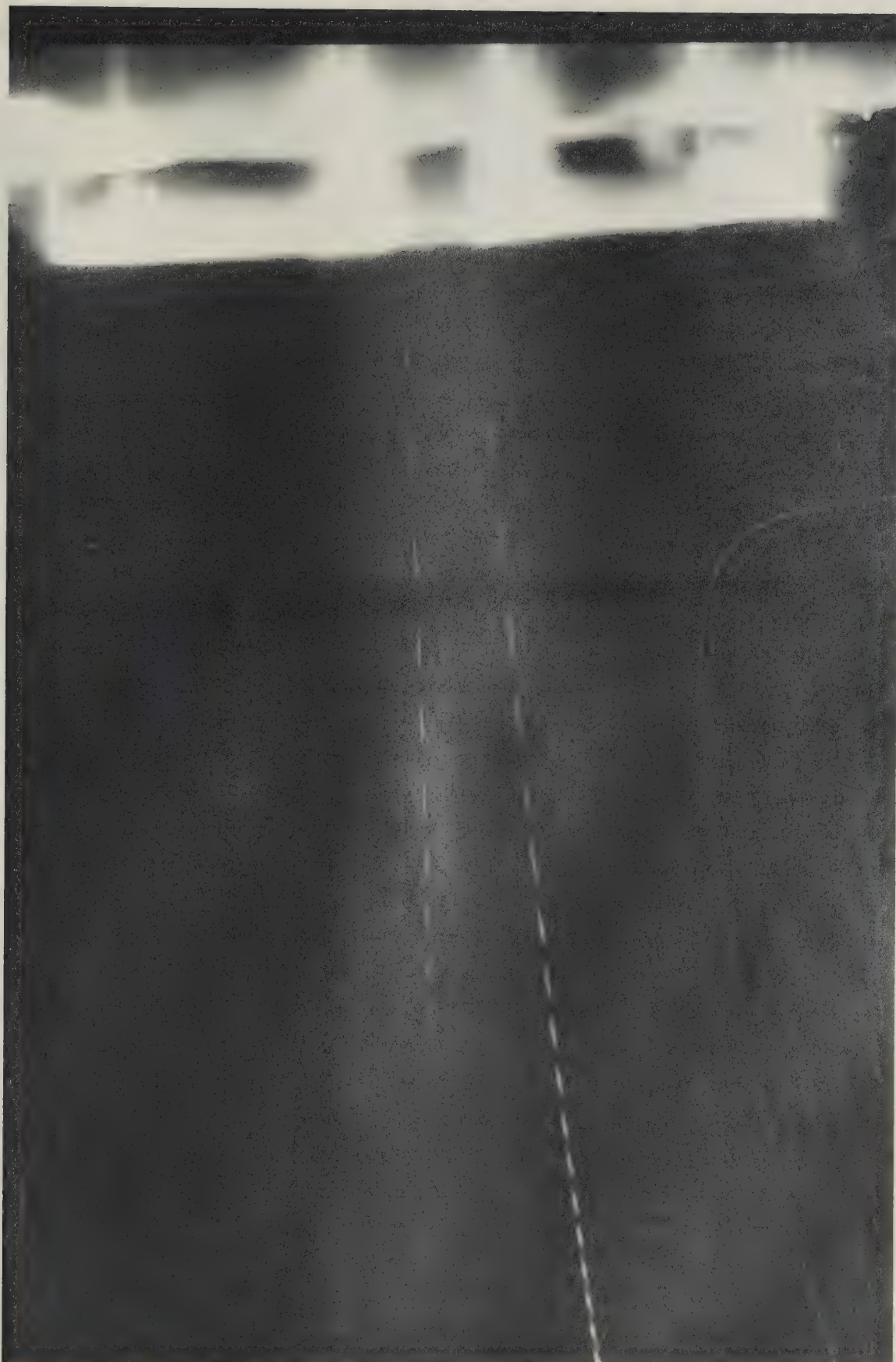


FIGURE III-4 Streak Photograph, 0.20 cm I.D.
 $Q = 0.1598 \text{ cm}^3/\text{sec}$, Extension Tube C

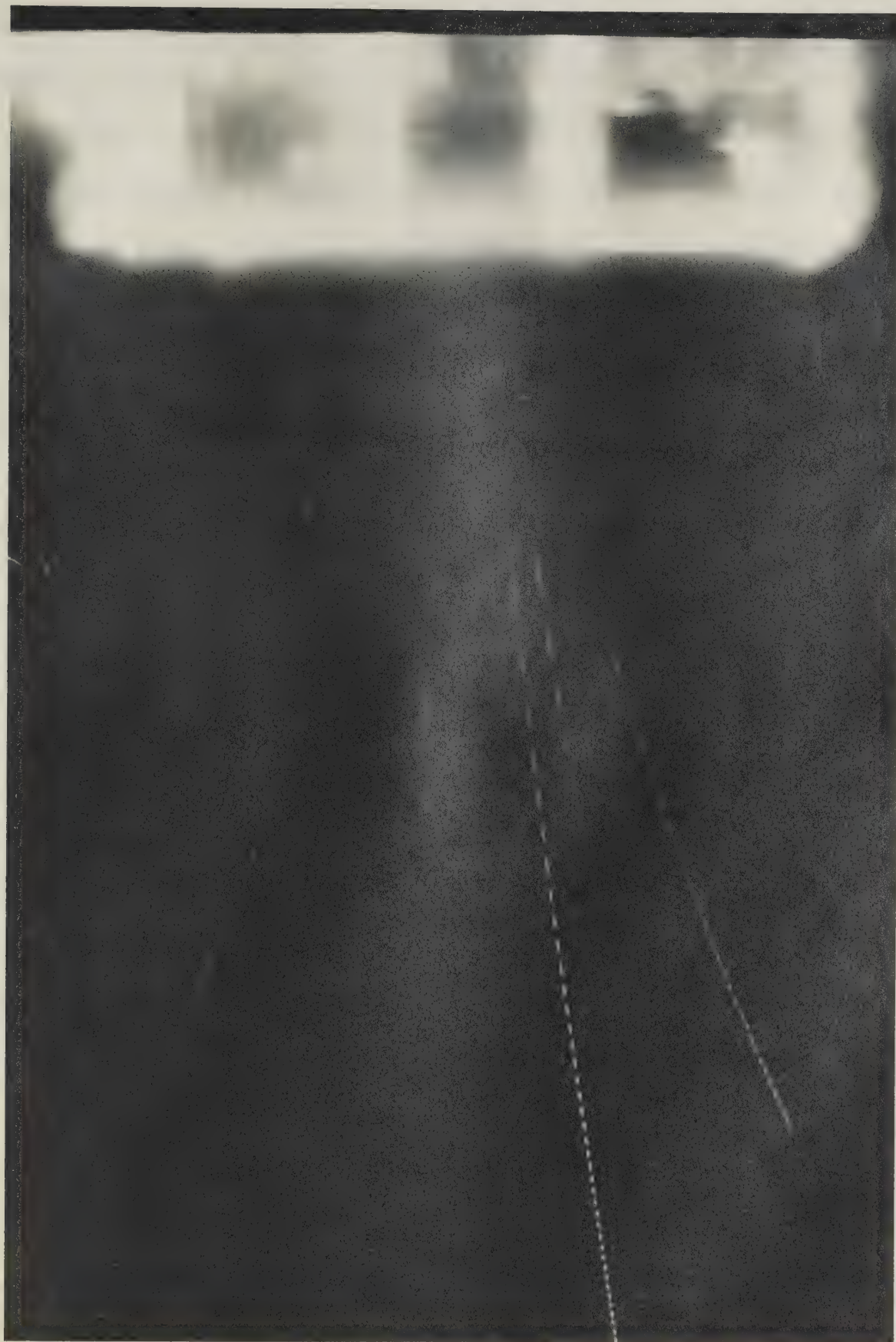


FIGURE III-5

Streak Photograph, 0.30 cm I.D.

$Q = 0.1598 \text{ cm}^3/\text{sec}$, Extension Tube B

(flow moving from bottom to top). The film exposure time was 30 sec and the extension tube C was used. The time interval for a streak was 0.00987 sec. The flow field shown in Figure (III-5) was obtained with the 0.30 cm I.D. capillary tube at a lowest flow rate of $0.1598 \text{ cm}^3/\text{sec}$ (flow moving from bottom to top). The film exposure time was 25 sec and the extension tube B was used. The time interval for a streak was 0.0429 sec. Those two figures show a better view of the velocity field very near to the tube entry than Figure (III-3).

Using several photographs similar to those illustrated by the figures, the streamlines and the axial velocity distributions were determined for several flow rates.

III.3-3 Analysis of Streak Photographs

a. Local Axial Velocity Measurements

A Bell & Howell projector (Model 745C) was used to project the photograph negatives on graph paper which was graduated in 0.10 inch divisions. The streaks were traced directly onto the graph paper. For example, consider the data obtained for the 0.30 cm I.D. capillary tube and for a flow rate of $0.3196 \text{ cm}^3/\text{sec}$. Figure (III-6) illustrates how streaks would look as traced onto the graph paper. Figure (III-6) is in scale with respect to the tube diameter except the streaks of streamline number 11, which has been included to illustrate a streak close to the outermost streamline. In this example, the actual magnification used on the graph paper was 49.8. Knowing the magnification and the time interval, these streak lengths were converted into velocities along the streamlines. Although not precisely the axial or "z" velocity the small cone angles resulted in only small difference between axial and measured velocity. Therefore, these measured velocities can

be reasonably assumed as the axial velocities all through this study.

Then,

$$V_z = \frac{\Delta L}{M\bar{t}} \quad (\text{III-1})$$

where ΔL = length of streak, cm

V_z = axial velocity, cm/sec

M = magnification of the streaks on the graph paper

\bar{t} = $(60/N\omega)$, sec

N = number of slits and spokes on the chopping disc

ω = number of revolutions per minute, R.P.M.

A sample calculation will be shown in Appendix F.

To minimize the error due to the half-shadow at the beginning and the end of every light period, and also the error due to finite particle size, nearly all the streak lengths were measured from leading edge to leading edge of the particles. Near the entry and close to the centerline of the capillary tube where the streaks were the longest, this was not always possible.

The resulting velocities as a function of distance from the entrance are plotted in Figure (III-7) for the streamlines corresponding to those in Figure (III-6). The solid lines in Figure (III-7) are the eye-fit lines to the data and which have been extrapolated to estimate velocity right at the contraction.

FIGURE III-6

STREAK LENGTH ALONG SEVERAL STREAMLINES

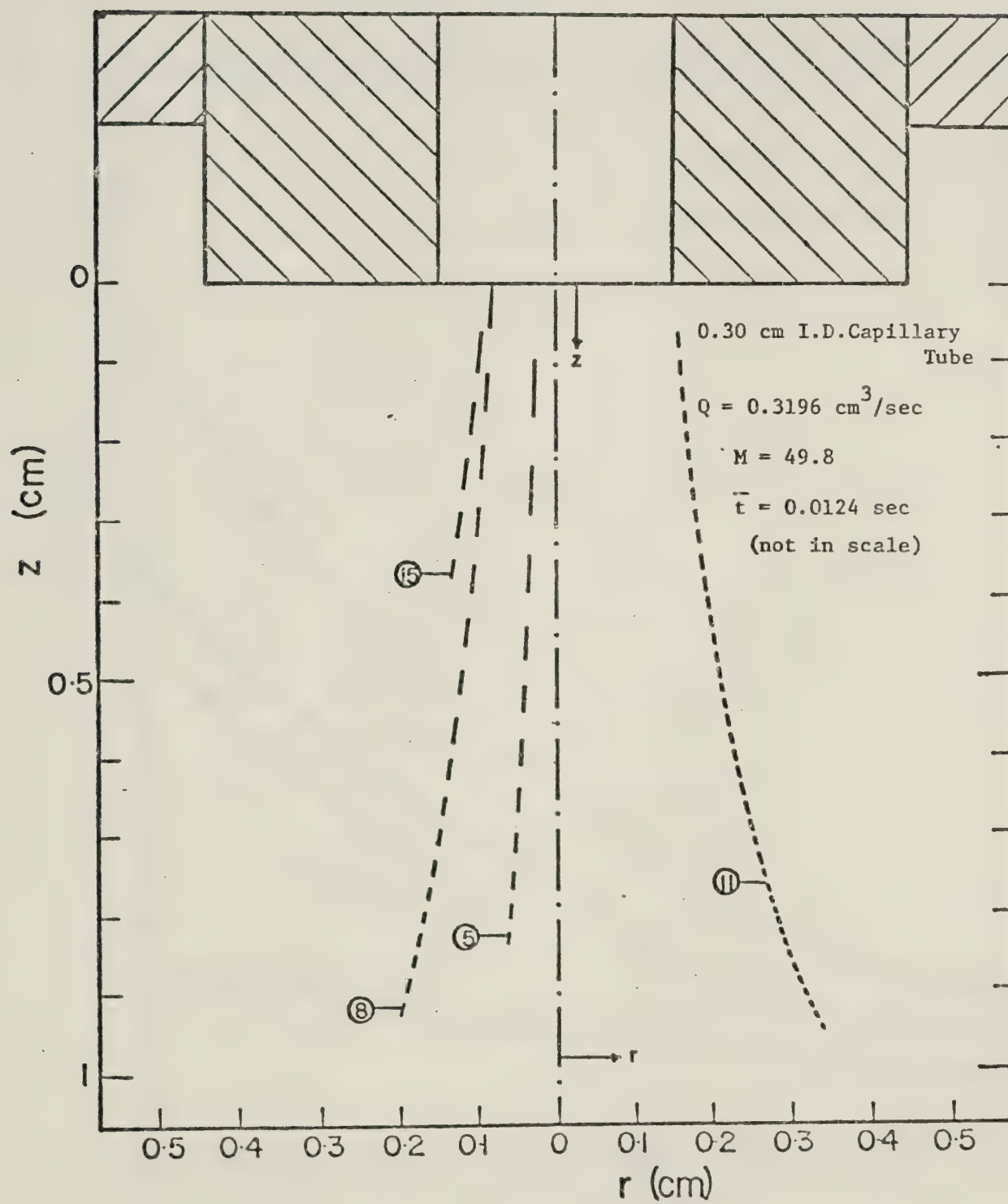
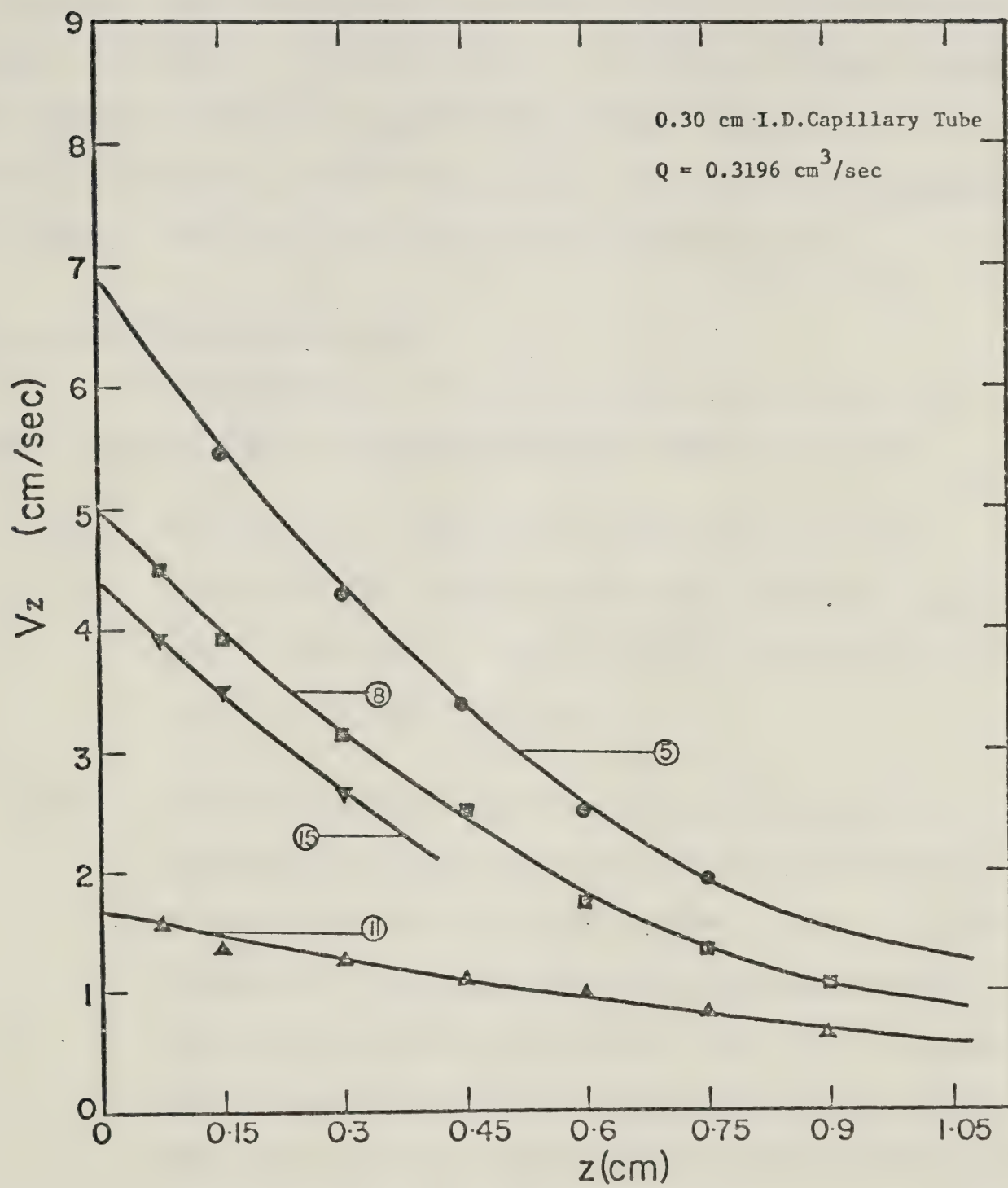


FIGURE III-7

TYPICAL AXIAL VELOCITY - POSITION DATA



b. Cone Angle Measurements

The cone angles at the contraction and upstream of the contraction, are defined as the angle formed by the line tangent to the outermost streamline that enters into the capillary tube. This streamline however, was not precisely determinable for all of the experimental runs. For example, in Figure (III-6), it is difficult to tell whether the streamline number 11 is exactly the outermost streamline of the flow that enter into the capillary tube or not. By using streamline number 11, however, the initial cone angle was estimated to be 6.2° .

c. Discussion of Error

In determination of the velocity distribution there were several sources of error associated with the projection technique.

- (i) At speeds of the chopping disc below 110 R.P.M., the speeds could only be measured by means of multiple images using a stroboscope. Repeat readings gave deviations as large as $\pm 2\%$ from the average.
- (ii) Using the projection technique it is important to know how accurately the streaks could be located with respect to the centerline of the capillary tube. This is because for each velocity profile, the data points were measured from several separate photographs. There were two methods used to locate the centerline of the capillary tube on the graph paper depending on which extension tube was being used. For photographs taken by extension tubes B and C where the walls of the reservoir could not be seen, the centerline of

the capillary tube was determined by measuring half way between the two visible outside walls of the capillary tube. By knowing the outside diameter of the capillary tube, the magnification of the photograph project onto the graph paper could also be found. For photographs taken by extension tube A, where the walls of the reservoir could be seen, the centerline of the capillary tube was determined by finding the center between the two reservoir walls. The magnification in this case could also be found by knowing the outside diameter of the capillary tube or, alternatively, from the known inside width of the reservoir.

Although the capillary tube was located following the procedure of centering of capillary tube which will be discussed in Section III.4-2, perfect symmetry was not always achieved in the velocity profiles because of non-uniformity in the wall thickness of the tubes. This would also cause an error in estimation of magnification. For example, consider data for the 0.30 cm I.D. capillary tube at the highest flow rate $0.6392 \text{ cm}^3/\text{sec}$ for which the photographs were taken by extension tubes A and B. The axial velocity profiles are shown in Figure (IV-2), and it can be seen that the local velocities on the right of the center are somewhat higher than those on the left. Also the experimental flow rates which were calculated from the areas under the curves of plot V_z versus r^2 at different axial positions, were always less than the calibrated flow rate by about 6%.

- (iii) Due to hazy beginning and end of the streaks, there is an error in measurement of the length of the streaks. This is more significant for short streaks than the long streaks. The rotational speed of the chopping disc was chosen to have most accuracy for streaks near the entry of the capillary tube. Therefore, streaks at locations further upstream were sometimes too short to measure with high accuracy. A good example for this case is for the 0.20 cm I.D. capillary tube at a flow rate of $0.6392 \text{ cm}^3/\text{sec}$ and at an axial location equal to three tube diameters ($z/D = 3$) which was the furthest upstream velocity profile measured. Here an error of 12% between the experimental flow rate and the calibrated flow rate was found.
- (iv) Since the depth of field of the camera was always greater than the depth of the beam of light, it was not possible to distinguish whether the aluminium dust particles were at the top of the beam of light (nearest to the camera), or at the bottom of the beam of light or at any intermediate plane lying within these limits. Thus, the streamlines on the photographs were not necessarily in the plane of the centerline of the capillary tube. The larger the velocity gradient the larger the possible error. Assuming the aluminium dust particles are randomly distributed on the fluid, this would cause a random scatter in the data.

- (v) Since the measured length of streaks were not actually the distance travelled in the z-direction, the local velocities reported are not V_z but $(V_z^2 + V_r^2)^{1/2}$. This error becomes more significant when the angle between the streak and the centerline of the capillary tube becomes larger. Considering the worst case in this study, for the 0.30 cm I.D. capillary tube at lowest flow rate and at axial location equal to two diameters ($z/D = 2$), the derivation of $(V_z^2 + V_r^2)^{1/2}$ from V_z was less than 10%. While at higher flow rate and at axial location near the entry of the capillary tube, this derivation was always negligible. Therefore, no distinction is made between V_z and $(V_z^2 + V_r^2)^{1/2}$ in this study.

III.4 Procedure

III.4-1 Preparation of Polymer Solution

To prepare the 0.2% (by weight) Separan AP-30 Solution, a stainless steel tank was filled with 300 lbs (136 Kg.) tap water and 272.1 gm. of solute. The salute was added slowly to the water so as to ensure that the powder was wetted without formation of large lumps and entrained bubbles. At the same time, a mixer agitated the solution very gently to avoid mechanical degradation and continued to do so for a period of approximately 10 hours after the final amount of solute was added to the solution. The solution was then left unsheared overnight. The specific gravity of the polymer solution determined for a fresh solution at 23°C, was 0.9984.

III.4-2 Centering of Capillary Tube

Since the wall thickness of each capillary tube was not uniform it was necessary to center each capillary tube so that the center of the capillary tube and the center of the light beam were on the same horizontal plane.

The empty reservoir was first adjusted so that it was in a horizontal plane. The capillary tube was then inserted into the holding device which was attached to the end plate of the reservoir. The light source was turned on and the room lights were turned off. The light beam was then clearly visible against the aluminium end wall of the reservoir and the side of the reservoir opposite the side where the adjustable slit was attached. By adjusting the level of the light source a plane passing through the center of the light beam was in line with a plane passing through an etched mark located on both sides of the reservoir. These etched marks represented a plane passing through the center of the hole in the aluminium end plate where the capillary tube was to be located. The capillary tube was rotated by hand until the center of the beam of light and the center of the capillary tube were judged by eye to be in the same plane.

III.4-3 Focusing on the Center of the Capillary Tube

To focus on the center of the capillary tube a wire sharpened to a point on the end and having a diameter approximately equal to the inside diameter of the capillary tube, was inserted into the tube until the end of it protruded into the reservoir. The light source was then turned on and the shadow of the wire was clearly visible against the side of the reservoir opposite the side where the adjustable

slit was attached. The wire was rotated slowly by hand until the shadow of the tip of the wire on the side of the reservoir was judged by eye to be in the center plane of the light beam, in other words, in the center plane of the capillary tube. The camera was then focused onto the illuminated tip of the wire.

Since the depth of field of the camera was greater than the thickness of the light beam, all aluminium particles within the beam's thickness were illuminated and recorded on the film.

III.4-4 Data Collection of Velocity Profiles

Measurement of the velocity profiles for the 0.2% weight solution of Separan AP-30 was discussed in the previous sections of this chapter. The results are tabulated in Appendix C.

CHAPTER IV

RESULTS AND DISCUSSIONS

Since the unstable velocity field of the converging flow of viscoelastic fluid is nearly impossible to measure, only the velocity field for stable conditions is measured in this study. The highest flow rate chosen in this study so as to measure the velocity profiles within the central cord under stable conditions is $0.6392 \text{ cm}^3/\text{sec}$ for both capillary tubes. Although the critical flow rates for the breakdown of the entrance velocity fields for different capillary tubes estimated by Catania (10) was approximately $0.318 \text{ cm}^3/\text{sec}$ for a 0.2 cm capillary tube, the velocity field at $0.6392 \text{ cm}^3/\text{sec}$ for 0.2 cm I.D. capillary tube is observed to be stable in this study. In this study, the axial velocity profiles at different locations upstream of the contraction were measured for three different flow rates of 0.6392, 0.3196, $0.1598 \text{ cm}^3/\text{sec}$ for both capillary tubes. In addition, the initial cone semi-angles and the upstream cone semi-angles were measured so as to present a complete description of the flow field within the central cord of the converging flow.

IV.1 Axial Velocity Profiles

Table (IV-1) shows the flow rates and the dimensionless locations upstream of the contraction where velocity profiles were measured. As indicated by the table the velocity profiles were measured in the region very close to the contraction. This region is of particular interest because it has been realized that the distortion of emerging extrudates may be closely related to the flow in this region.

TABLE IV-1

Flow Rates and Axial Locations for Velocity Profiles Measured

I.D. (cm)	Flow Rate (cm ³ /sec)	Axial Location (z/D) (No. of Diameter)
0.20	0.1598	0.0*
		1.0
		2.0
	0.3196	0.0*
		1.0
		2.0
		3.0
	0.6392	0.0*
		1.0
		2.0
		3.0
		3.0
0.30	0.1598	0.0*
		1.0
		2.0
		3.0
	0.3196	0.0*
		1.0
		2.0
		3.0
		3.0
		3.0

TABLE IV-1 (continued)

I.D. (cm)	Flow Rate (cm ³ /sec)	Axial Location (z/D) (No. of Dia.)
0.30	0.6392	0.0*
		1.0
		2.0
		3.0

* From eye fit extrapolated data

Raw velocity data are tabulated in Appendix C. From these data, typical velocity profiles are given in Figures (IV-1) and (IV-2) at several upstream axial locations for two different capillary tubes. The accuracy of these data may be judged in the following way. The local velocities can be integrated over the cross section of the converging flow that enters the tube and the result compared with the known volumetric flow rate. This comparison is of interest as it can be made in the upstream field for different locations. The mean deviation of these integrated flow rates from calibrated flow rates was approximately equal to 5%.

Figure (IV-1) shows the velocity profiles which were obtained with the 0.20 cm I.D. capillary tube at the smallest flow rate 0.1598 cm³/sec. Figure (IV-2) shows the velocity profiles which were obtained with the 0.30 cm I.D. capillary tube at the highest flow rate 0.6392 cm³/sec. The axial velocity profiles at the contraction, $z/D = 0.0$, were impossible to measure directly in this study but were obtained with

FIGURE IV-1

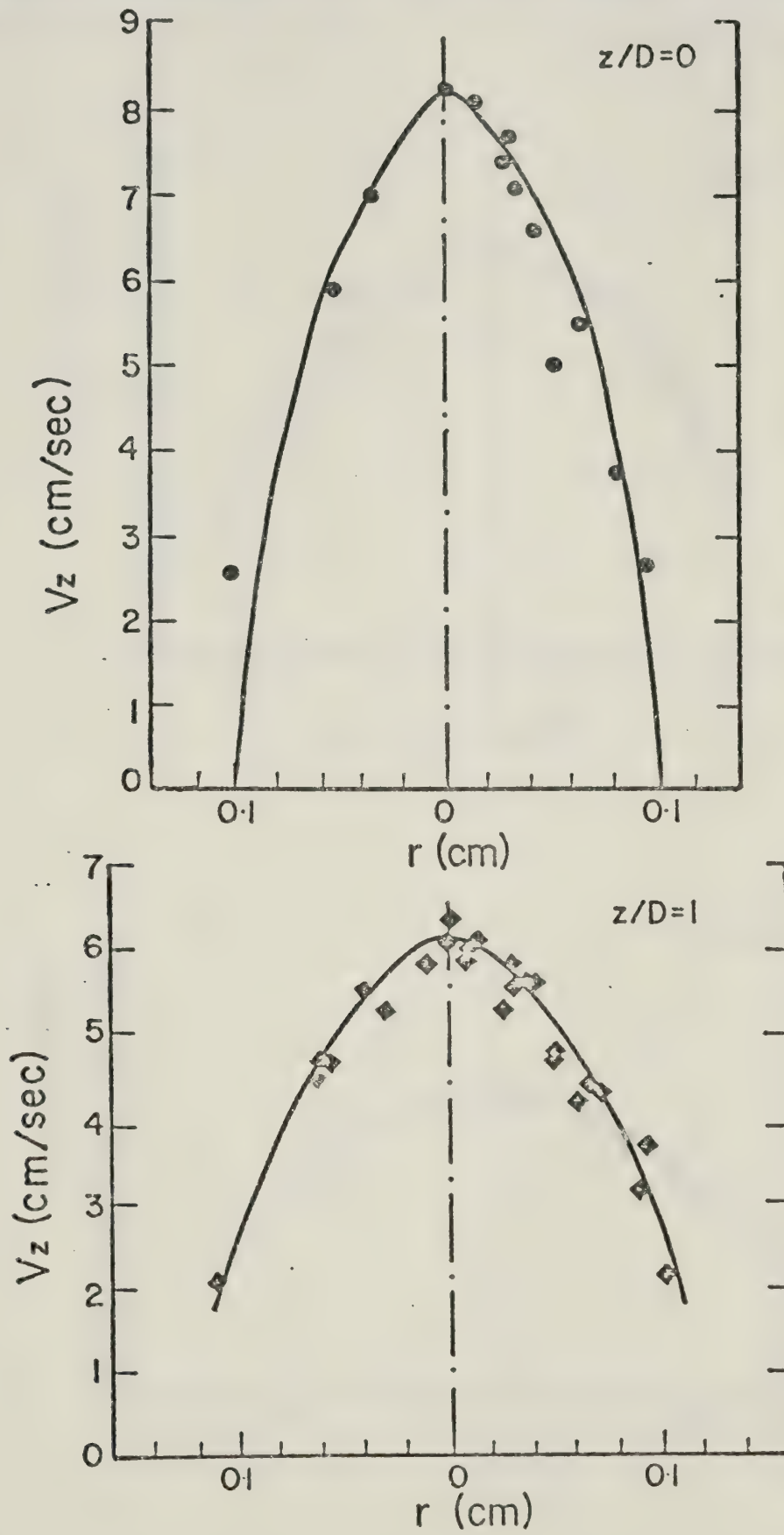
AXIAL VELOCITY PROFILES, 0.20 cm I.D. CAPILLARY TUBE, $Q = 0.1598 \text{ cm}^3/\text{SEC}$ 

FIGURE IV-1 (CONTINUED)

0.20 cm I.D. CAPILLARY TUBE

$$Q = 0.1598 \text{ cm}^3/\text{SEC}$$

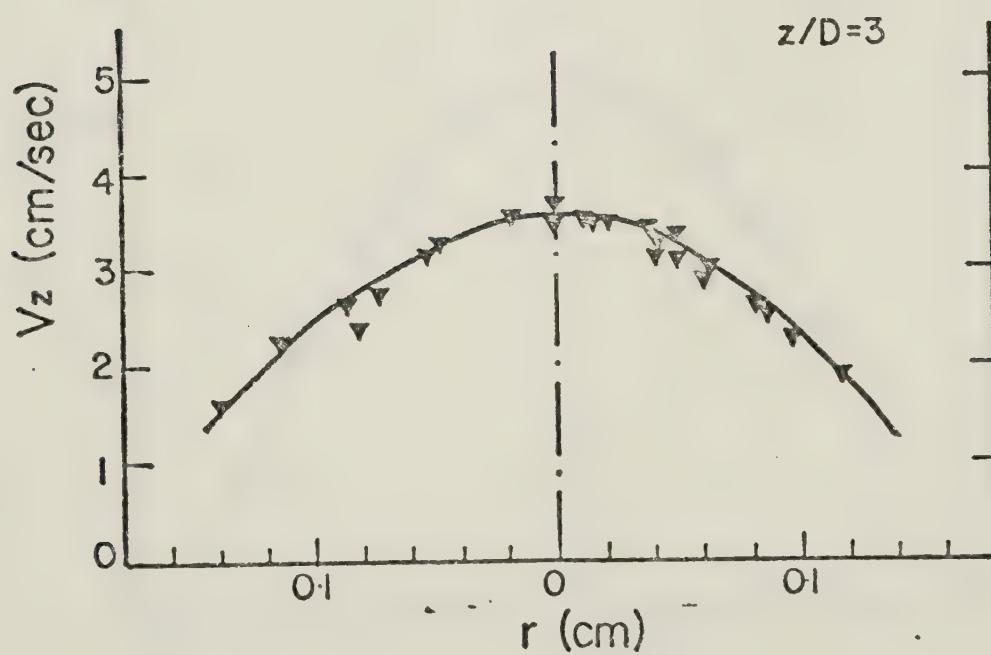
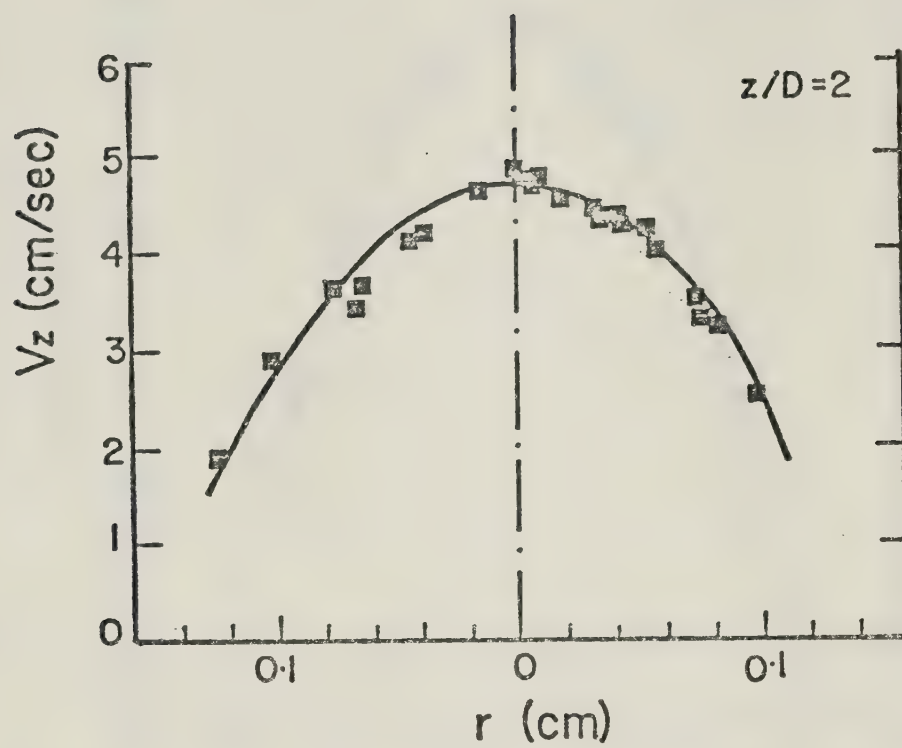


FIGURE IV-2

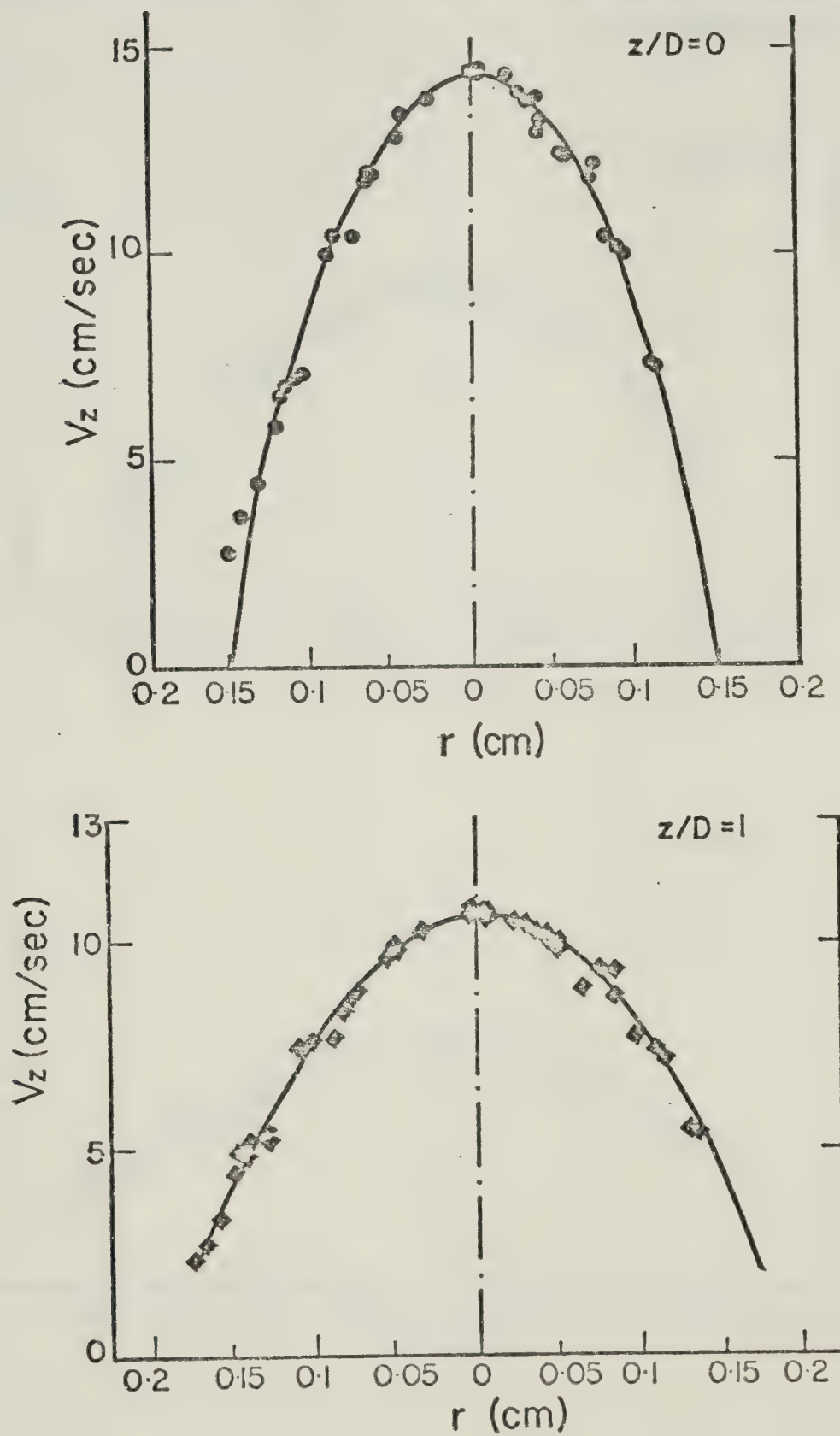
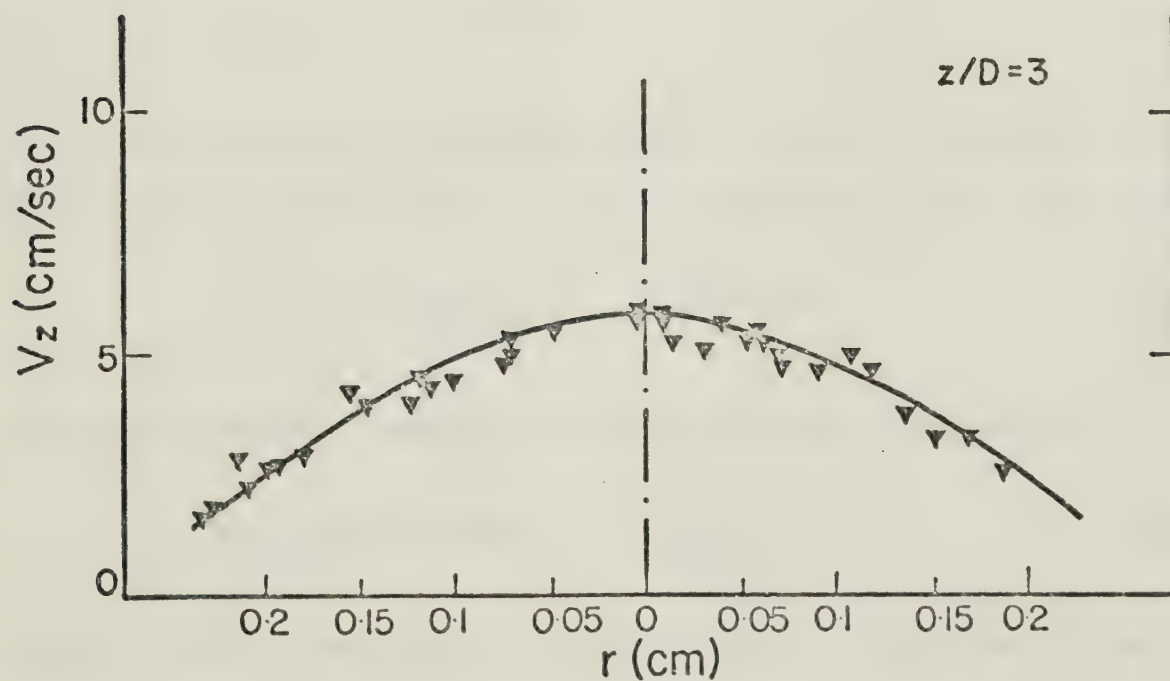
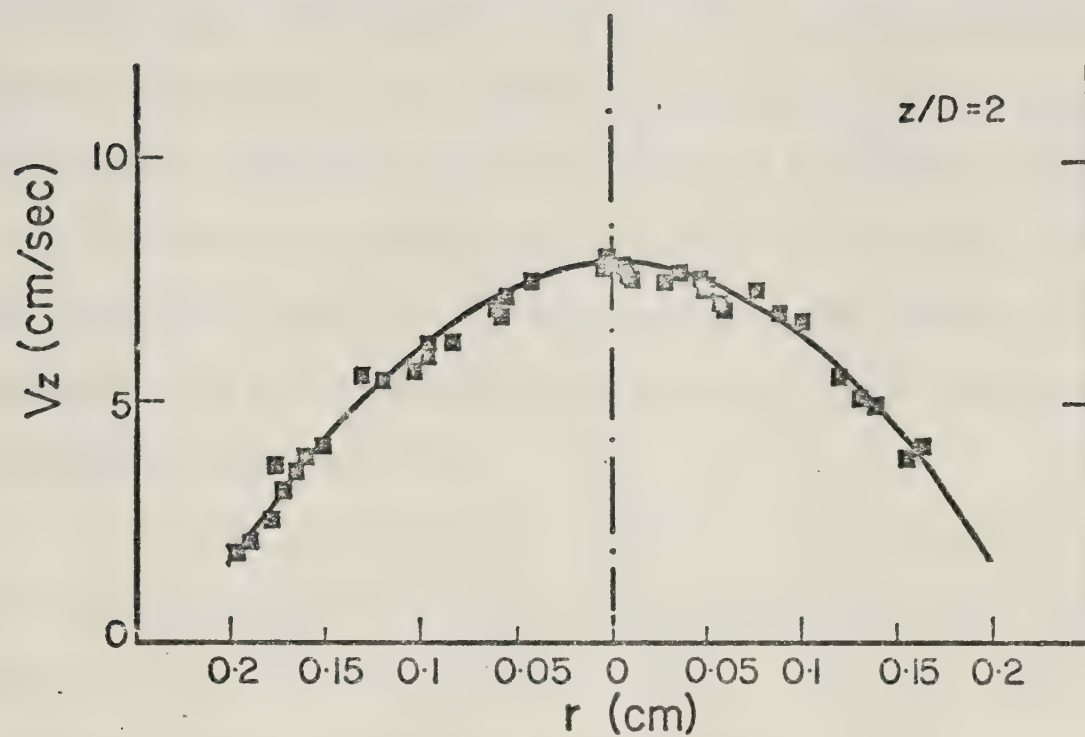
AXIAL VELOCITY PROFILES, 0.30 CM I.D. CAPILLARY TUBE, $Q = 0.6392 \text{ cm}^3/\text{SEC}$ 

FIGURE IV-2 (CONTINUED)

0.30 cm I.D. CAPILLARY TUBE

$$Q = 0.6392 \text{ cm}^3/\text{SEC}$$



the extrapolated data points. This extrapolation procedure will be discussed in Appendix C.

All of the data as illustrated in Figures (IV-1) and (IV-2) show that the velocity profiles within the central core are not flat as assumed by many investigators (26, 27, 32). In Figure (IV-2), for example, at $z/D = 1.0$, the velocity at the centerline and the velocity at outermost streamline were 10.9 cm/sec and 2.30 cm/sec respectively. Also, for the entire range of the flow rates in this study, the ratio of the centerline velocity at the contraction to the centerline velocity for developed flow of a power-law fluid in the capillary tube, was approximately constant and equal to 0.946.

A plot of centerline velocities at the contraction ($V_{z,\zeta,0}$) which are tabulated in Appendix C versus the average velocity at the contraction (V) is shown in Figure (IV-3). The solid line with slope equal to 1.0 can be written as Equation (IV-1);

$$V_{z,\zeta,0} = 1.617V \quad (IV-1)$$

With a power law fully developed velocity profile, the axial velocity of the fully developed profile in the capillary tube can be expressed as:

$$V_z = \left(\frac{3n+1}{n+1}\right) V \left[1 - \left(\frac{r}{R}\right)^{(n+1)/n}\right] \quad (IV-2)$$

Then the centerline velocity of the fully developed profile is,

$$V_{z,\zeta, \text{ fully devel. }} = \left(\frac{3n+1}{n+1}\right) V \quad (IV-3)$$

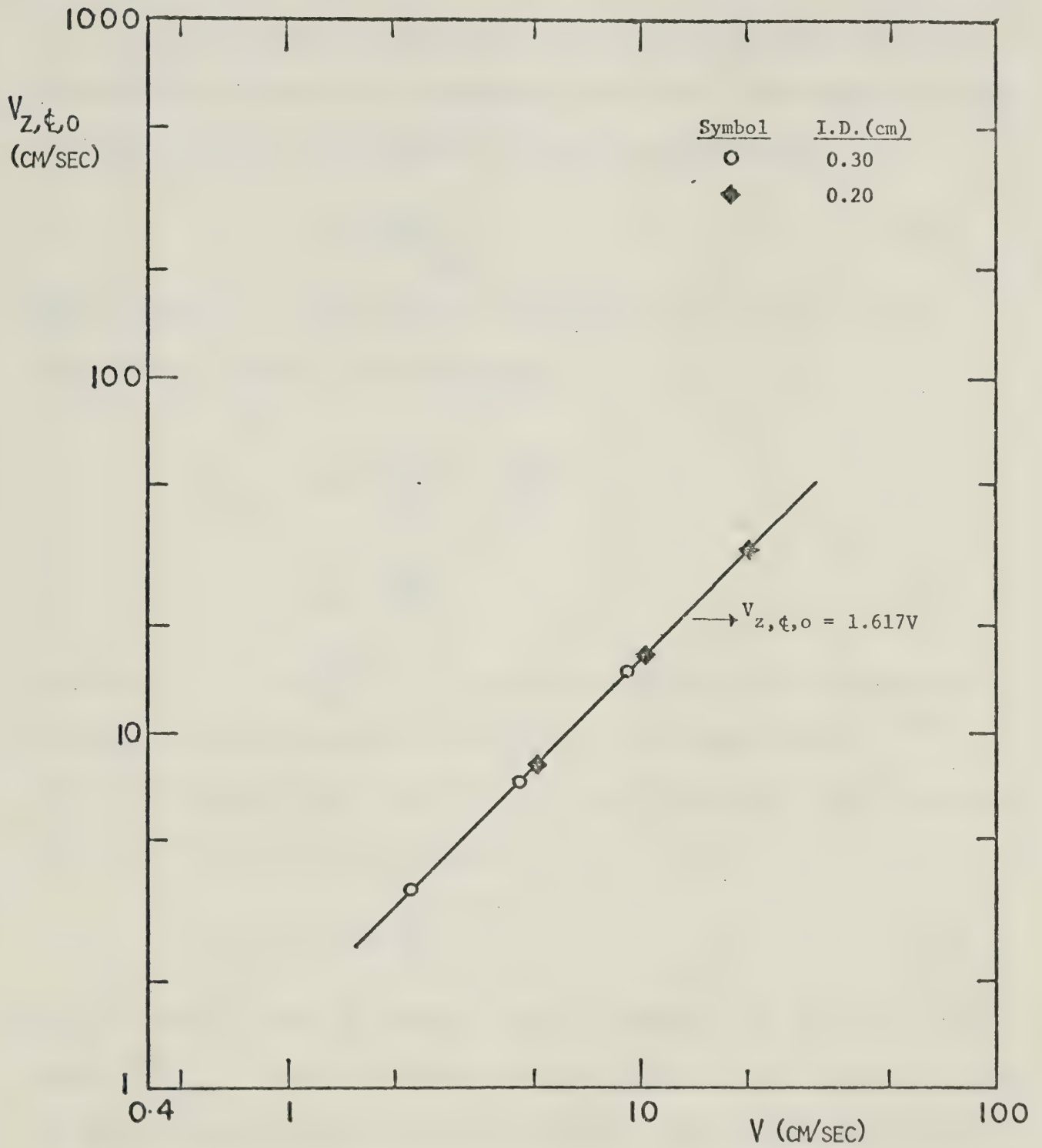
where n is the flow behavior index and equal to 0.55 from Appendix B.

Substituting Equation (IV-3) into Equation (IV-1):

$$V_{z,\zeta,0} = 0.946 V_{z,\zeta, \text{ fully devel. }} \quad (IV-4)$$

FIGURE IV-3

AXIAL CENTERLINE VELOCITY AT CONTRACTION VERSUS AVERAGE VELOCITY AT CONTRACTION



The ratio, $(V_{z,\phi,0}/V_{z,\phi,\text{fully devel.}})$ indicates the degree to which the velocity profile was developed at the contraction. Clearly the velocity profile is very nearly fully developed before the fluid enters the capillary tube.

It is also of interest to compare the wall shear stress at entrance with those of fully developed tube flow. Considering a power-law fluid, the wall shear stress (τ_w) can be expressed as,

$$\tau_w = K_o \left(\frac{dV_z}{dr} \right)_{r=R}^n \quad (\text{IV-5})$$

Differentiating Equation (IV-2) with respect to r and substituting into Equation (IV-5), and rearranging,

$$\begin{aligned} \tau_w &= K_o \left(\frac{3n+1}{4n} \right)^n \left(\frac{8V}{D} \right)^n \\ &= K_o' \left(\frac{8V}{D} \right)^n \end{aligned} \quad (\text{IV-6})$$

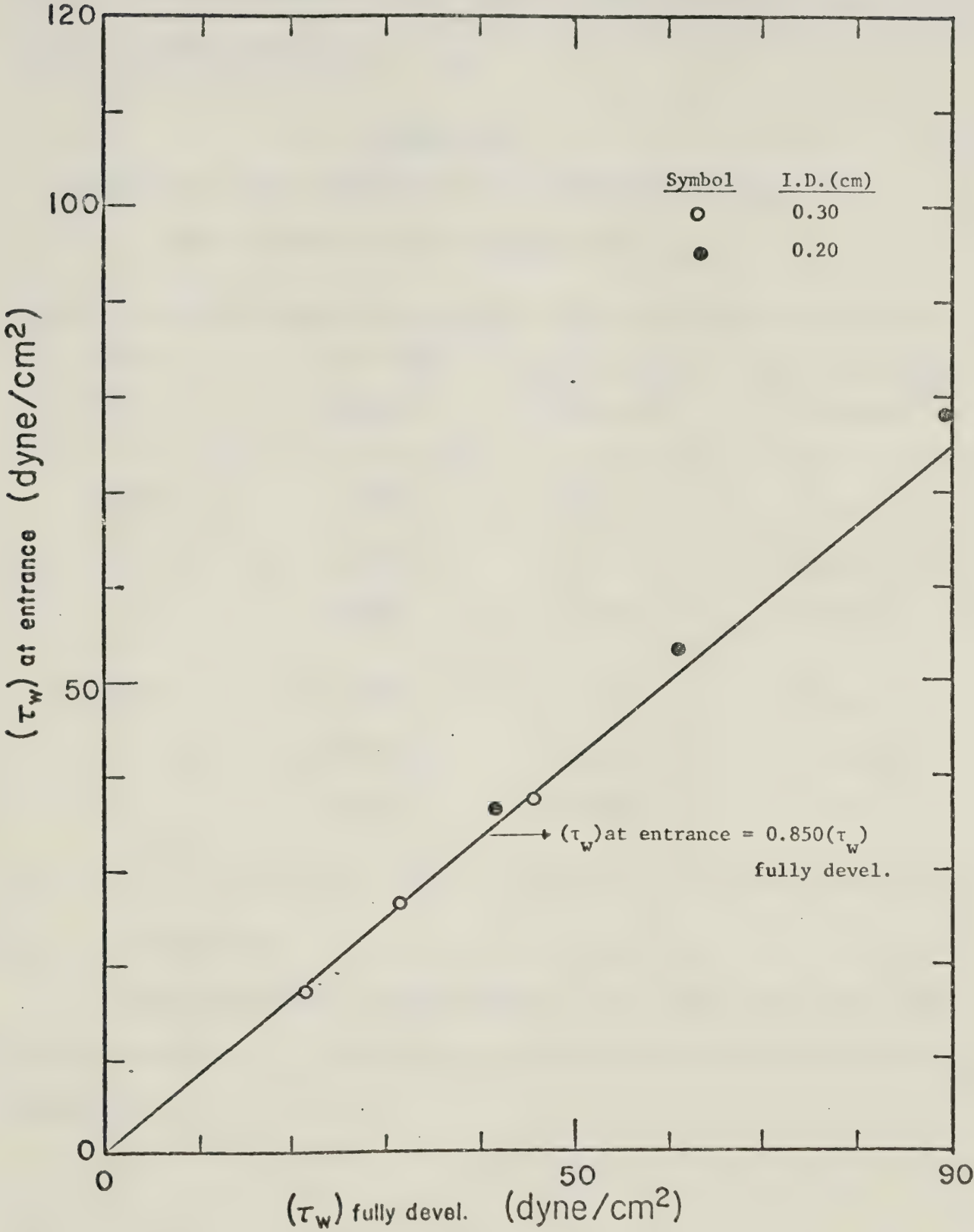
where $K_o' = K_o \left(\frac{3n+1}{4n} \right)^n$. The values of K_o' can be obtained from Equation (B-6) in Appendix B and equal to $2.24 \text{ (dynes/cm)}\text{-sec}^{0.55}$.

Therefore the wall shear stress (τ_w) of fully developed tube flow can be calculated from the following equation,

$$\tau_w = 2.24 \left(\frac{8V}{D} \right)^{0.55} \quad (\text{IV-7})$$

The wall shear stress at entrance can be determined by Equation (IV-5) where $\left(\frac{dV_z}{dr} \right)_{r=R}$ can be estimated from the slope of the tangent (at $r=R$) to the velocity profile at the contraction. The results of the wall shear stress at entrance and the wall shear stress of fully developed tube flow are tabulated in Table (IV-2) and are plotted in Figure (IV-4).

FIGURE IV-4 WALL SHEAR STRESS AT CONTRACTION VERSUS
WALL SHEAR STRESS OF FULLY DEVELOPED TUBE FLOW



The solid line in Figure (IV-4) can be represented as Equation (IV-8).

$$(\tau_w) \text{ at entrance} = 0.850 (\tau_w) \text{ fully devel.} \quad (\text{IV-8})$$

The above equation also shows that the wall shear stress at entrance of the capillary is very close to the wall shear stress of the fully developed tube flow.

TABLE IV-2

Comparison of Wall Shear Stress at Contraction with Wall
Shear Stress of Fully Developed Tube Flow

I.D. (cm)	Flow Rate (cm/sec)	(τ_w) at entrance (dynes/cm ²)	(τ_w) fully devel. (dynes/cm ²)
0.20	0.1598	36.41	41.69
	0.3196	53.38	61.01
	0.6392	78.38	89.35
0.30	0.1598	17.27	21.34
	0.3196	26.57	31.25
	0.6392	37.32	45.75

IV.2 Cone Angles

The procedures for measurements of the cone angles were discussed in Chapter III. The measured cone semi-angles are tabulated in Appendix D.

IV.2-1 Initial Cone Semi-Angles

By using the Oldroyd-Maxwell constitutive model and assuming a sink flow model of the velocity field within the central core of the converging flow to obtain the physical components of the normal stresses, Metzner, et al (32) and Murch (33) suggested a dimensionless group $(r^{*3}/\theta_{fl} Q^*)$ which is the reciprocal of the relaxation time - deformation rate product. The deformation rate (Q^*/r^{*3}) at the orifice was given by Metzner (31) as (Q^*/R^3) which was in terms of the orifice radius (R). By using the diameter of the capillary tube (D) instead of the radius (R), a plot of initial cone semi-angle (ϕ_o) versus a dimensionless group $(D^3/\theta_o Q)$ on the logarithmic coordinates is shown in Figure (IV-5) θ_o , the relaxation time at zero shear, is assumed equal to 1.0 sec (10). In Figure (IV-5), two parallel straight lines with slopes equal to 0.6 are found for the 0.20 and 0.30 cm I.D. capillary tubes. The data in Figure (IV-5) can be reasonably represented by Equations (IV-9) and (IV-10) which are shown as the solid lines.

$$\phi_o = 22.15 \left(\frac{D^3}{\theta_o Q} \right)^{0.6} \quad \text{for 0.20 cm I.D.} \quad (\text{IV-9})$$

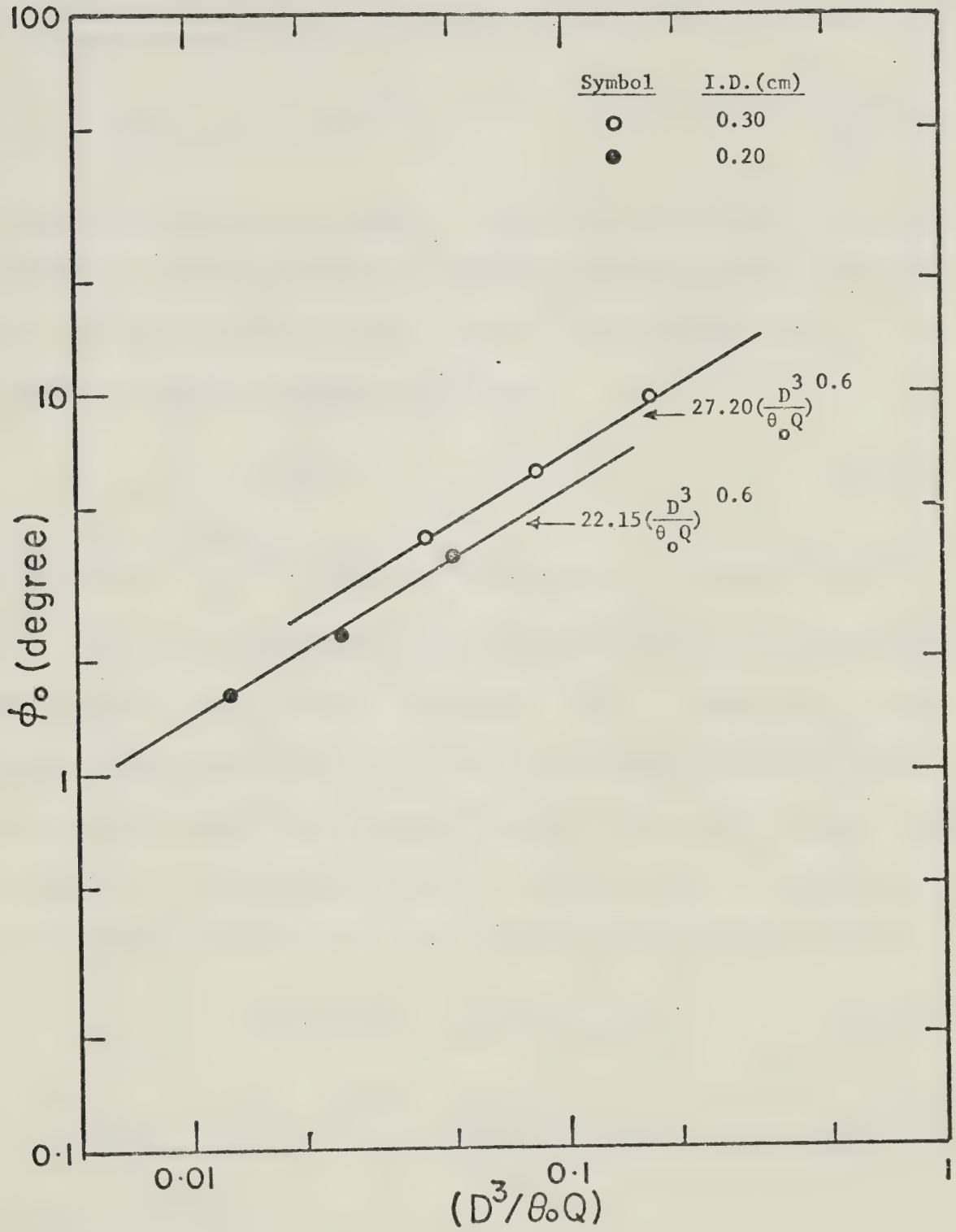
$$\phi_o = 27.20 \left(\frac{D^3}{\theta_o Q} \right)^{0.6} \quad \text{for 0.30 cm I.D.} \quad (\text{IV-10})$$

where ϕ_o is in degrees. Considering Equations (IV-9) and (IV-10) and rearranging them, one can obtain an equation in the form of:

$$\phi_o = f(D) \left(\frac{D}{V} \right)^{0.6} \quad (\text{IV-11})$$

where V is the average velocity at the contraction and f(D) is a function of the capillary tube diameter (D).

FIGURE IV-5 INITIAL CONE SEMI-ANGLE VERSUS $(\frac{D^3}{\theta_0 Q})$



Oliver and Bragg (38) suggested that a single equation could not be expected to give exact cone semi-angles for a range of visco-elastic solutions. However, for one solution and a limited range of operating variables this might be possible. An empirical equation for initial cone semi-angle (ϕ_o) of the form:

$$\sin \phi_o = K' R^{s'} V^{t'} \quad (\text{IV-12})$$

was suggested by Oliver and Bragg. Considering the small initial cone semi-angles in Oliver's study for low flow rates ($\phi_o < 10^0$), where the initial cone semi-angles increase when the flow rate decreases, it is reasonable to rewrite Equation (IV-12) as:

$$\phi_o = K D^s V^t \quad (\text{IV-13})$$

since the ratio $\left(\frac{\sin \phi_o}{\phi_o}\right)$ approaches unity when ϕ_o is a small angle.

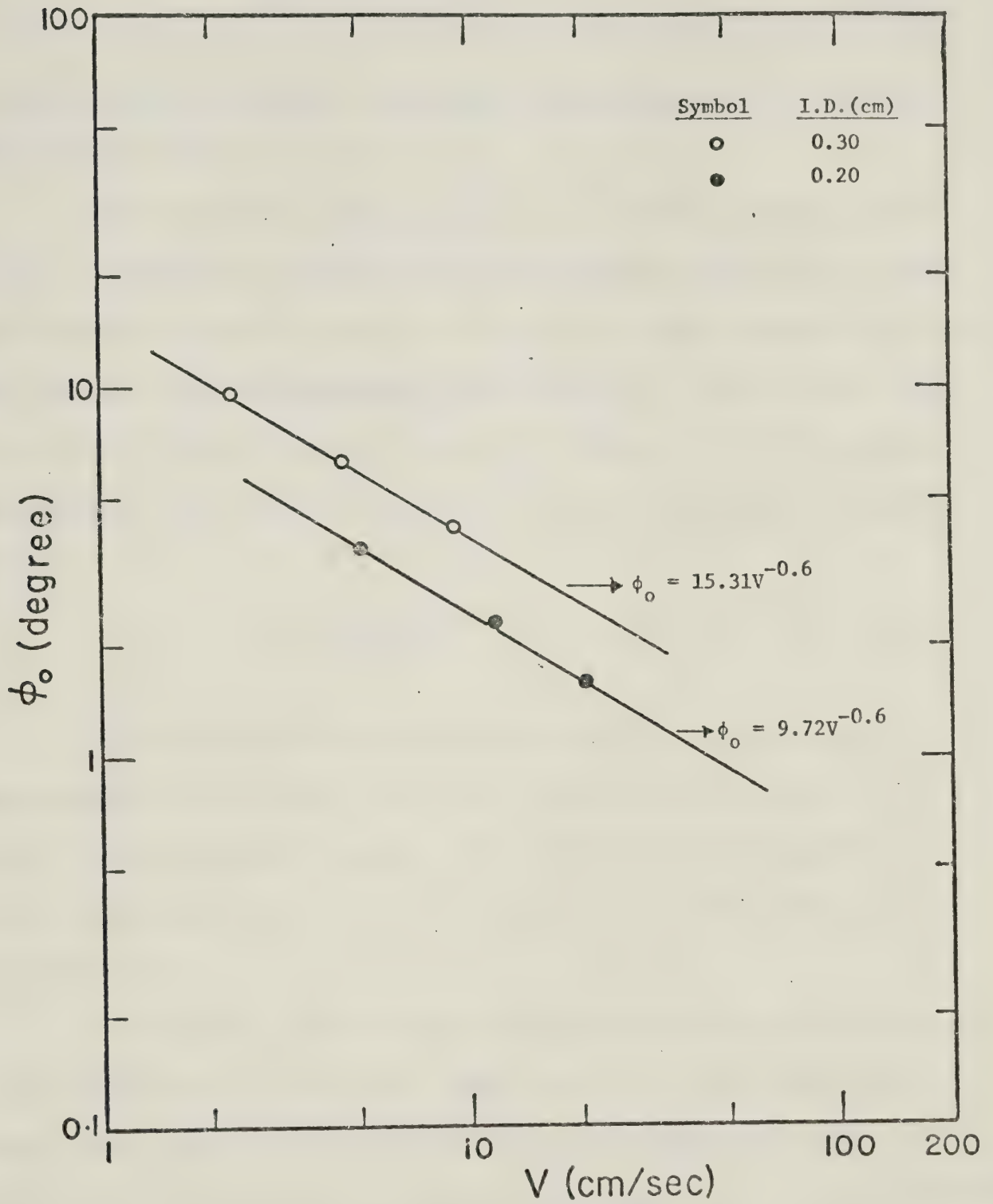
Comparing Equations (IV-11) and (IV-13), these two equations are the same with $f(D) = K D^{s+t}$ (where $t = -0.6$). Therefore, a plot of initial cone semi-angles (ϕ_o) versus the average velocity at the contraction (V) should form a set of straight lines with the same slope equal to -0.6. The plots are shown in Figure (IV-6). Equations (IV-14) and (IV-15) are shown as the solid lines in Figure (IV-6).

$$\phi_o = 9.72 V^{-0.6} \quad \text{for } 0.20 \text{ cm I.D.} \quad (\text{IV-14})$$

$$\phi_o = 15.31 V^{-0.60} \quad \text{for } 0.30 \text{ cm I.D.} \quad (\text{IV-15})$$

where ϕ_o is in degrees.

FIGURE IV-6 INITIAL CONE SEMI-ANGLE VERSUS AVERAGE VELOCITY AT CONTRACTION



The values of K and s in Equation (IV-13) can be easily found from Equations (IV-9) and (IV-10) or from Equations (IV-14) and (IV-15). Then an empirical equation:

$$\phi_o = 57.33 D^{1.1} V^{-0.6} \quad (\text{IV-16})$$

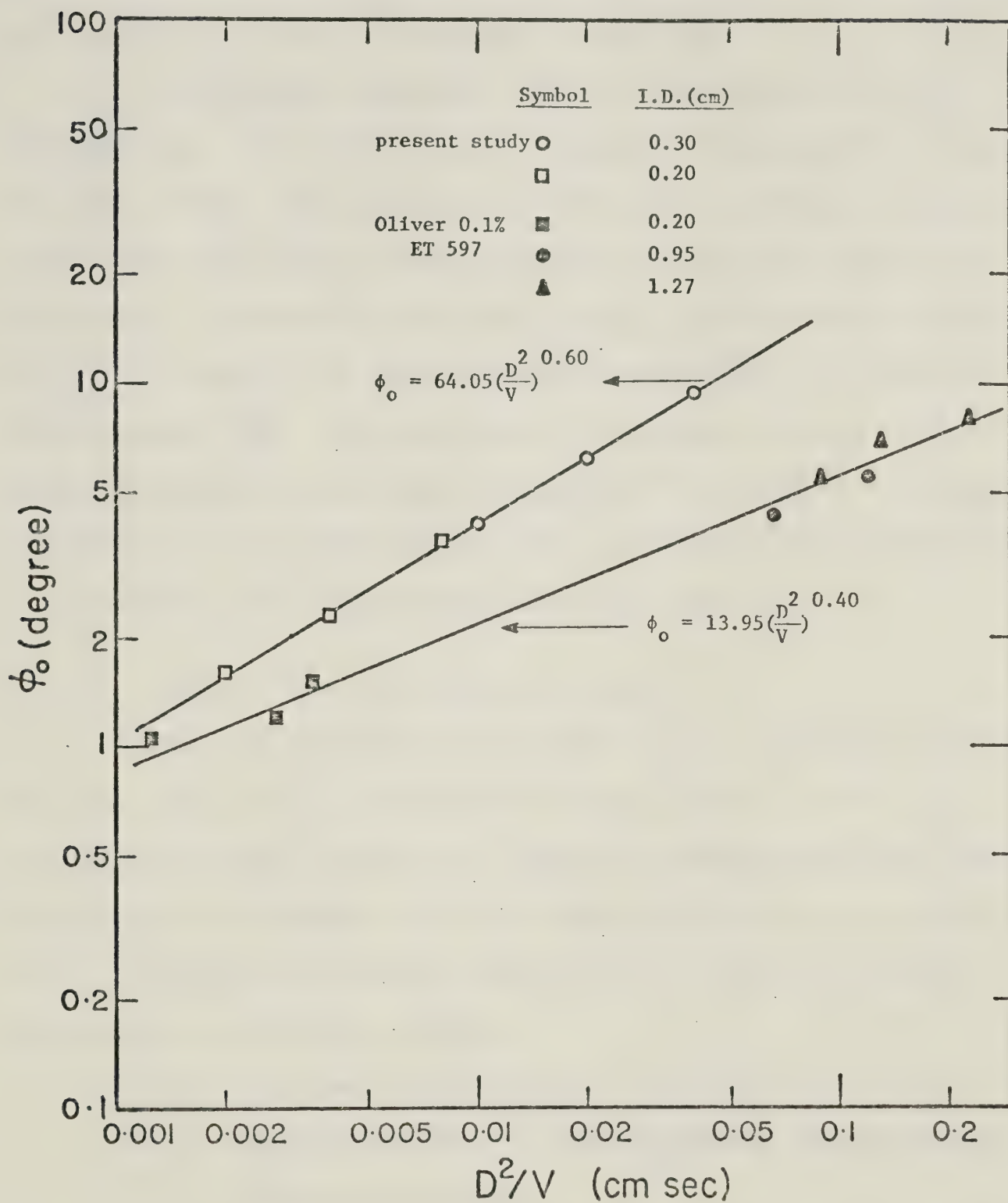
can approximately represent the initial cone semi-angle for the 0.2% Separan AP-30 solution.

From Equation (IV-16) the group $(D^{1.1}/V^{0.6})$ or approximately (D^2/V) is suggested to represent the relationships between the velocity field within the control core, and the capillary tube diameter and flow rate instead of the dimensionless group $(D^3/\theta_o Q)$. Figure (IV-7) shows a plot of the initial cone semi-angle (ϕ_o) versus (D^2/V) on logarithmic coordinates. The data in Figure (IV-7) can be represented by Equation (IV-17).

$$\phi_o = 64.05 \left(\frac{D^2}{V}\right)^{0.6} \quad (\text{IV-17})$$

Thus for 0.2% Separan AP-30, the initial cone semi-angle is approximately represented by Equation (IV-17) for the values of $(\frac{D^2}{V})$ between 0.0020 and 0.0398 cm sec. The initial cone semi-angles calculated from Equation (IV-17) have an average error less than 3% of the measured values.

The initial cone semi-angles measured by Oliver (38) for 0.1% ET 597 solution at low flow rate, where the initial cone semi-angles increase when the flow rate decrease, are also plotted in Figure (IV-7). Those Oliver's data can be reasonably represented by $\phi_o = 13.95 (D^2/V)^{0.4}$. The values of s and t in Equation (IV-13) corresponding to the Oliver's condition are 0.8 and -0.4 respectively which are not the same as the

FIGURE IV-7 INITIAL CONE SEMI-ANGLE VERSUS (D^2/V) .

values in this study. This result indicates that the values of s and t in Equation (IV-13) are constant only for one concentration of a polymer solution in the limit range of operating variables, they will change for different concentrations, different polymer solutions, or different range of operating variables as mentioned by Oliver (38).

Unfortunately, the group (D^2/V) in Equation (IV-17) is not dimensionless. But being an empirical equation determined by the experiment data in this study, Equation (IV-17) is still valid to represent the initial cone semi-angle in the limited range of operating variables in this study. A possible dimensionless group of these variables would be $(D^4/\theta_o^3 V_v^2)$ which is the ratio of Reynold number $(\frac{\rho V D}{\mu})$ to the cube of Deborah number $(\frac{\theta V}{D})$. From the data in this study, the value of this group was estimated approximately between 4×10^{-5} and 4×10^{-3} . In view of the large radial dependence of velocity, the necessity of including shearing viscosity as an important variable is not surprising.

IV.2.2 Upstream Cone Semi-Angles Development

Since the initial cone semi-angle (ϕ_o) is a function of (D^2/V) , the cone semi-angle (ϕ) are plotted in Figure (IV-8) to (IV-10) as a function of the same group so as to compare the development of the cone semi-angles for different I.D. of the capillary tube at the same flow rate. From the data plotted in Figures (IV-8) to (IV-10), several observations can be made as follows:

- (i) For some capillary tube, the gradient of the cone semi-angles along the axial locations increases as the flow rate decreases.

FIGURE IV-3 UPSTREAM CONE SEMI-ANGLE DEVELOPMENT; $Q = 0.1593 \text{ cm}^3/\text{SEC}$

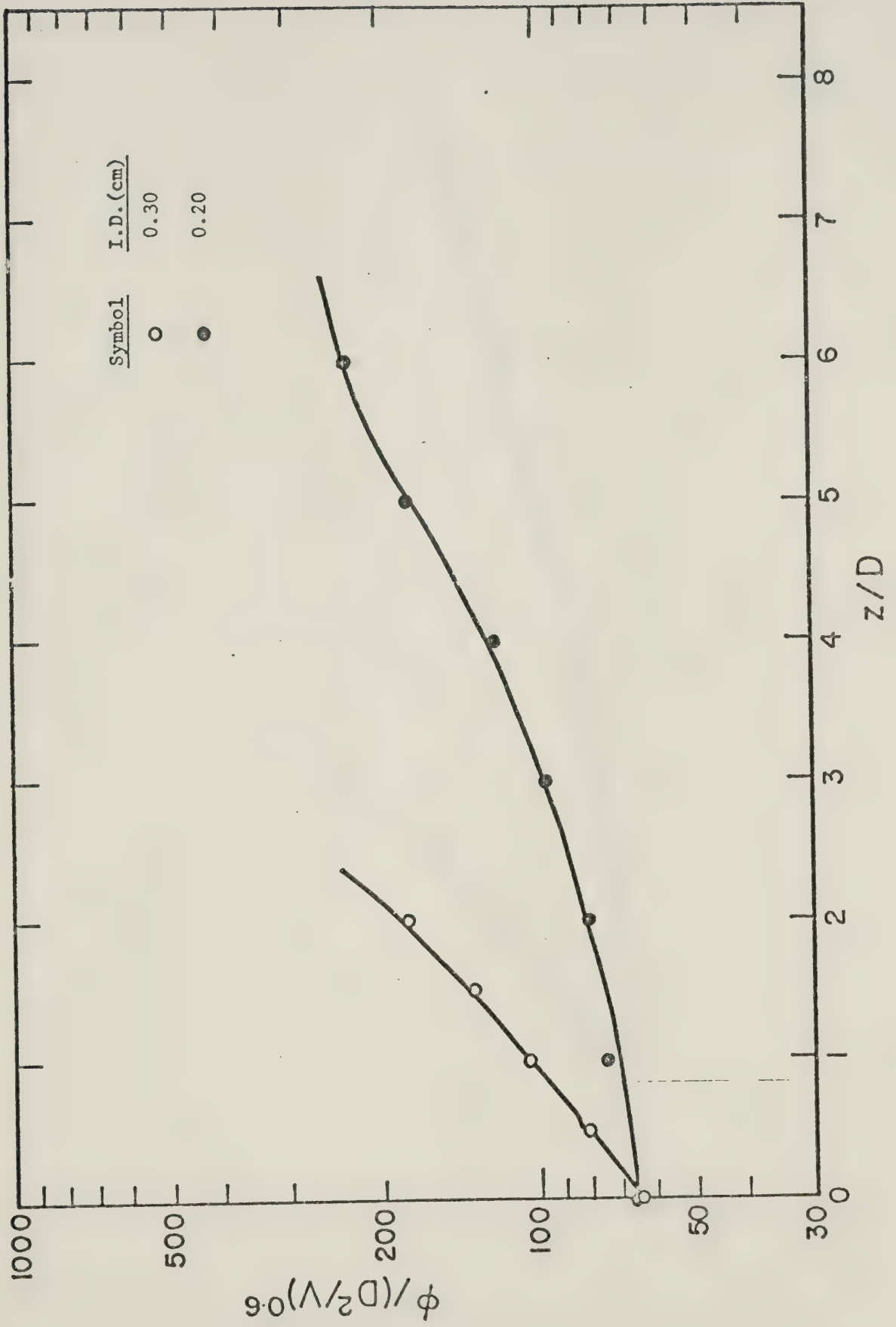


FIGURE IV-9 UPSTREAM CONE SEMI-ANGLE DEVELOPMENT; $Q = 0.3196 \text{ cm}^3/\text{SEC}$

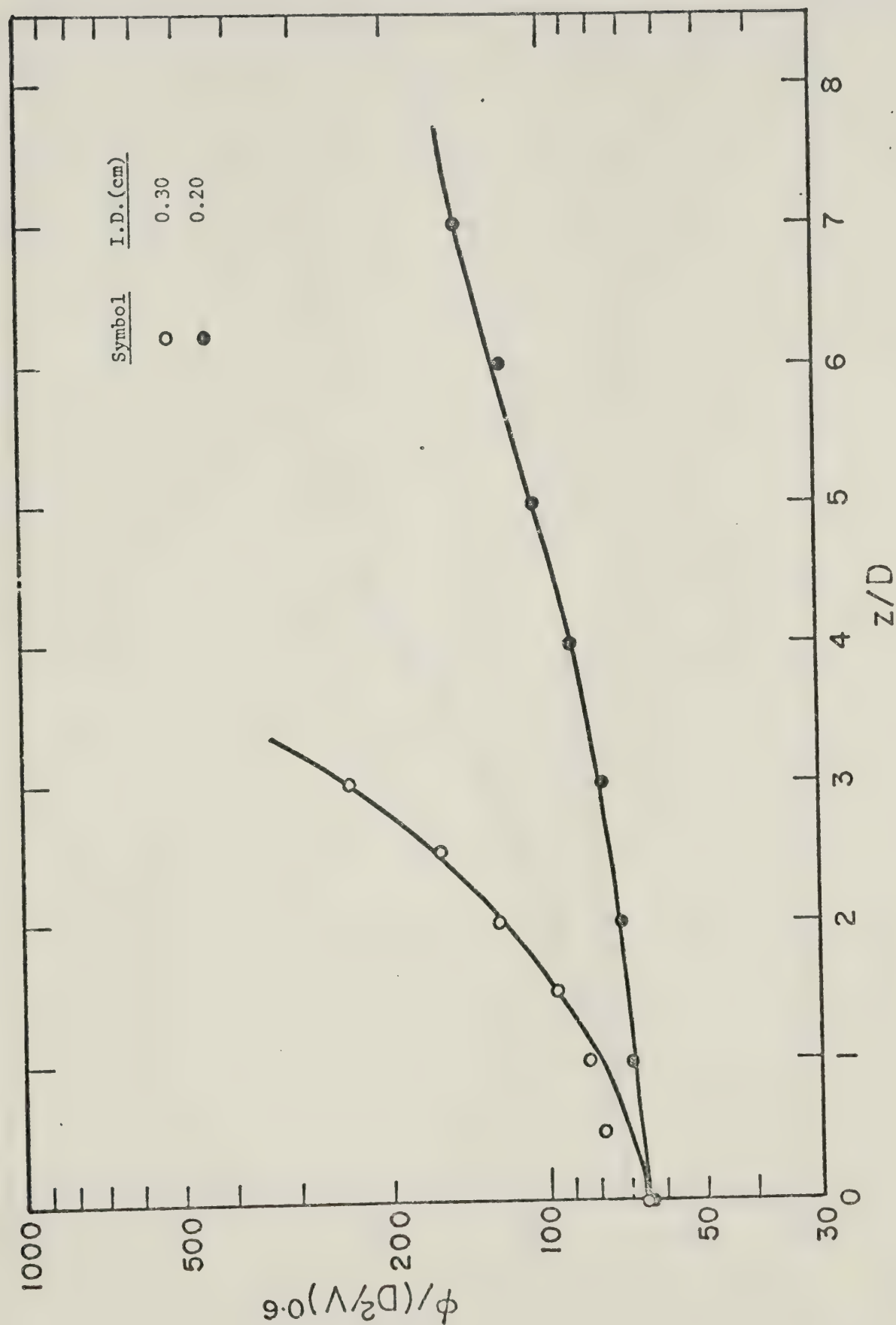
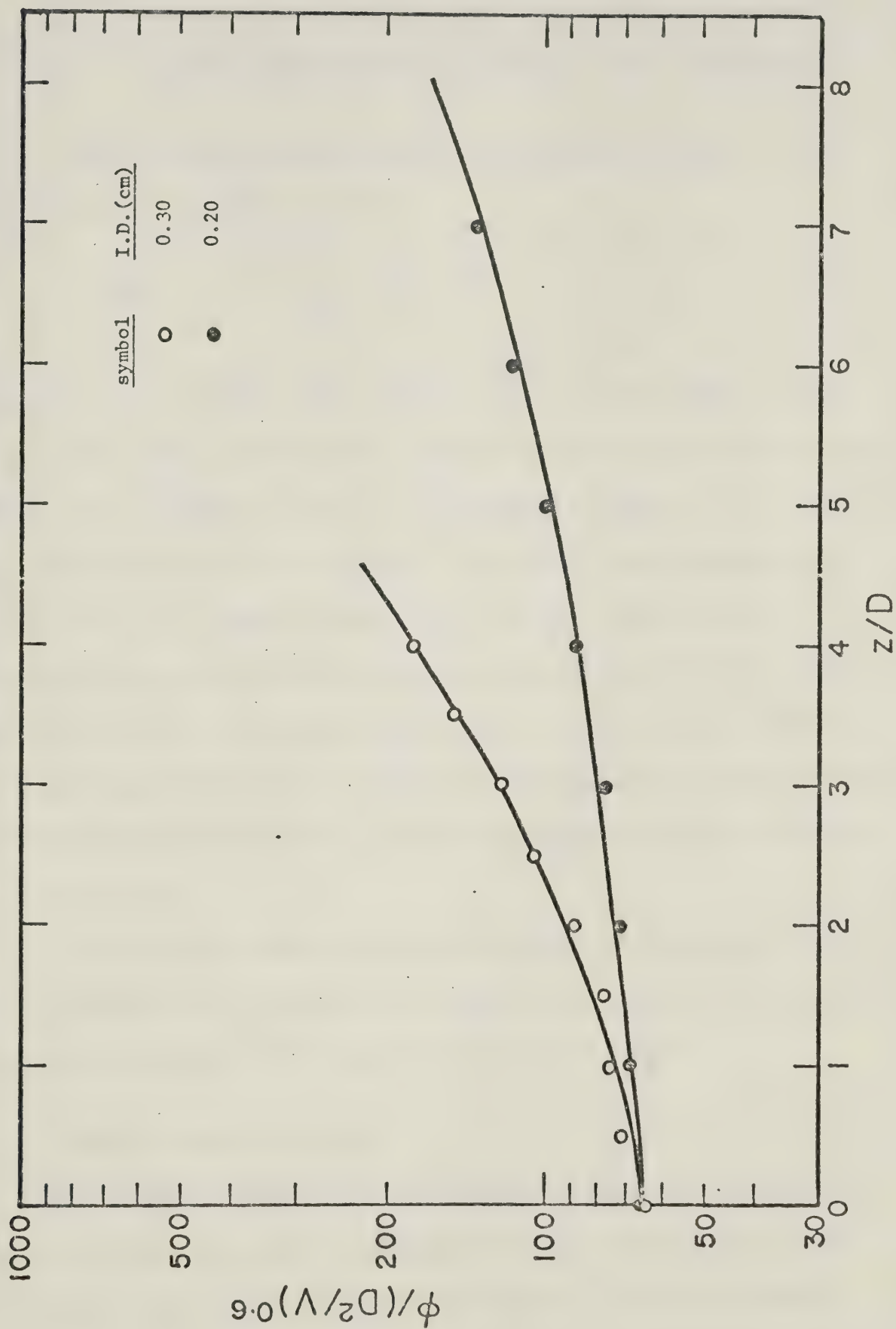


FIGURE IV-10 UPSTREAM CONE SEMI-ANGLE DEVELOPMENT; $Q=0.6392 \text{ cm}^3/\text{sec}$ 

- (ii) For the same flow rate, the gradient of the cone semi-angles along the axial locations increases as the diameter of the capillary tube increases.

The upstream cone semi-angles development predicted by K-1 model was shown in Chapter II, to be

$$\tan \phi = - \frac{C_1}{2D} d^2 \quad (IV-18)$$

On logarithmic coordinates the slope of a plot of the tangent of the cone semi-angle ($\tan \phi$) versus the diameter of the central core (d) will be equal to +2 if Equation (IV-18) is correct. Figures (IV-11) and (IV-12) show the data of this study. The solid lines representing Equation (IV-18) has good agreement with the data only at axial locations further upstream from the entrance and give less than experimental values of the cone semi-angles near the contraction. Because of this poor agreement with the data near the contraction, the K-1 model is not suitable in representing the upstream cone semi-angles development in this study.

The cone semi-angles and the diameters of the central core at several upstream axial locations are tabulated in Appendix D and serve to give a description of the shape of the central core.

IV.3 Central Core Velocities

To obtain an empirical description of the velocity profiles within the central core which would describe the dependence on axial location, the three models described in Chapter II were considered.

FIGURE IV-11

UPSTREAM CONE SEMI-ANGLES DEVELOPMENT; K-1 MODEL; 0.20 cm I.D. CAPILLARY TUBE

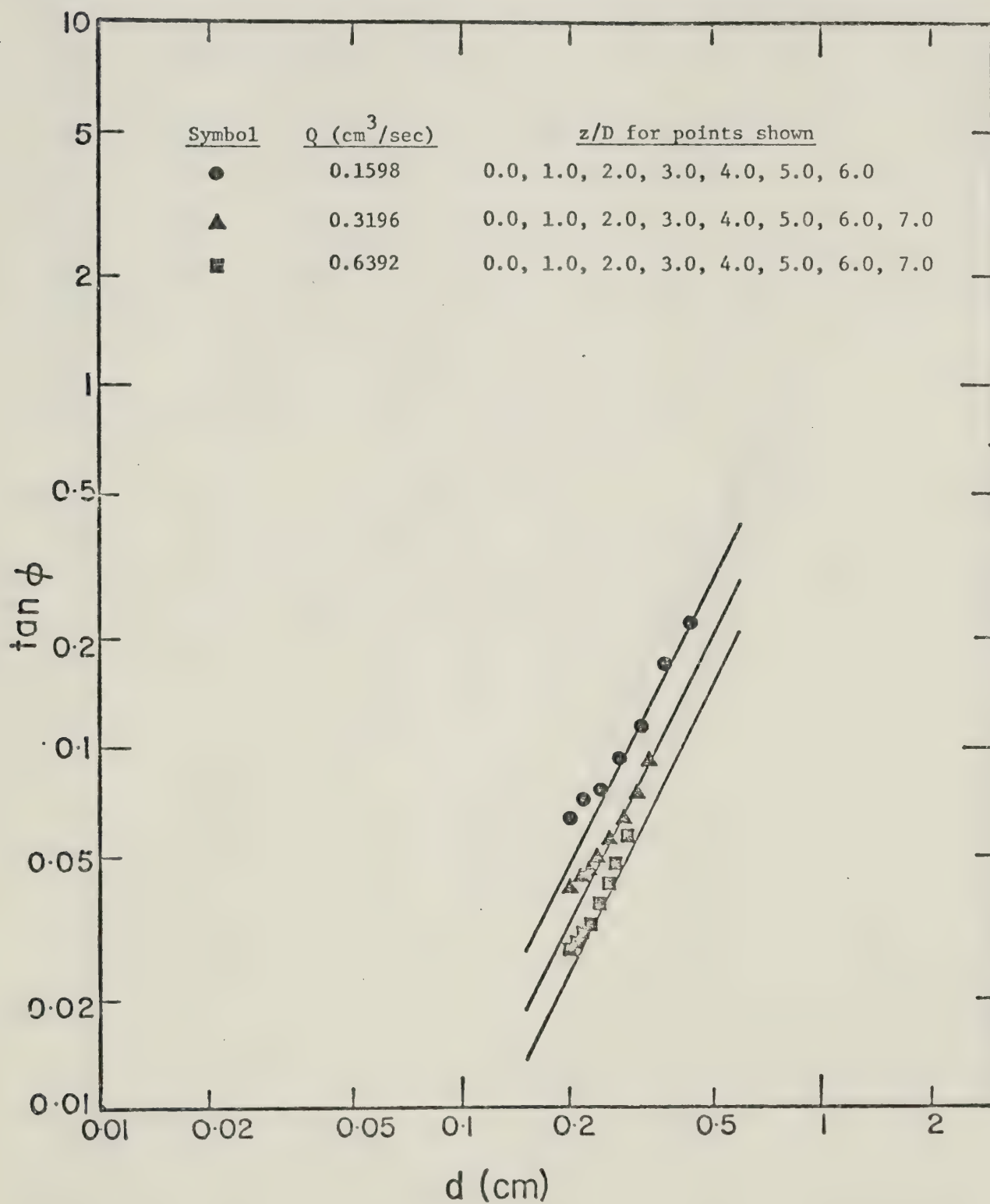
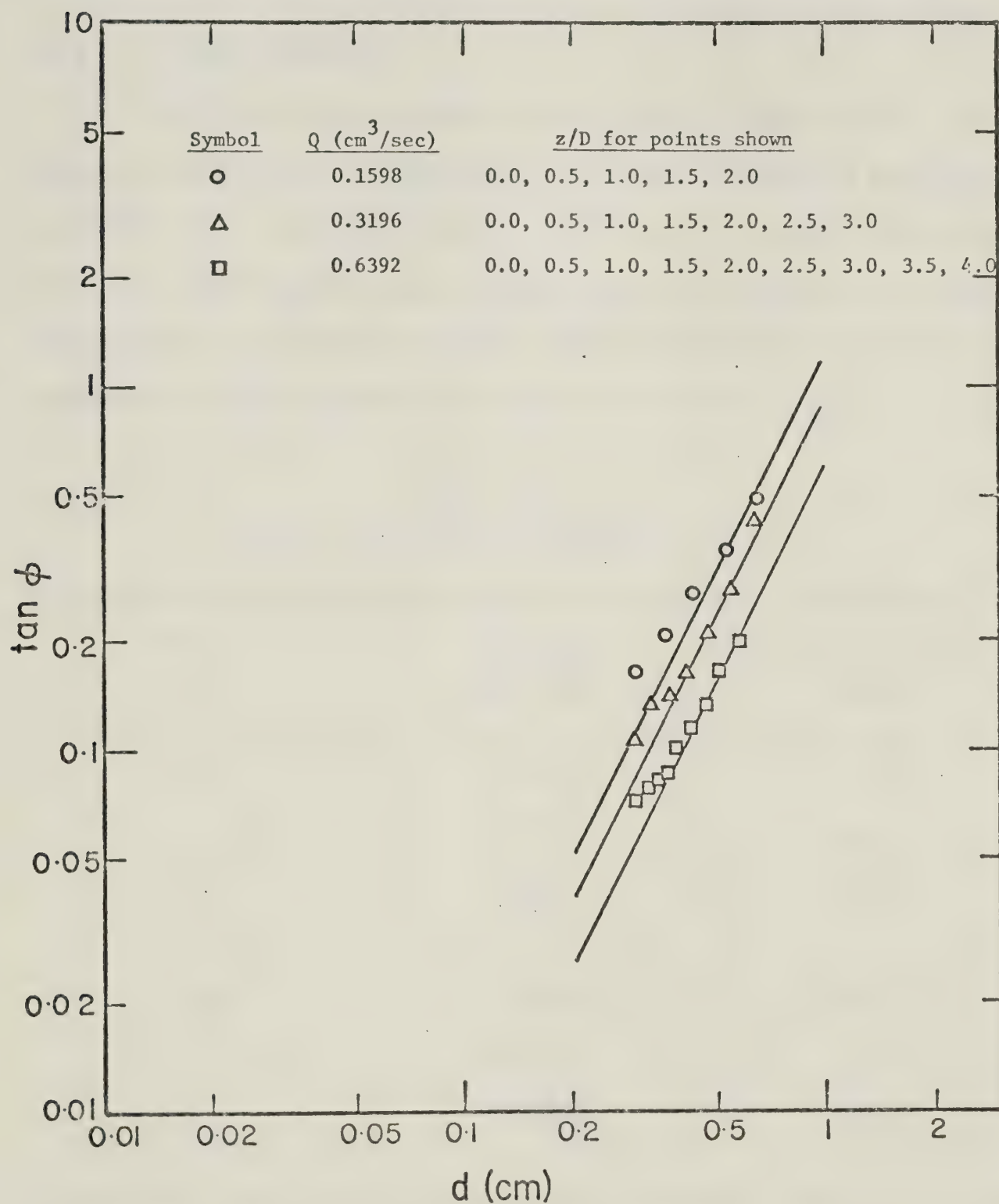


FIGURE IV-12

UPSTREAM CONE SEMI-ANGLE DEVELOPMENT; K-1 MODEL; 0.30 cm I.D. CAPILLARY TUBE



Only the centerline velocities were considered to obtain the relationship of the dependence on axial location. The centerline velocities at different axial locations for several flow rates are tabulated in Appendix C.

IV.3-1 Sink Flow Model

As described in Chapter II and shown by Figure (II-1), the velocity field within the converging region may be analyzed employing a spherical polar coordinate system. The origin is located within the tube at a point determined by extending the converging streamlines to their intersection. The location of the origins of the sink flow model as determined by the streamlines are tabulated in Table (IV-3).

TABLE IV-3
Location of Origin for Sink Flow Model

I.D. (cm)	Flow Rate (cm ³ /sec)	Location of Origin (-z) (cm)
0.20	0.1598	1.55
	0.3196	2.49
	0.6392	3.58
0.30	0.1598	0.91
	0.3196	1.38
	0.6392	2.09

By knowing the location of the origin of the sink, one can easily convert the cylindrical axial coordinate (z) into spherical radial coordinate (r^*) because only spherical coordinates are used to analyze the sink flow model.

Consider the centerline velocities, Equation (II-3) can be rewritten as:

$$\left(\frac{V_{z,c}}{V}\right) = \frac{Q^*}{VD^2} \left(\frac{r^*}{D}\right)^{-2} \quad (\text{IV-19})$$

Therefore, the slope of a plot of $(V_{z,c}/V)$ versus (r^*/D) on the logarithmic coordinates will be equal to -2. Figures (IV-13) and (IV-14) show the data of this study where the solid lines are the straight lines with slopes equal to -2. The results have good agreement only near the entrance. This was also suggested by Kanel (26) and Murch (33). At larger upstream axial locations, the sink flow model predicts velocities that are higher than the experimental data. This is because at larger upstream axial locations the streamlines are curved and are not directed to the origin. This deviation increases when either the flow rate decreases or the diameter of the capillary tube increases.

For 0.30 cm capillary tube, at a flow rate of $0.1598 \text{ cm}^3/\text{sec}$ good agreement was for upstream axial locations as large as 1.0 diameter, while at $0.6392 \text{ cm}^3/\text{sec}$ agreement occurred for upstream axial locations as large as 1.5 diameters. For the 0.20 cm capillary tube, at a flow rate of $0.1598 \text{ cm}^3/\text{sec}$, agreement occurred for upstream axial locations as large as 1.5 diameters, while at $0.6392 \text{ cm}^3/\text{sec}$ agreement was up to 2.0 diameters.

FIGURE IV-13

CENTERLINE VELOCITY; SINK FLOW MODEL; 0.20 cm I.D. CAPILLARY TUBE

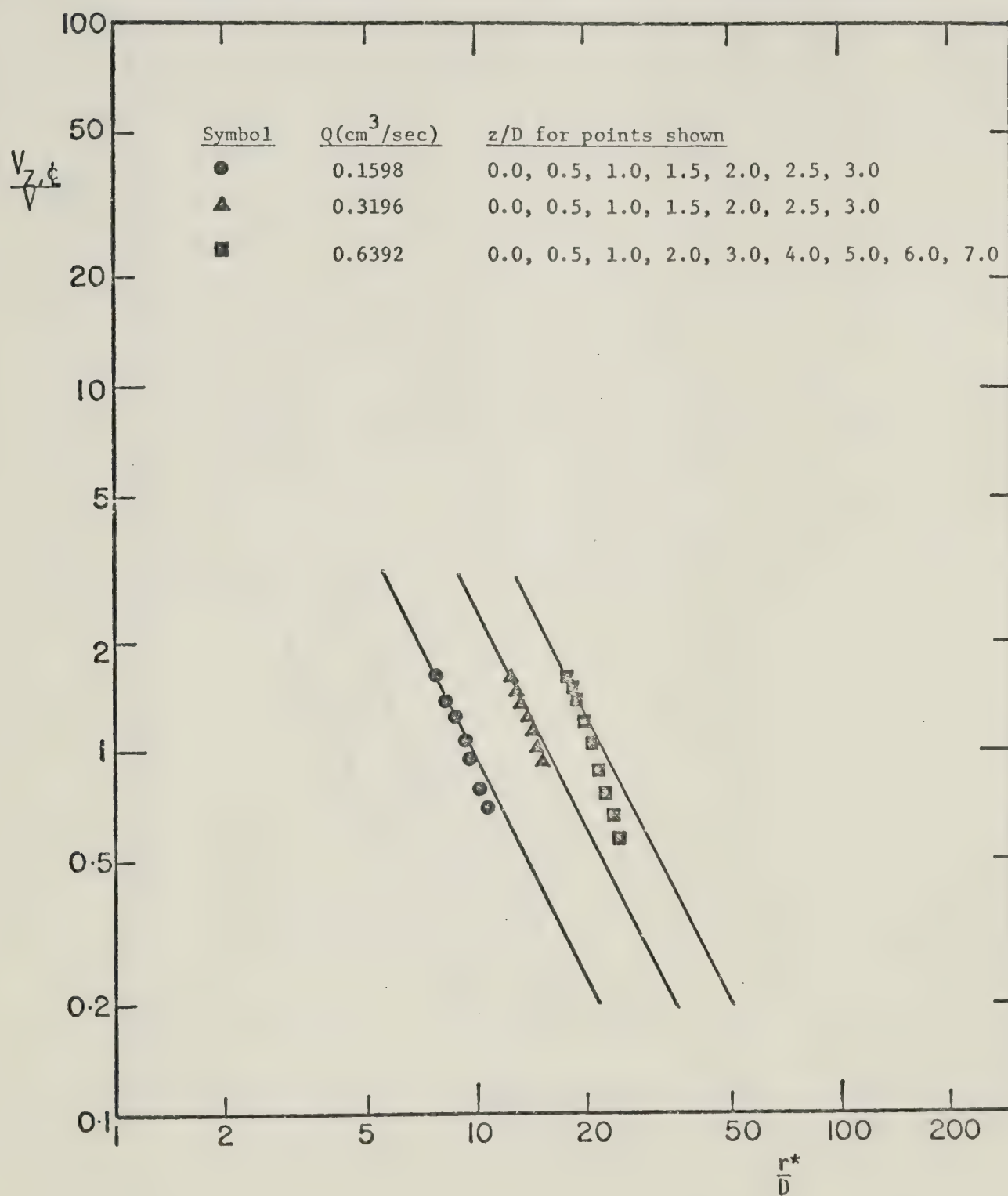
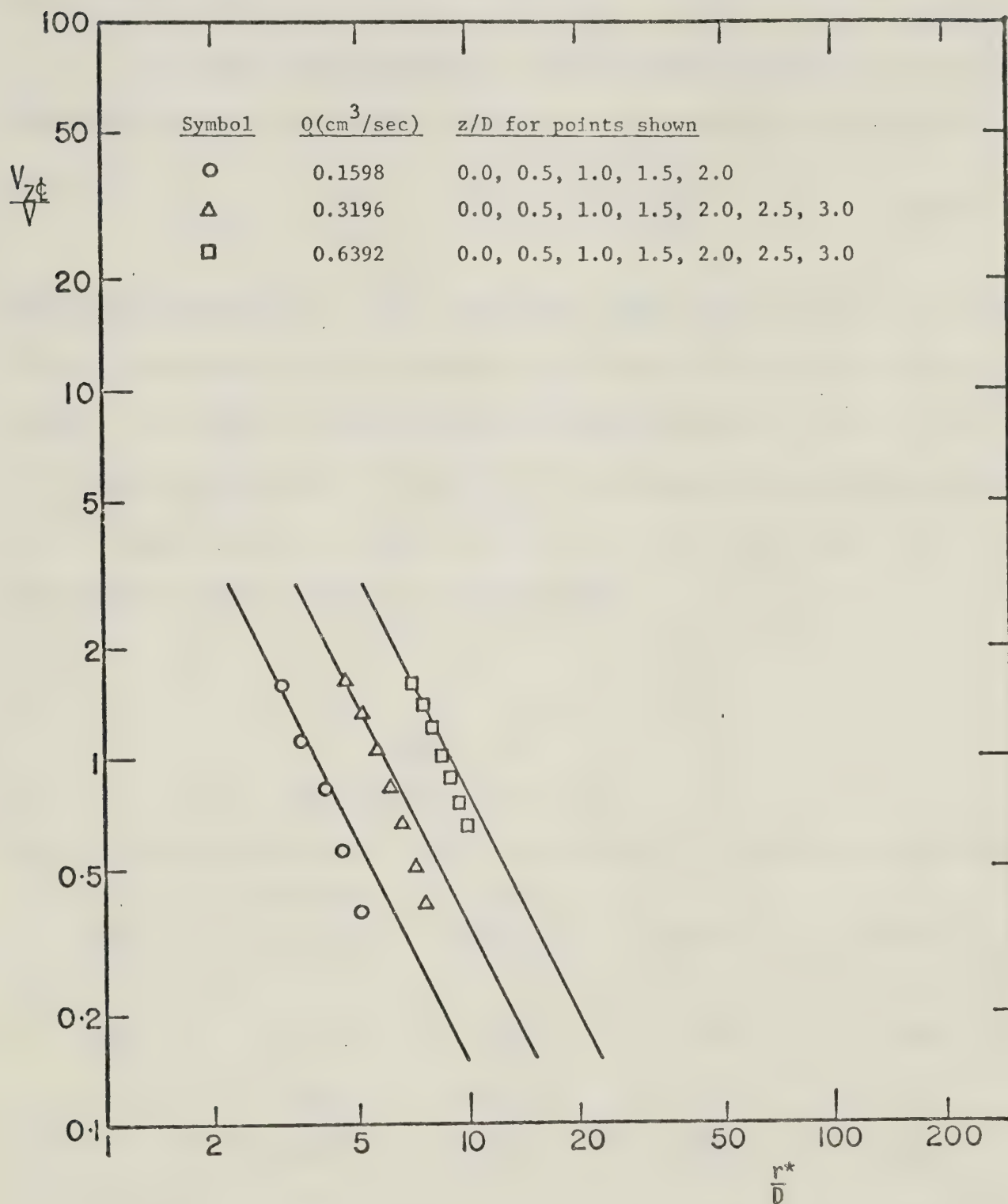


FIGURE IV-14

CENTERLINE VELOCITY; SINK FLOW MODEL; 0.30 cm I.D. CAPILLARY TUBE



Because of the poor quantitative as well as qualitative agreement with experiment data, the sink flow model is inadequate to represent the relationship between velocity along the centerline and axial location.

IV.3-2 K-1 Model

As described in Chapter II, the K-1 model suggests a quadratic dependence of axial centerline velocity on upstream axial location as,

$$V_{z,c} = K_1 + K_2 \left(\frac{z}{D}\right) + K_3 \left(\frac{z}{D}\right)^2 \quad (\text{IV-20})$$

The three parameters K_1 , K_2 and K_3 were found from the least square fit of the experiment data for different flow rates and diameter of capillary tubes. The values of these parameters are tabulated in Table (IV-4). From these values of K_1 , K_2 and K_3 , it is clear that the relationship $K_2^2 = 4K_1K_3$ required by Equation (II-11) is not satisfied. This demonstrates the inadequacy of the K-1 model.

TABLE IV-4
Parameters of K-1 Model

I.D. (cm)	Flow Rate (cm ³ /sec)	K_1 (cm/sec)	K_2 (cm/sec)	K_3 (cm/sec)
0.20	0.1598	8.3760	-2.1941	0.1957
	0.3196	16.3370	-2.7086	0.1450
	0.6392	32.3283	-4.3701	0.2009
0.30	0.1598	3.3450	-1.7700	0.2600
	0.3196	7.3720	-2.9519	0.3671
	0.6392	14.5700	-4.1914	0.4286

Typical experimental centerline velocities are shown in Figure (IV-15) and compared with the least square lines. Considering the differentiation of Equation (IV-20) with respect to axial location (z), yields:

$$V_{z,z,\zeta} = \left(\frac{K_2}{D}\right) + \left(\frac{2K_3}{D}\right) \left(\frac{z}{D}\right) \quad (\text{IV-21})$$

Typical stretch rates along centerline which are tabulated in Appendix E are shown in Figure (IV-16) and compared with Equation (IV-21).

Although the quadratic equation has good agreement with the centerline velocity data as shown in Figure (IV-15) and also with the stretch rates as shown in Figure (IV-16), it is not obvious how to obtain the relationships for the parameters K_2 and K_3 with flow rate and diameter of capillary tube (the ratio of K_1 to the average velocity at the contraction is approximately constant). In other words, when the flow rate or the diameter of the capillary tube is changed, one cannot predict what the changes of K_2 and K_3 will be. Therefore the K-1 and/or quadratic equations are considered to be of limited interest.

IV.3-3 Exponential Decay Model

As mentioned in Chapter II, the velocities within the central core can be expressed as a exponential function of the axial locations. Consider the centerline velocity, Equation (II-18) can be rewritten as:

$$V_{z,\zeta} = V_0 \exp \left(\alpha \left(\frac{z}{D} \right) \right) \quad (\text{IV-22})$$

Equation (IV-22) predicts that on semi-logarithmic coordinates, a plot of the centerline axial velocity ($V_{z,\zeta}$) versus the dimensionless axial location (z/D) will be a straight line with slope equal to α and intercept at $z/D = 0$ equal to V_0 .

FIGURE IV-15 TYPICAL CENTERLINE AXIAL VELOCITY; K-1 MODEL

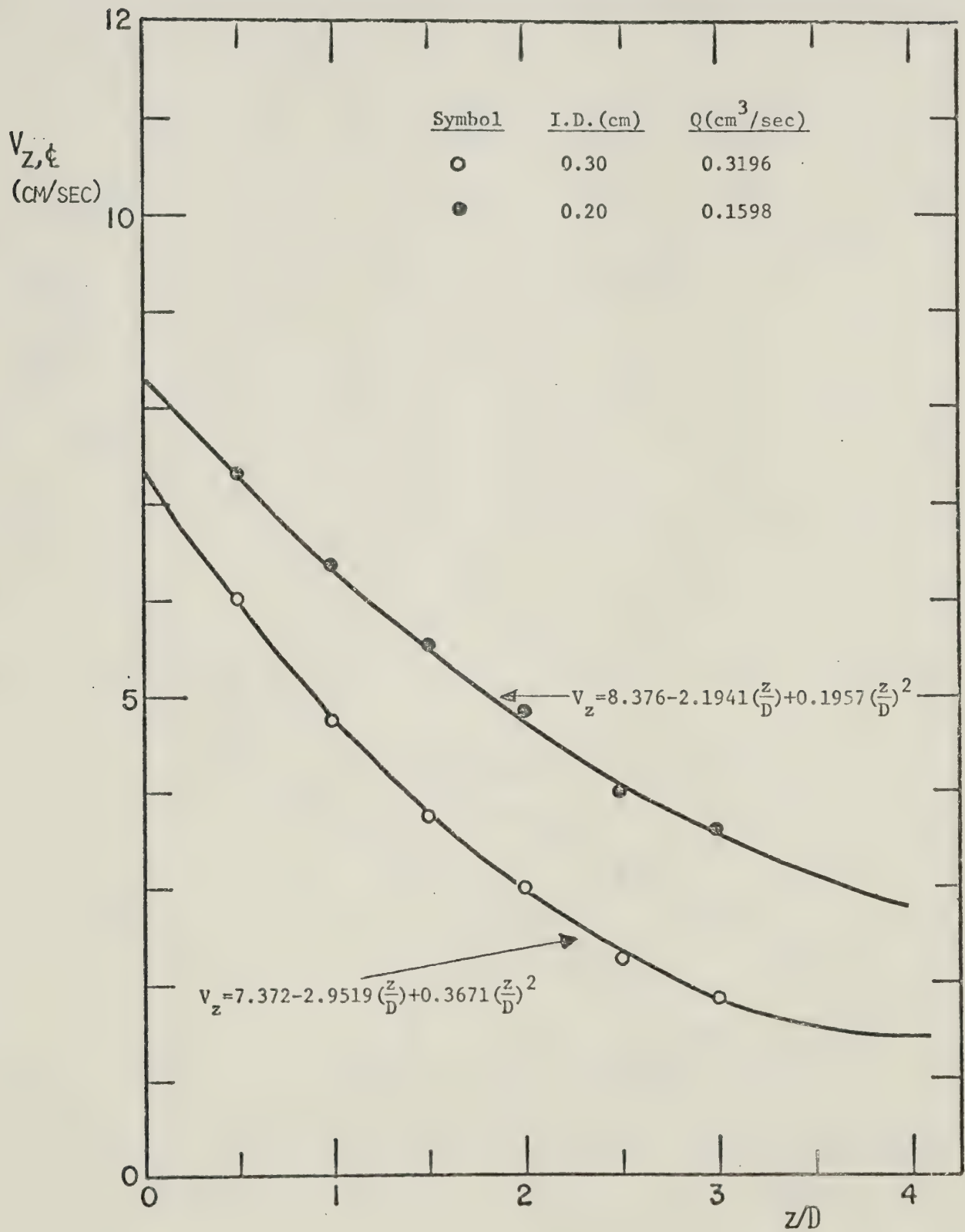
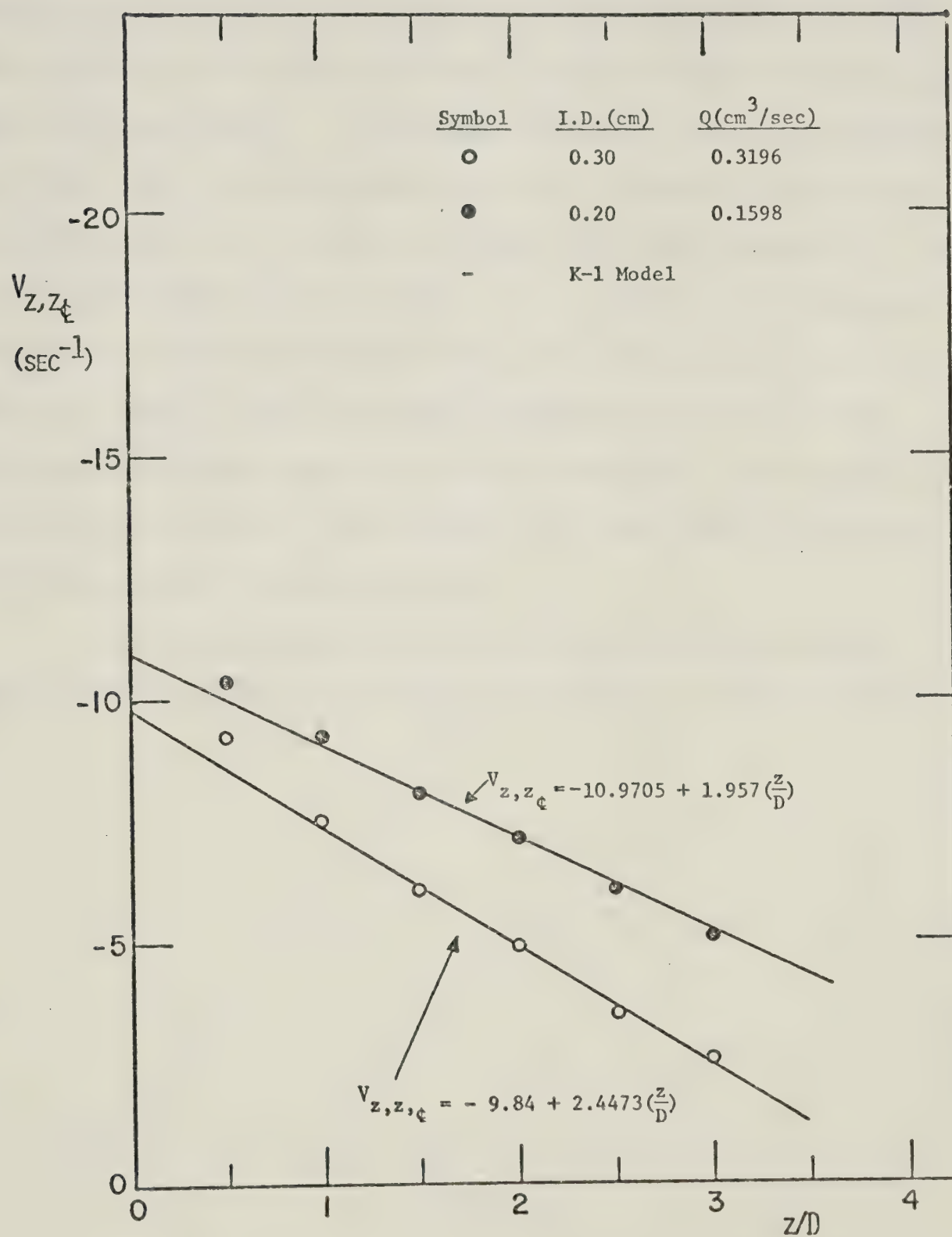


FIGURE IV-16 TYPICAL CENTERLINE STRETCH RATE; K-1 MODEL



Figures (IV-17) and (IV-18) show the experimental data of this study with the solid lines determined by the least square method. Good agreement with all of the centerline velocity data is obvious. In addition, some data from the other streamlines where experiment data can be measured as close as 0.25 diameters for the 0.30 cm I.D. capillary tube are plotted in Figure (IV-19) with solid lines again determined by the least square method. From Figures (IV-17) to (IV-19) the exponential decay model has good agreement with all the data not only for the centerline velocities but also for those of the other streamlines. The experimental data measured by Metzner, et al (32) for a 0.5% Separan AP-30 solution flowing from an 18" reservoir into a 3.76 cm I.D. tube are also plotted on semi-logarithmic coordinates in Figure (IV-20). These data which were chosen from the two streamlines very close to the centerline ($\phi = 0^{\circ}20'$) for two different flow rates have good agreement with the exponential decay model too.

The two parameters V_0 and α in Equation (IV-22) which were determined by the least square method are tabulated in Table (IV-5).

FIGURE IV-17 CENTERLINE AXIAL VELOCITY; EXPONENTIAL DECAY MODEL

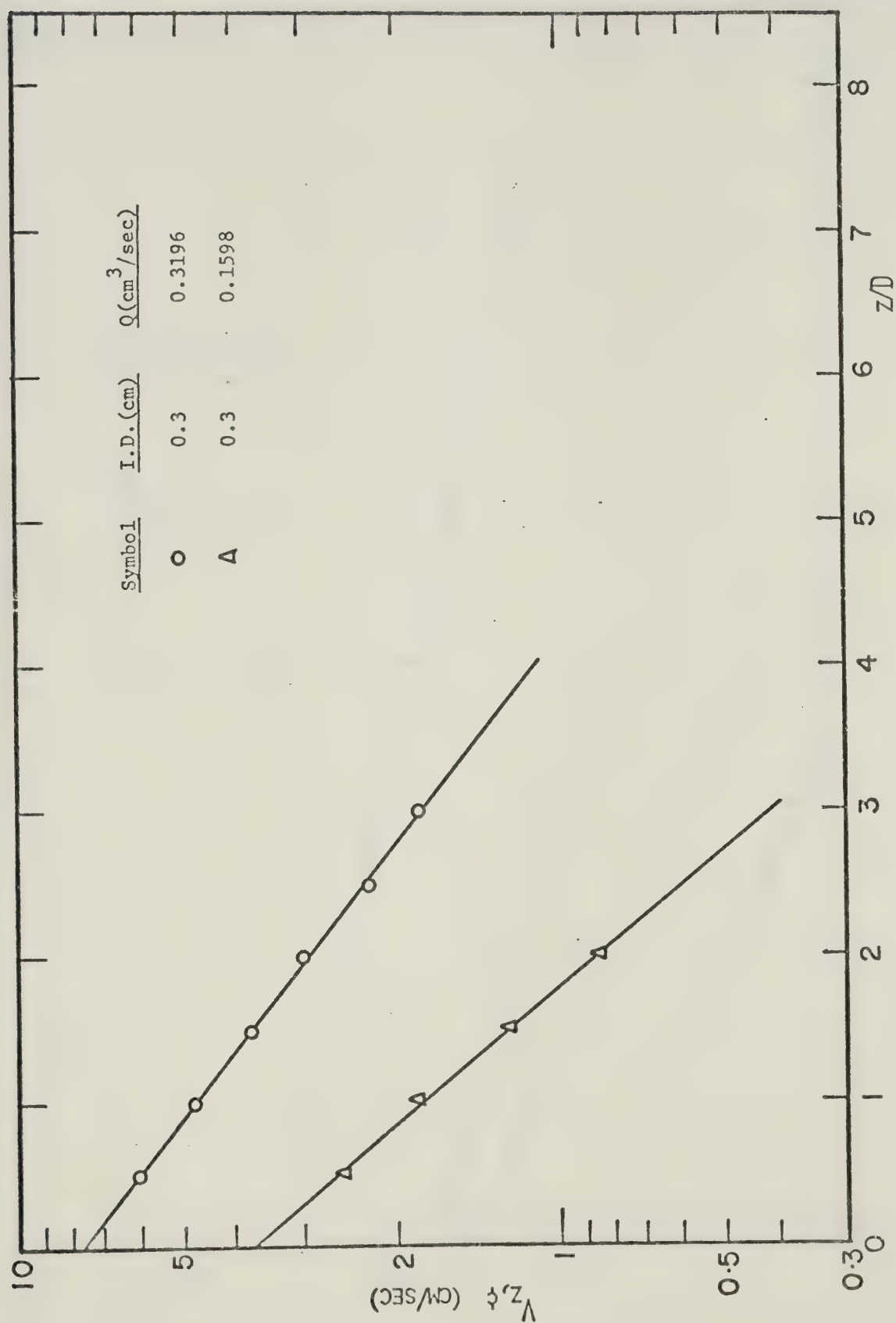


FIGURE IV-18 CENTER AXIAL VELOCITY EXPONENTIAL DECAY MODEL

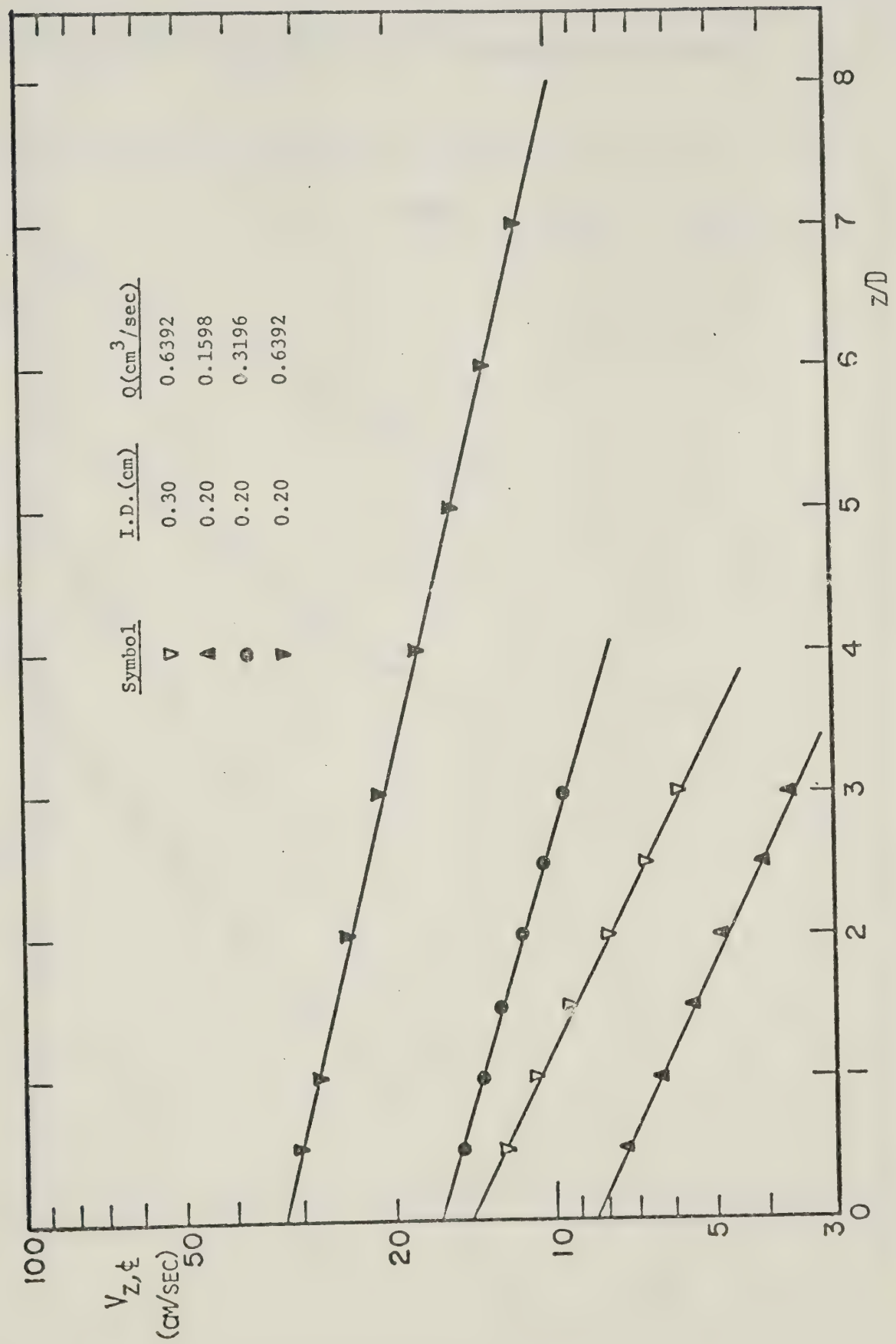


FIGURE IV-19 TYPICAL AXIAL VELOCITY; EXPONENTIAL DECAY MODEL

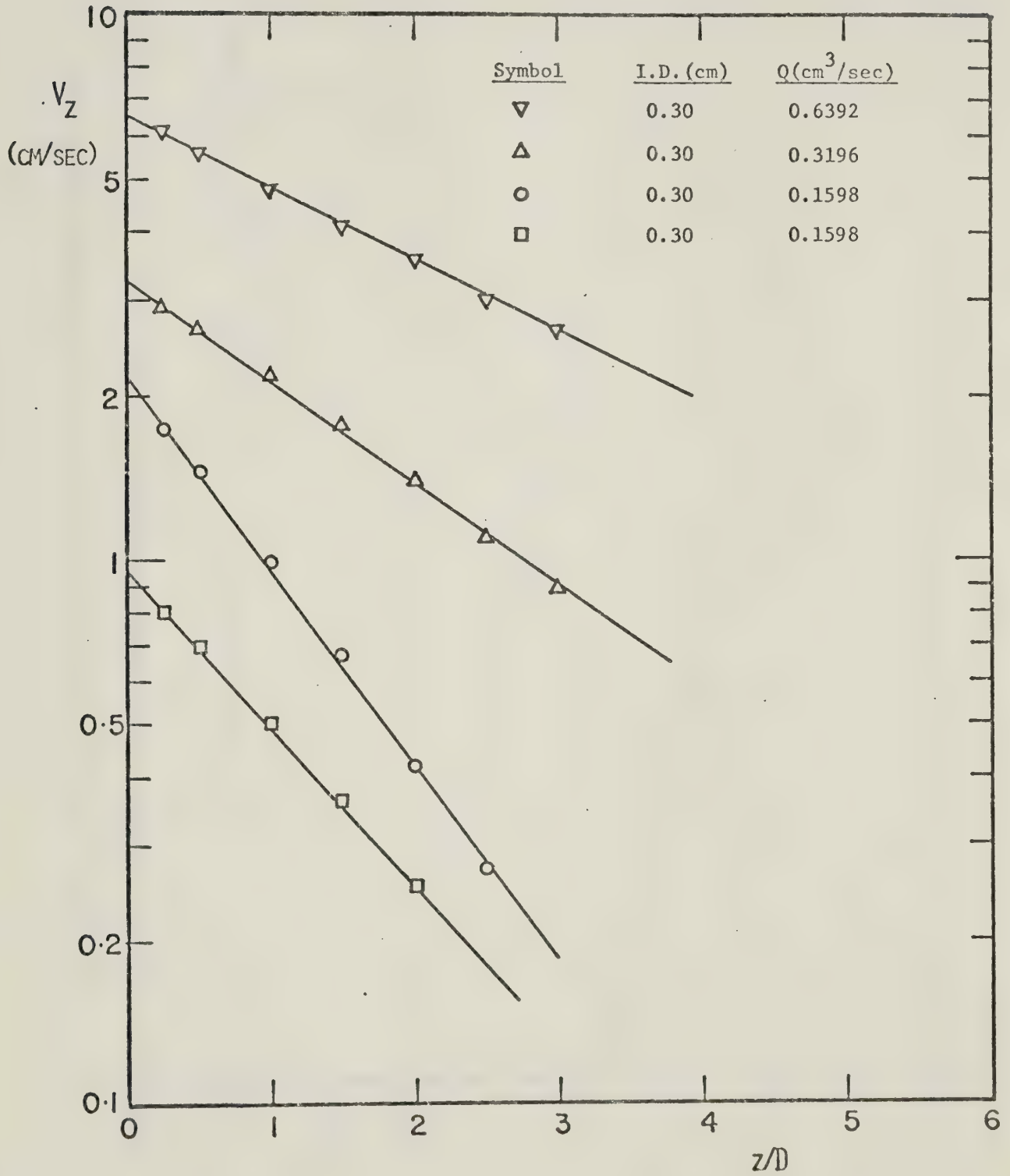


FIGURE IV-20 TYPICAL AXIAL VELOCITY (METZNER ET AL); EXPONENTIAL DECAY MODEL

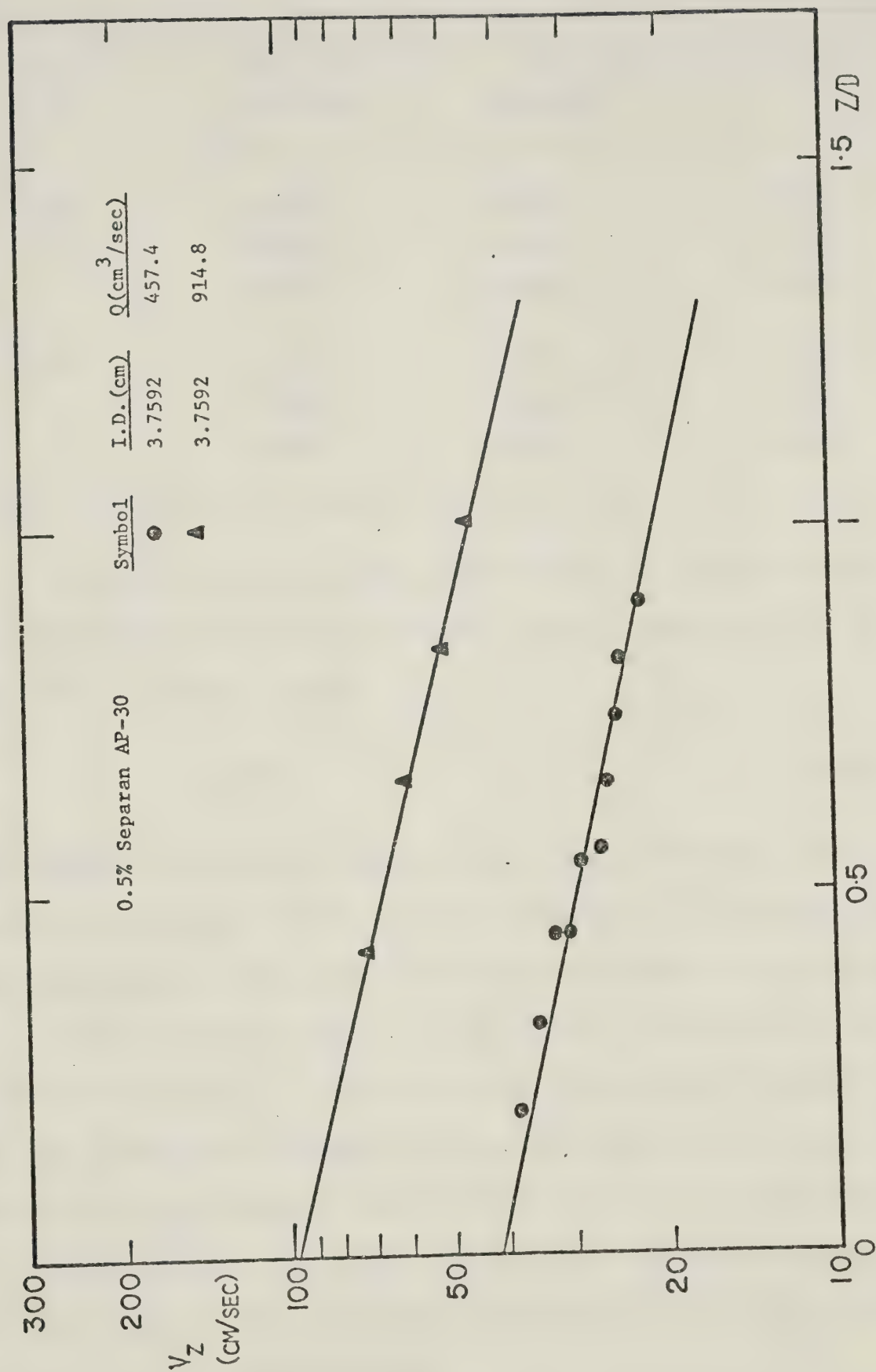


TABLE IV-5
Parameters of Exponential Decay Model

I.D. (cm)	Flow Rate (cm ³ /sec)	V ₀ (cm/sec)	α
0.20	0.1598	8.5071	-0.2902
	0.3196	16.5178	-0.1826
	0.6392	32.6827	-0.1486
0.30	0.1598	3.7177	-0.7289
	0.3196	7.6916	-0.4814
	0.6392	14.6698	-0.3078

A plot of the V₀ in Table (IV-5) versus the average velocity at the contraction (V) is shown in Figure (IV-21), the solid line is represented by Equation (IV-23):

$$V_0 = 1.645 V \quad (\text{IV-23})$$

Compare Equation (IV-23) with Equation (IV-1), the difference between the extrapolated values of the centerline velocities at the contraction from the exponential decay model and the eye fit method is less than 2%.

Since, in Section (IV-2.1), the initial cone semi-angle can be represented by a group $(\frac{D^2}{V})$, this group was also used when trying to obtain the relationships between the parameter α and the flow rate and diameter of capillary tube. Figure (IV-22) shows a plot of the parameter α versus $(\frac{D^2}{V})$ on logarithmic coordinates. The data in Figure (IV-22) can be reasonably represented by Equation (IV-24) which is shown as the solid line in Figure (IV-22):

$$\alpha = -4.04 \left(\frac{D^2}{V}\right)^{0.545} \quad (\text{IV-24})$$

FIGURE IV-21
PARAMETER V_0 OF EXPONENTIAL DECAY MODEL VERSUS AVERAGE VELOCITY AT CONTRACTION

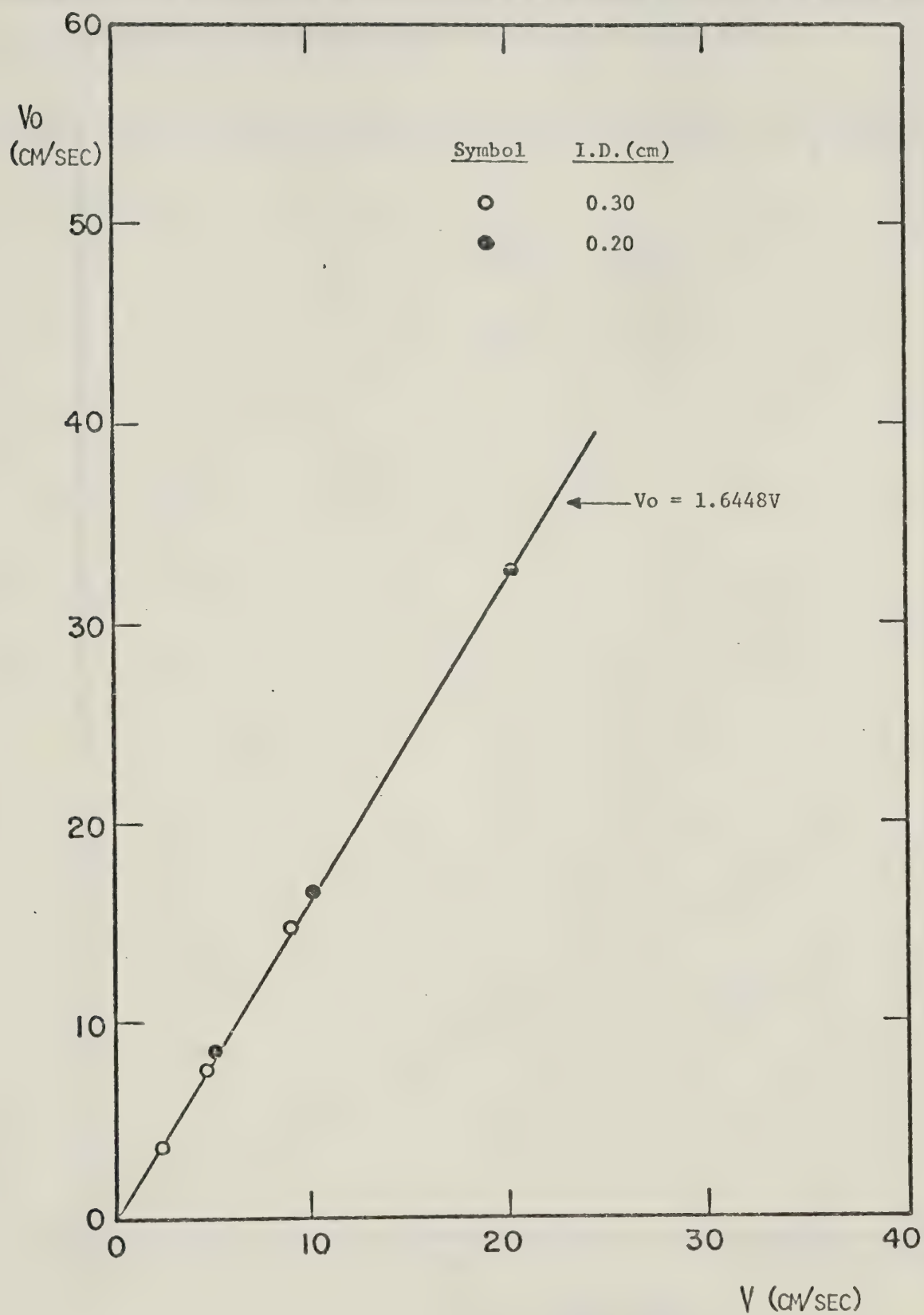
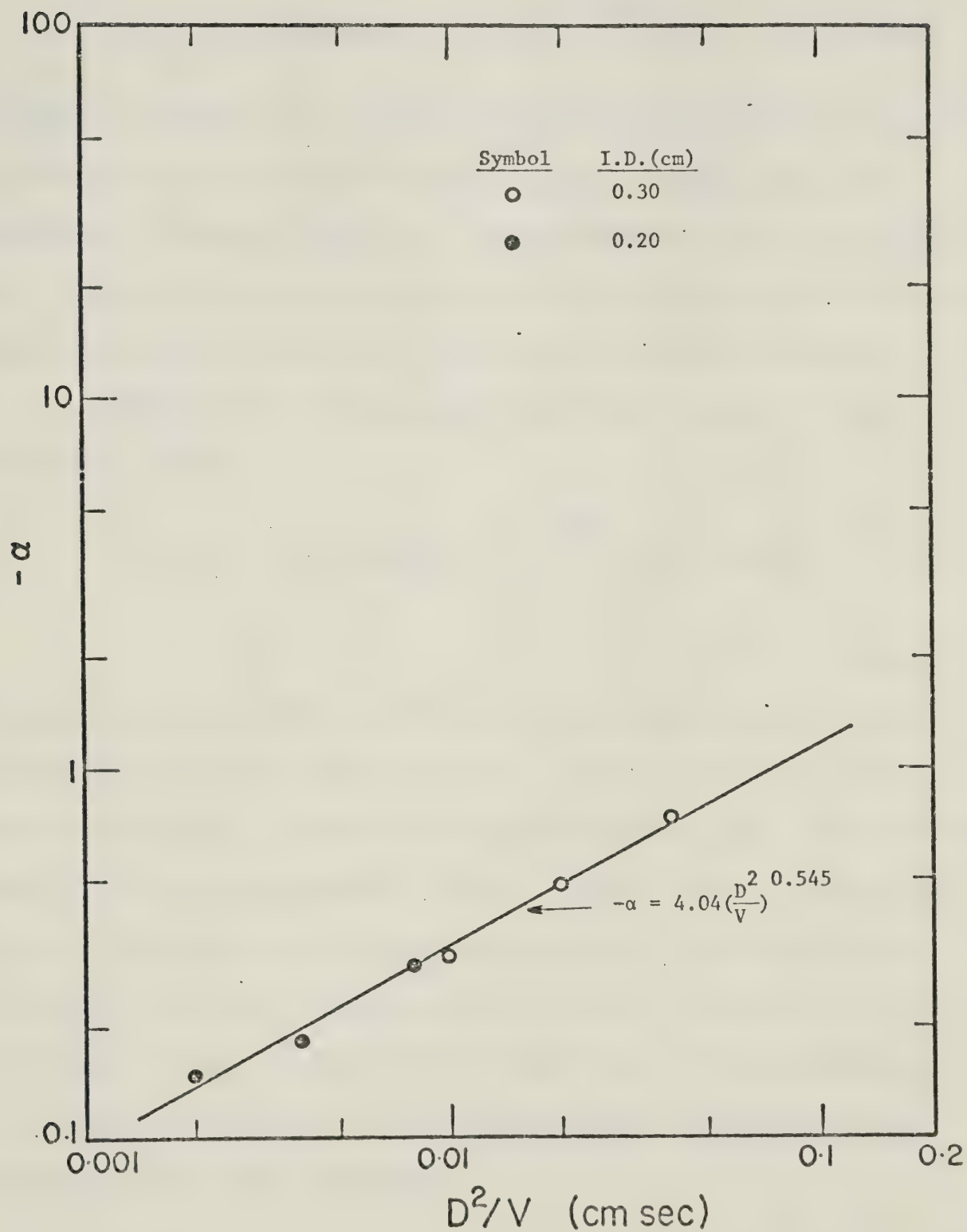


FIGURE IV-22 PARAMETER α OF THE EXPONENTIAL DECAY MODEL

The mean deviation of the value of α calculated from Equation (IV-21) from the values of α in Table (IV-5) was less than 5%.

Substituting Equations (IV-23) and (IV-24) into Equation (IV-22), and empirical equation in the form:

$$V_{z,\zeta} = 1.645V \exp \left[-4.04 \left(\frac{D^2}{V} \right)^{0.545} \left(\frac{z}{D} \right) \right] \quad (\text{IV-25})$$

was found to represent the relationships for the centerline velocity with flow rate and capillary tube diameter. Figure (IV-23) shows the comparisons of Equation (IV-25) and the experimental data for two typical runs. The predicted values of Equation (IV-25) have a maximum deviation of about 5% and a mean deviation less than 3% from the experimental data.

Differentiation of Equation (IV-25) with respect to axial location (z) yields:

$$V_{z,z,\zeta} = - 6.646 \left(\frac{V}{D} \right) \left(\frac{D^2}{V} \right)^{0.545} \exp \left[-4.04 \left(\frac{D^2}{V} \right)^{0.545} \left(\frac{z}{D} \right) \right] \quad (\text{IV-26})$$

The comparisons of Equation (IV-26) and the experimental data are shown in Figure (IV-24) for two typical runs. The predicted values from Equation (IV-26) have a maximum deviation of about 9% and a mean deviation of about 3% from the experimental values. Also it is of interest that Equation (IV-26) predicts a maximum value for the stretch rate of the contraction. Since the stretch rate of the fully developed tube flow must be equal to zero, therefore the stretch rate must decrease and go to zero somewhere between the contraction and the location where the velocity profile is fully developed.

FIGURE IV-23

COMPARISON OF CENTERLINE AXIAL VELOCITY WITH EXPONENTIAL DECAY MODEL

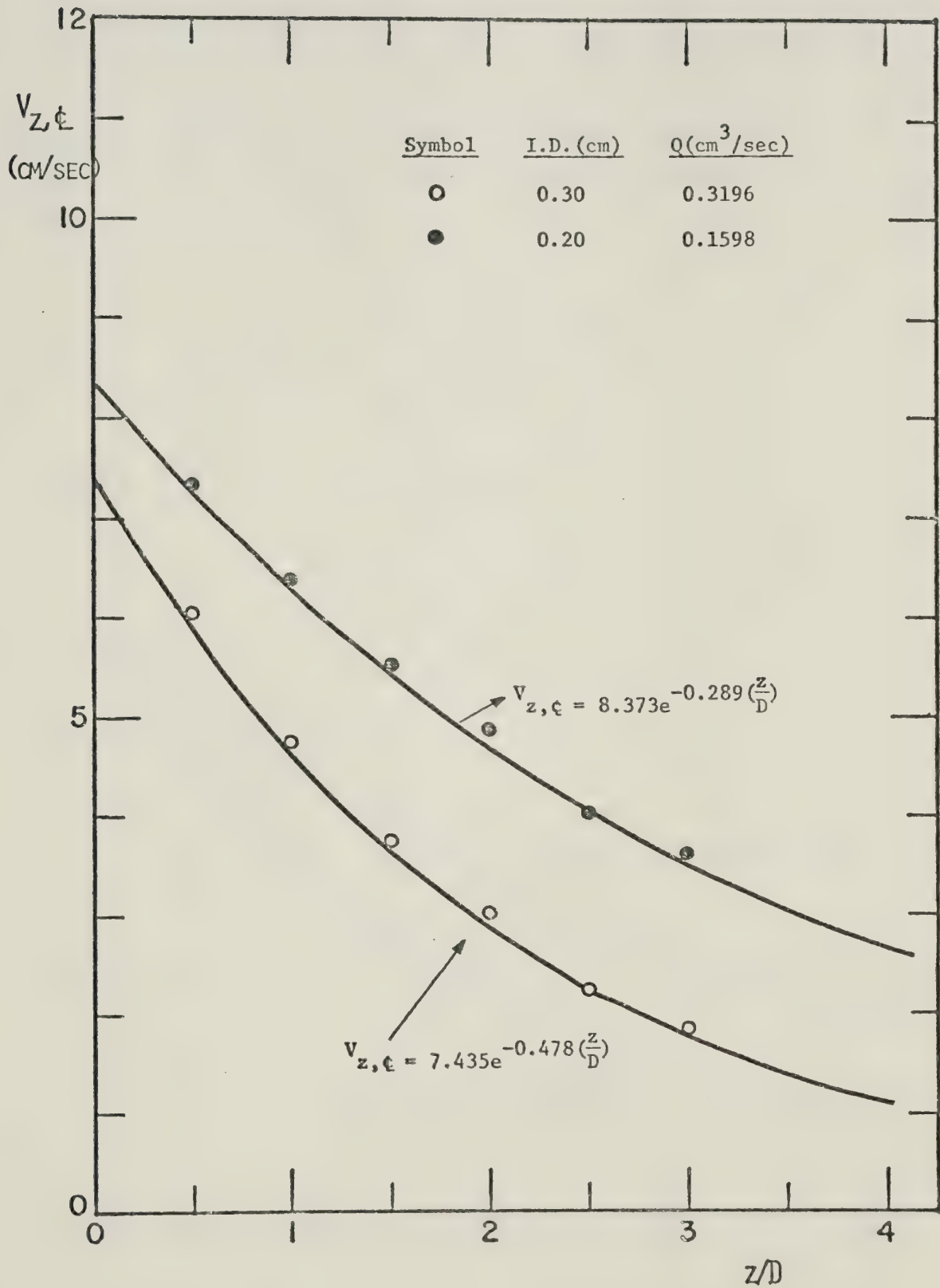
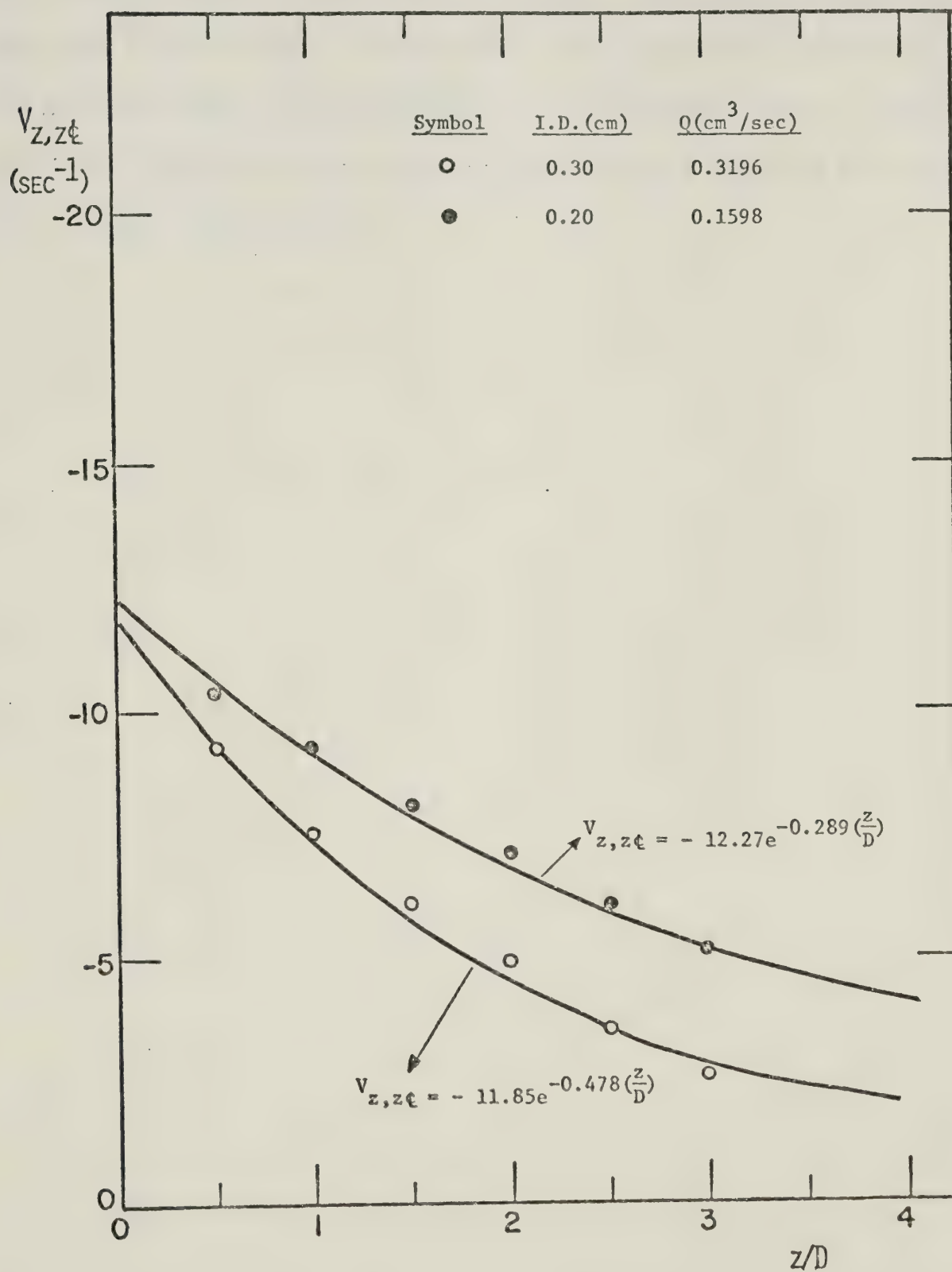


FIGURE IV-24

COMPARISON OF CENTERLINE STRETCH RATE WITH EXPONENTIAL DECAY MODEL



The above experimental results reveal that the velocity field within the central core can not be predicted simply by sink flow model or K-1 model. However, the exponential decay model has good agreement with the experimental centerline velocities. Besides, the experiment data show that the ratio of the square of the capillary tube diameter to the average velocity at the contraction (D^2/V) can be used to reasonably represent the relationships between the velocity field, and the capillary tube diameter and flow rate.

CHAPTER V

CONCLUSIONS AND RECOMMENDATIONS

V.1 Conclusions

The conclusions of this study can be summarized in the following manner:

- (i) The experimental velocity profiles for 0.2% aqueous solution of Separan AP-30 within the central core showed considerable development upstream of the entrance. At the entrance, centerline velocities were approximately 96% of the centerline velocities of the fully developed tube flow and the wall shear stresses were approximately 85% of the wall shear stresses of the fully developed tube flow.
- (ii) The sink flow model and the K-1 model failed to predict the centerline velocities within the central core because the sink flow model had poor agreement of the experiment data at large upstream locations from the contraction. Parameters in a quadratic equation suggested by K-1 model did not have obvious relationships with the flow rate and the capillary tube diameter.
- (iii) The initial cone semi-angle could be expressed as:

$$\phi_o = 64.05 \left(\frac{D}{V} \right)^{2.0.6} \quad (V-1)$$

where ϕ_o is in degrees, for values of $\left(\frac{D}{V} \right)^2$ between 0.0020 and 0.0398 cm sec. The initial cone semi-angles predicted by Equation (V-1) had a mean deviation of about 3% from the measured values.

- (iv) The centerline axial velocities within the central core could be expressed as:

$$V_{z,c} = 1.646 V \exp \left[-4.04 \left(\frac{D}{V} \right)^{0.545} \left(\frac{z}{D} \right) \right] \quad (V-2)$$

within the range of operating variables in this study. The centerline axial velocities predicted by Equation (V-2) had a maximum deviation of about 5% and a mean deviation less than 3% from the experimental data.

- (v) The stretch rates along the centerline obtained by differentiating Equation (V-2) with respect to axial location (z) are given by:

$$V_{z,z,c} = - 6.646 \left(\frac{V}{D} \right) \left(\frac{D}{V} \right)^{0.545} \exp \left[-4.04 \left(\frac{D}{V} \right)^{0.545} \left(\frac{z}{D} \right) \right] \quad (V-3)$$

The stretch rates predicted by Equation (V-3) had a maximum deviation of about 9% and a mean deviation of about 3% from the experimental values.

V.2 Recommendations

- (i) Data in this study are based on only two capillary tube diameters, therefore additional data should be generated to test the validity of the diameter dependence implied by the correlations.
- (ii) In this study the empirical equation developed, predicts the stretch rate is a maximum at the contraction. On the otherhand, the stretch rate at a downstream location in the capillary tube where the velocity profile is fully developed must be equal to zero. This means the stretch rate must

decrease and go to zero somewhere between the contraction and location where the velocity profile is fully developed. More detailed study within this region is recommended.

- (iii) Since all of the empirical relationships in this study are restricted as to the range of operating variables, some experiments with other polymer solutions are recommended in order to compare with the predictions such as Equations (V-1) and (V-2) in this study.

NOMENCLATURE

$a_2, a_4, a_6,$	parameters defined by Equation (II-16)
c	parameters defined by Equation (II-15)
C_1, C_2	parameters defined by Equation (II-6)
C_1', C_2'	parameters defined by Equation (II-4)
d	diameter of the fluid column within the center core, cm
D	I.D. of capillary tube, cm
D_p	diameter of the plate, cm
k_T	torsion bar constant, dyne cm/micron
K	parameter defined by Equation (IV-13)
K'	parameter defined by Equation (IV-12)
K_1, K_2, K_3	K-1 parameters, Equation (II-13), cm/sec
M	magnification of the streaks on the graph paper
n	flow behavior index in power-law
N	number of slits and spokes on the chopping disc
p	parameter defined by Equation (II-4)
Q	volumetric flow rate, cm^3/sec
Q^*	volumetric flow rate function defined by Equation (II-3)
r	radial coordinate in cylindrical coordinate system, cm
r^*	radial coordinate in spherical coordinate system, cm
R	radius of capillary tube, cm
R_p	radius of the plate, cm
s	parameter defined by Equation (IV-13)
s'	parameter defined by Equation (IV-12)
S_1	sensitivity of the torque transducer, micron /volt

t	parameter defined by Equation (IV-13)
t'	parameter defined by Equation (IV-12)
\bar{t}	time interval for streak, sec
T	torgue, dyne cm
V	average velocity at the contraction, cm/sec
V_0	velocity at contraction defined by Equation (II-16), cm/sec
V_r	radial velocity in cylindrical coordinate system, cm/sec
V_r^*, V_θ, V_ϕ	velocity components in spherical coordinate system, cm/sec
V_z	axial velocity in cylindrical coordinate system, cm/sec
$V_{z,c}$	axial centerline velocity, cm/sec
$V_{z,c,0}$	axial centerline velocity at the contraction, cm/sec
$V_{z,z}$	axial stretch rate, sec^{-1}
$V_{z,z,c}$	axial stretch rate along centerline, sec^{-1}
z	axial distance upstream of contraction, cm

Greek Symbols

α	parameter defined by Equation (II-18)
α'	parameter defined by Equation (II-16)
β	parameter defined by Equation (II-15)
Δ_T	movement of torsion head transducer, volt
θ_{fl}	relaxation time, sec
θ_0	zero shear relaxation time, sec
μ	viscosity, poise
μ_0	parameter defined by Equation (II-15), poise
ν	kinematic viscosity, cm^2/sec
σ	shear rate, sec^{-1}

τ	shear stress, dyne/cm ²
τ_w	wall shear stress, dyne/cm ²
ϕ	cone semi-angle, degrees
ϕ_0	initial cone semi-angle, degrees
ψ	angle of viscometer cone, degrees
ω	number of revolutions of the chopping disc/minute, RPM
Ω	angular rotation of the plate, rad./sec

BIBLIOGRAPHY

1. ASTARITA, G., "Dimensional Analysis of Flow of Viscoelastic Fluids", Chem. Eng. Sci., 29, 1273 (1974).
2. BAGLEY, E. B., and SCHREIBER, H. P., "Effect of Die Entry Geometry on Polymer Melt Fracture and Extrudate Distortion". Trans. Soc. Rheol., 5, 341 (1961).
3. BAGLEY, E. B., "The Separation of Elastic and Viscous Effects in Polymer Flow". Trans. Soc. Rheol., 5, 355 (1961).
4. BALAKRISHNAN, C., and GORDON, R. J., "Extensional Viscosity and Recoil in Highly Dilute Polymer Solutions"., A.I.Ch.E.J., 21, 1225 (1975).
5. BALLENGER, T. F., et. al., "Polymer Melt Flow Instabilities in Extrusion: Investigation of the Mechanism and Material and Geometric Variables"., Trans. Soc. Rheol., 15, 195 (1971).
6. BALLENGER, T. F., and WHITE, J. L., "The Development of the Velocity Field in Polymer Melts in a Reservoir Approaching a Capillary Die"., J. Appl. Poly. Sci., 15, 1949 (1971).
7. BALMER, R. T., "A Surface Tension Driven Extensional Flow"., Trans. Soc. Rheol., 19, 407 (1975).
8. BARNETT, S. M., "A correlation of Melt Fracture"., Poly. Eng. and Sci., 7, 168 (1967).
9. BLYLER, Jr., L. L., and HART, Jr., A. C., "Capillary Flow Instability of Ethylene Polymer Melts"., Poly. Eng. and Sci., 10, 193 (1970).
10. CATANIA, P. J., Ph.D. Dissertation, in preparation, University of Alberta (1976).
11. CHRISTIANSEN, E. B., KELSEY, S. J., and CARTER, T. R., "Laminar Tube Flow through an Abrupt Contraction"., A.I.Ch.E.J., 18, 372 (1972).
12. CHRISTIANSEN, E. B., and KELSEY, S. J., "Nonisothermal Laminar Contracted Flow"., A.I.Ch.E.J., 18, 713 (1972).
13. COGSWELL, F. N., "Converging Flow of Polymer Melts in Extrusion Dies"., Poly. Eng. and Sci., 12, 64 (1972).
14. COGSWELL, F. N., "Measuring the Extensional Rheology of Polymer Melts"., Trans. Soc. Rheol., 16, 383 (1972).
15. den OTTER, J. L., "Some Investigations of Melt Fracture". Rheol. Acta., 10, 200 (1971).

16. den OTTER, J. L., WALES, J. L. S., and SCHIJF, J., "The Velocity Profiles of Molten Polymers during Laminar Flow"., *Rheol. Acta.*, 6, 205 (1967).
17. DENSON, C. D., "Implications of Extensional Flow in Polymer Fabrication Processes"., *Poly. Eng. and Sci.*, 13, 125 (1973).
18. GIESEKUS, H., *Rheol. Acta*, 7, 127 (1968).
19. GIESEKUS, H., *Rheol. Acta*, 8, 411 (1969).
20. HALMOS, A. L., and Boger, D. V., "Flow of Viscoelastic Polymer Solutions through an Abrupt 2- to - 1 Expansion"., *Trans. Soc. Rheol.*, 20, 253 (1976).
21. HAN, C. D., "Wall Normal Stresses and Die Swell Behavior of Viscoelastic Polymeric Melts in Flow through Converging Ducts"., *A.I.Ch.E.J.*, 19, 649 (1973).
22. HAN, C. D., "Influence of the Die Entry Angle on the Entrance Pressure Drop, Recoverable Elastic Energy, and Onset of Flow Instability in Polymer Melt Flow"., *J. Appl. Phys. Sci.*, 17, 1403 (1973).
23. HURLIMANN, H. P., and KNAPPE, W., "The Relationship between the Normal Stress of a Plastic (Polymer) Melt in a Jet Inlet in a Melt Fracture"., *Rheol. Acta.*, 11, 292 (1972).
24. KALONI, P. N., "On Creeping Flow of a Visco-Elastic Liquid in Converging Channel"., *J.Phys. Soc. Japan*, 20, 132 (1965).
25. KALONI, P. N., "On the Flow of an Elastico-Viscous Fluid in a Conical Duct"., *J.Phys. Soc. Japan*, 20, 610 (1965).
26. KANEL, F. A., "The Extension of Viscoelastic Materials"., Ph.D. Dissertation, University of Delaware (1972).
27. KASE, S., "Studies on Melt Spinning. III. Velocity Field within the Thread"., *J. Appl. Phys. Sci.*, 18, 3267 (1974).
28. KASE, S., "Studies on Melt Spinning. IV. On the Stability of Melt Spinning"., *J. Appl. Phys. Sci.*, 18, 3279 (1974).
29. KIZIOR, T. E., and SEYER, F. A., "Axial Stress in Elongational Flow of Fiber Suspension"., *Trans. Soc. Rheol.*, 18, 271 (1974).
30. McINTIRE, L.V., "On the Initiation of Melt Fracture"., *J. Appl. Poly. Sci.*, 16, 2901 (1972).

31. METZNER, A. B., and METZNER, A. P., "Stress Levels in Rapid Extensional Flows of Polymeric Fluids"., *Rheol. Acta*, 9, 174 (1970).
32. METZNER, A. B., UEHLER, E. A., and CHAN MAN FONG, C. F., "Converging Flows of Viscoelastic Materials"., *A.I.Ch.E.J.*, 15, 750 (1969).
33. MURCH, R. E., "The Converging Flow of Viscoelastic Fluids"., Ph. D. Dissertation, University of Delaware (1970).
34. NICKELL, R. E., TANNER, R. I., and CASWELL, B., "The Solution of Viscous Incompressible Jet and Free-Surface Flows Using Finite-Element Methods"., *J.Fluid Mech.*, 65, 189 (1974).
35. OKA, S., "The Steady Slow Motion of a Viscous Fluid through a Tapered Tube"., *J.Phys. Soc. Japan*, 19, 1481 (1964).
36. OLIVER, D. R., "The Prediction of Angle of Convergence for the Flow of Viscoelastic Liquids into Orifices"., *Chem. Eng. J.*, 6, 265 (1973).
37. OLIVER, D. R., and BRAGG, R., "The Extensional Flow of Polymeric Solutions through Small Orifices"., *Chem. Eng. J.*, 5, 1 (1973).
38. OLIVER, D. R., and BRAGG, R., "Flow Patterns in Viscoelastic Liquids Upstream of Orifices"., *C.J.Ch.E.*, 51, 287 (1973).
39. OLIVER, D. R., and BRAGG, R., "The Triple Jet: a New Method for Extensional Viscosity Measurement"., *Nat. Phys. Sci.*, 241, 131 (1973).
40. PEARSON, J. R. A., and PICKUP, T. J. F., "Stability of Wedge and Channel Flow of highly Viscous and Elastic Liquids"., *Polymer*, 14, 209 (1973).
41. PETRIE, C. J. S., and DENN, MM., "Instabilities in Polymer Processing"., *A.I.Ch.E.J.*, 22, 209 (1976).
42. PHILIPPOFF, W., "The Analysis of the Entrance Flow into a Slit Part I"., *Trans. Soc. Rheol.*, 20, 423 (1976).
43. RAMA MURTHY, A. V., "Flow Instabilities in a Capillary Rheometer for an Elastic Polymer Solution"., *Trans. Soc. Rheol.*, 18, 431 (1974).
44. ROTHENBERGER, R., McCOY, D. H., and DENN, M. M., "Flow Instability in Polymer Melt Extrusion"., *Trans. Soc. Rheol.*, 17, 259 (1973).
45. SOUTHERN, J. H., and PAUL, D. R., "Elastic Fracture of Polystyrene Solutions"., *Poly. Eng. and Sci.*, 14, 560 (1974).

46. TOMITA, Y., and SHIMBO, T., "Unstable Flow of Viscoelastic Fluids"., J. Appl. Poly. Sci., 20, 137 (1973).
47. TORDELLA, J. P., "Capillary Flow of Molten Polyethylene - A Photographic Study of Melt Fracture"., Trans. Soc. Rheol., 1, 203 (1957).
48. TORDELLA, J. P., "Unstable Flow of Molten Polymers: A Second Site of Melt Fracture"., J. Appl. Poly. Sci., 7, 215 (1963).
49. UEBLER, E. A., Ph. D. Dissertation, University of Delaware (1966).
50. VINOGRADOV, G. V., and MANIN, V. N., "An Experimental Study of Elastic Turbulence"., Koll Z., 201, 93 (1965).
51. VLACHOPOULOS, J., and LIDORIKIS, S., "Melt Fracture of Polystyrene"., Poly. Eng. and Sci., 11, 1 (1971).
52. VOSSOUGH, S., Ph.D. Dissertation, University of Alberta, (1976).
53. VRENTAS, J. S., and DUDA, J. L., "Flow of a Newtonian Fluid through a Sudden Contraction"., Appl. Sci. Res., 28, 241 (1973).
54. WEINBERGER, C. B., Ph.D. Dissertation, University of Michigan, (1970).
55. WEISSENBERG Rheogoniometer, The., Instruction Manual, Model R.18., Sagamo Controls Limited, Section D. Theory.
56. WHITE, J. L., "Critique on Flow Patterns in Polymer Fluids at the Entrance of a Die and Instabilities Leading to Extrudate Distortion"., J. Appl. Poly. Sci., 20, 155 (1973).

APPENDIX A

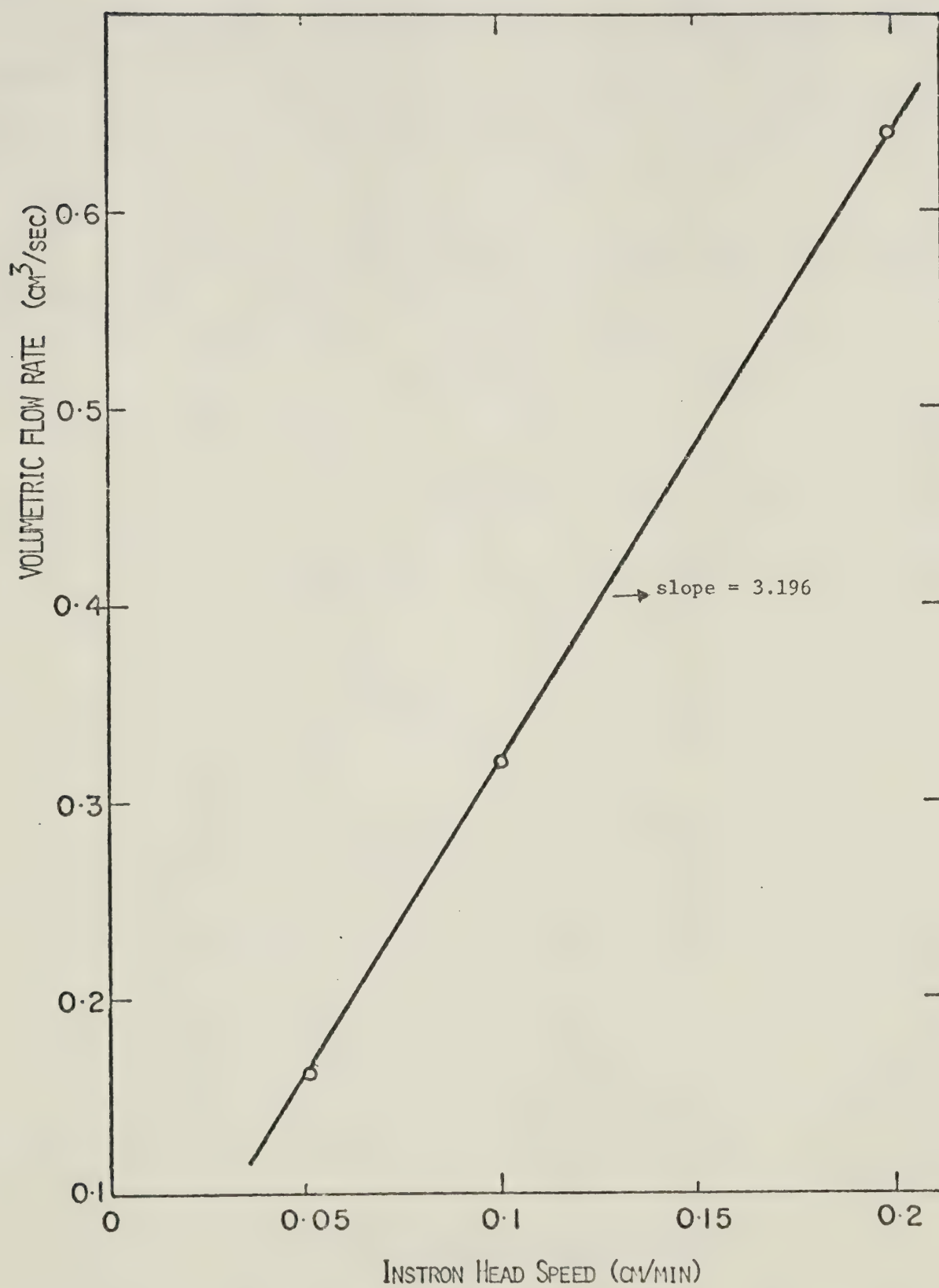
CALIBRATION OF INSTRON

An Instron (Model TT-BM) and stainless steel hydraulic cylinder of approximately 15.60 cm I.D. were used to provide a constant flow rate of the polymer solution in this study. At Push-button Speed Selector settings of 0.2, 0.1 and 0.05 cm/min, the measured flow rates which were determined by the volume of the polymer solution collected over a known period of time were 0.6397, 0.3202 and 0.1603 cm³/sec respectively. Figure (A-1) shows a plot of the measured volumetric flow rate and the Instron head speed or speed of piston. The solid line which is an eyefit through the data results in a calibration factor for flow rate of 3.196 (cm³/sec)/(cm/min). The comparison of the calibrated flow rate and the flow rate calculated from knowledge of the Instron head speed and I.D. of the cylinder is tabulated in Table A-1.

TABLE A-1
CALIBRATION OF FLOW RATE

Instron Head Speed (cm/min)	Calibration Flow Rate (cm ³ /sec)	Calculated Flow Rate (cm ³ /sec)
0.05	0.1598	0.1592
0.1	0.3196	0.3186
0.2	0.6392	0.6371

FIGURE A-1 CALIBRATION OF INSTRON HEADSPEED



From Table (A-1), the flow rates calculated from knowledge of the Instron speed and calibrated flow rates were within 0.5% of each other.

APPENDIX B

RHEOLOGICAL PROPERTIES OF THE POLYMER SOLUTION

A WEISSENBERG Rheogoniometer was used to measure viscosity of the polymer solution. This Rheogoniometer was calibrated with two standard oils of different viscosity. The theory of this Rheogoniometer which was shown in the Instruction Manual of the Weissenberg Rheogoniometer (55) is also discussed here.

The Weissenberg Rheogoniometer is basically a simple cone and plate viscometer. The shear stress is given by:

$$\tau = \frac{3T}{2\pi R_p^3}$$

(B-1)

$$\tau = \frac{3.82T}{D_p^3}$$

where τ = shear stress, dynes/cm²

$T = S_1 \Delta_T k_T$ = torque , dynes cm

S_1 = torque transducer sensitivity, micron/volt

Δ_T = movement of torsion head transducer, volts

k_T = torsion bar constant, dyne cm/micron movement of the transducer

R_p = radius of the plate, cm

D_p = diameter of the plate, cm

The shear rate is given by,

$$\sigma = \frac{\text{angular velocity in radians/sec}}{\tan \psi}$$

i.e. for the small angles of ψ used:

$$\begin{aligned}\sigma &= \frac{180}{\pi} \frac{\Omega}{\psi} \\ &= \frac{360}{\psi t}\end{aligned}\tag{B-2}$$

where σ = shear rate, sec^{-1}

ψ = angle of cone, degrees

t = $2\pi/\Omega$, sec./rev.

Ω = angular rotation of the plate, rad./sec.

With τ and σ measured apparent viscosity is calculated by:

$$\mu = \frac{\tau}{\sigma}\tag{B-3}$$

For all runs in this study only one plate and one torsion bar was used. For this plate and torsion bar, the Rheogoniometer parameters are:

$$\begin{aligned}D_p &= 7.50 \text{ cm} \\ \psi &= 55'10'' \\ k_T &= 0.1066 \times 10^3 \text{ dyne cm/micron} \\ S_1 &= 1.008 \text{ micron/volt} \\ \text{Gap Set} &= 39 \text{ microns}\end{aligned}$$

Therefore, Equations (B-1) and (B-2) become,

$$\tau = 0.973 \Delta_T \text{ dyne/cm}^2\tag{B-4}$$

$$\sigma = \frac{391.56}{t} \text{ sec}^{-1}\tag{B-5}$$

By setting a rotational speed of the motor which drove the plate, the movement of torsion head transducer (Δ_T) was recorded by a recorder. Using this knowledge, t and Δ_T can be found. Then the values of shear stress and shear rate can be calculated by substituting t and Δ_T into Equations (B-4) and (B-5).

Plots of shear stress and, viscosity versus shear rate are given in Figures (B-1) and (B-2). In Figure (B-1), good agreements of the data with the calibrated solid lines of shear stress versus shear rate with slope unity and the calibrated constant viscosity horizontal dashed lines obtained for the standard oils, indicate the Newtonian behavior of these fluids. In Figure (B-2) the solid line of shear stress versus shear rate can be represented by Equation (B-6) within the range of shear rate from 5.0×10^0 to $1.10 \times 10^3 \text{ sec}^{-1}$ which is of interest in this study.

$$\tau = 2.24 \sigma^{0.55} \quad (\text{B-6})$$

The dashed line of apparent viscosity versus shear rate can be represented by Equation (B-7)

$$\mu = 2.24 \sigma^{-0.45} \quad (\text{B-7})$$

Equations (B-6) and (B-7) indicate power law behavior of the polymer solution with flow behavior index ($n = 0.55$) in the range of shear rates studied.

FIGURE B-1 RHEOLOGICAL PROPERTIES OF STANDARD OILS

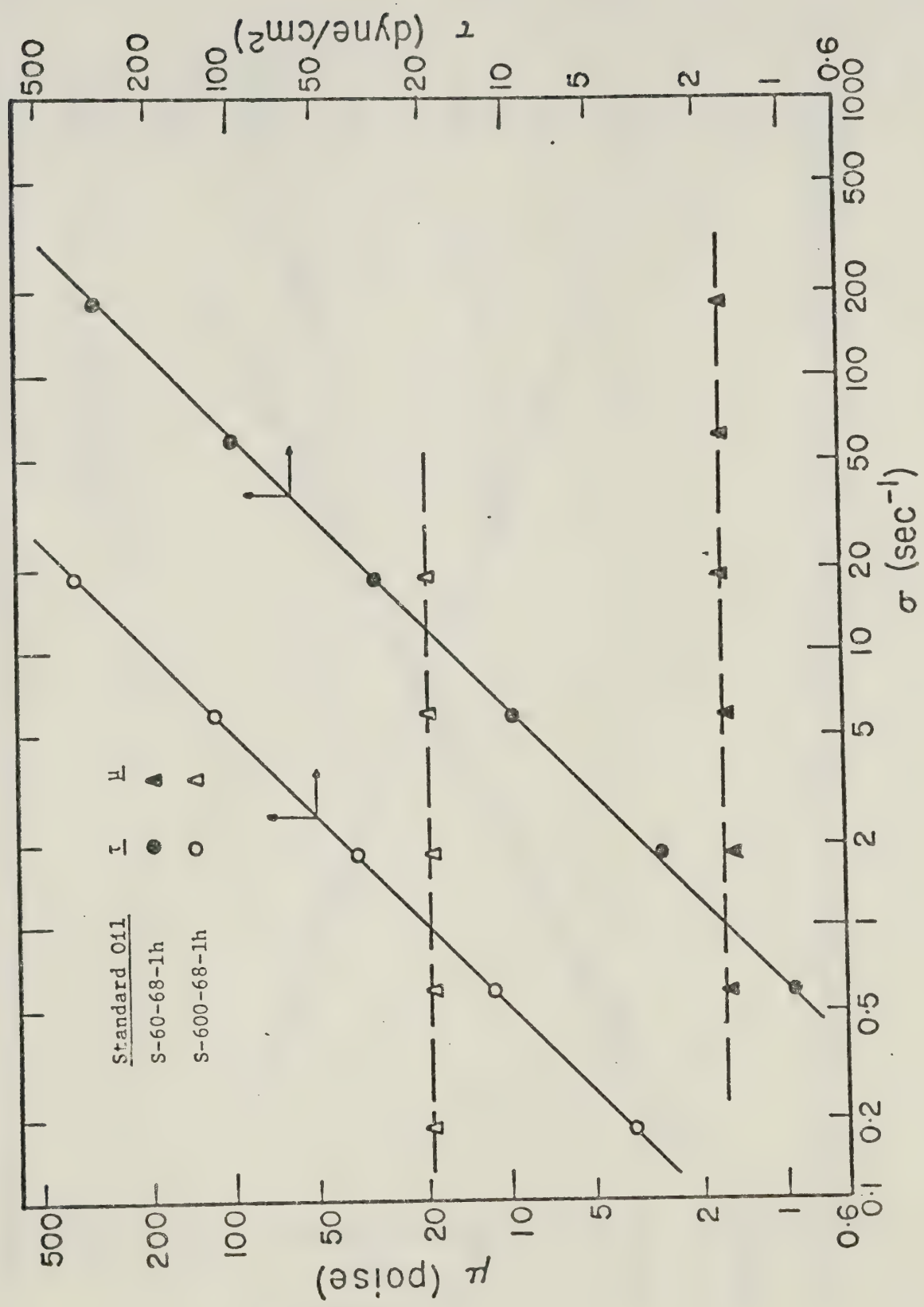


FIGURE B-2 RHEOLOGICAL PROPERTIES OF SEPARAN AP-30 0.2% (BY WEIGHT)

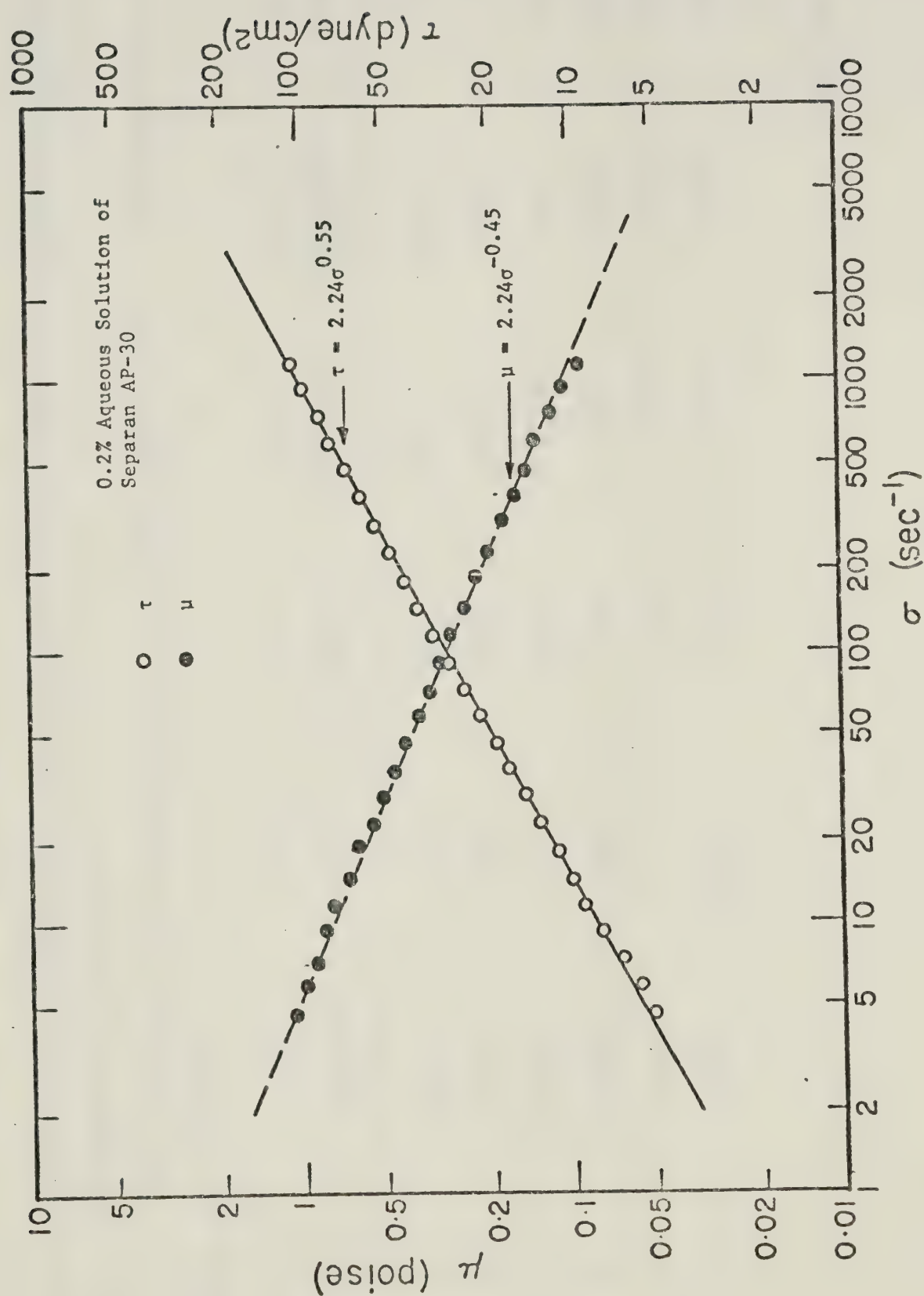


TABLE B-1

RHEOLOGICAL PROPERTIES OF STANDARD OILS

(i) Standard Oil (S-60-68-1h)		This standard oil had a stated viscosity of 1.634 poise at 20°C. The temperature of this experiment was 20 ± 1°C				
Run No.	$\frac{\Omega}{2\pi}$ (rev/sec)	t (sec/rev)	σ (sec ⁻¹)	ΔT (volts)	τ (dyne/cm ²)	μ (poise)
1	0.47	2.11	186	315	306.5	1.651
2	0.15	6.67	58.9	100	97.3	1.653
3	0.047	21.1	18.6	31.25	30.4	1.638
4	0.015	66.7	5.89	9.75	9.49	1.611
5	0.0047	211	1.86	2.875	2.80	1.507
6	0.0015	667	0.589	0.950	0.924	1.570

Continued.....

TABLE B-1 (continued)

(ii) Standard Oil (S-600-68-1h)		This standard oil had a stated viscosity of 19.74 poise at 20°C. The temperature of this experiment was $20 \pm 1^\circ\text{C}$.				
Run No.	$\frac{\Omega}{2\pi}$ (rev/sec)	t (sec/rev)	σ (sec ⁻¹)	ΔT (volts)	τ (dyne/cm ²)	μ (poise)
1	0.047	21.1	18.6	375	364.9	19.66
2	0.015	66.7	5.89	117.5	114.3	19.42
3	0.0047	211	1.86	36.25	35.27	19.00
4	0.0015	667	0.589	11.50	11.2	19.00
5	0.00047	2110	0.186	3.70	3.6	19.40

TABLE B-2
RHEOLOGICAL PROPERTIES OF POLYMER SOLUTION

0.2% Separan AP-30 solution (by weight) at 20°C						
Run	$\frac{\Omega}{2\pi}$ (rev./sec.)	t (sec./rev.)	σ (sec ⁻¹)	ΔT (volts)	τ (dyne/cm ²)	μ (poise)
No.						
1	3.0	0.334	1170	110	107.0	0.091
2	2.4	0.420	932	100	97.3	0.104
3	1.9	0.530	739	87.5	85.1	0.115
4	1.5	0.667	589	80	77.8	0.132
5	1.2	0.840	466	68.75	66.9	0.144
6	0.95	1.06	371	61	59.4	0.160
7	0.75	1.33	286	54	52.5	0.178
8	0.60	1.67	235	47.5	46.2	0.197
9	0.47	2.11	186	42	40.9	0.220
10	0.38	2.65	148	37.5	36.5	0.247
11	0.30	3.34	117	33	32.1	0.274
12	0.24	4.20	93.2	29.5	28.7	0.308

Continued.....

TABLE B-2 (continued)

Run No.	$\frac{\Omega}{2\pi}$ (rev./sec.)	t (sec/rev.)	σ (sec ⁻¹)	ΔT (volts)	τ (dyne/cm ²)	μ (poise)
13	0.19	5.30	73.9	25.5	24.8	0.336
14	0.15	6.67	58.9	22	21.4	0.364
15	0.12	8.40	46.6	19.5	19.0	0.407
16	0.095	10.6	37.1	17.5	17.0	0.459
17	0.075	13.3	59.6	15.25	14.8	0.502
18	0.060	16.7	23.5	13.25	12.9	0.550
19	0.047	21.1	18.6	11.75	11.4	0.616
20	0.038	26.5	14.8	10.25	9.97	0.675
21	0.030	33.4	11.7	9.25	9.00	0.767
22	0.024	42.0	9.32	8	7.78	0.835
23	0.019	53.0	7.39	6.75	6.57	0.889
24	0.015	66.7	5.89	5.875	5.72	0.971
25	0.012	84.0	4.66	5.2	5.06	1.086

APPENDIX C

AXIAL VELOCITY PROFILES AND CENTERLINE VELOCITIES

C.1. Axial Velocity Profiles

Contained in this section are the axial velocity profiles at several upstream axial locations for various flow rates. The method used to measure the axial velocities and associated error were discussed in Chapter III. In addition, included in the table are the axial velocity profiles at the contraction ($z/D = 0$). These were determined by drawing eye-fit lines through the arithmetic plots of measured axial velocities as a function of distance from the entrance and extrapolating the curves to the entrance.

Although the measured velocity was not precisely the axial velocity (discussed in Chapter III), the small cone angles resulted in only small difference between measured and true axial velocity. Therefore, these measured velocities are tabulated as the axial velocities in Table (C-1) to (C-6). The radial location in Table (C-1) to (C-6) are the actual distance from the centerline of the capillary tube as distinguished from apparent distances on graph paper. The radial locations marked with an "*" means that these radial locations are on the opposite side of the centerline of those which don't have the asterisk.

TABLE C.1

Diameter: 0.20 cm I.D.

Flow Rate: 0.1598 cm³/sec

Axial Location (z/D) (No. of Dia.)	Radial Location (r) (cm)	Axial Velocity (V _z) (cm/sec)
0.0	0.000	8.25
	0.013	8.18
	0.033	7.70
	0.028	7.40
	0.034	7.12
	0.034*	7.01
	0.045	6.62
	0.054*	5.90
	0.066	5.50
	0.058	5.05
	0.080	3.78
	0.095	2.61
1.0	0.100*	2.54
	0.000	6.38
	0.015	6.09
	0.000	6.02
	0.008	6.00
	0.007	5.83
	0.012*	5.81

Continued.....

TABLE C-1 (continued)

Axial Location (z/D) (No. of Dia.)	Radial Location (r) (cm)	Axial Velocity (V _z) (cm/sec)
1.0	0.028	5.78
	0.039	5.64
	0.037	5.62
	0.029	5.52
	0.040*	5.50
	0.036	5.26
	0.050	5.25
	0.030*	5.24
	0.063*	4.65
	0.050	4.64
	0.056*	4.60
	0.066*	4.48
	0.066	4.38
	0.072	4.32
	0.062	4.14
	0.092*	3.64
	0.090	3.08
	0.105	2.08
	0.110*	2.07
2.0	0.000	4.82
	0.011	4.78
	0.000	4.75

Continued.....

TABLE C-1 (continued)

Axial Location (z/D) (No. of Dia.)	Radial Location (r) (cm)	Axial Velocity (V _z) (cm/sec)
2.0	0.008	4.68
	0.015*	4.60
	0.018	4.52
	0.032	4.41
	0.033	4.36
	0.044	4.35
	0.044	4.29
	0.038*	4.20
	0.039	4.15
	0.045*	4.15
	0.057	4.02
	0.055	3.70
	0.066*	3.67
	0.074*	3.56
	0.075	3.43
	0.069*	3.42
	0.072	3.32
	0.086	3.21
	0.101*	2.92
	0.099	2.49
	0.124*	1.90

Continued.....

TABLE C-1 (continued)

Axial Location (z/D) (No. of Dia.)	Radial Location (r) (cm)	Axial Velocity (V _z) (cm/sec)
3.0	0.000	3.65
	0.019*	3.56
	0.012	3.50
	0.016	3.50
	0.022	3.50
	0.036	3.45
	0.000	3.40
	0.050	3.35
	0.044*	3.27
	0.040	3.25
	0.053*	3.15
	0.051	3.12
	0.042	3.10
	0.064	3.01
	0.062	2.89
	0.072*	2.76
	0.087*	2.63
	0.082	2.60
	0.087	2.57
	0.082*	2.42
	0.114*	2.28
	0.098	2.27
	0.117	1.91
	0.138*	1.60

TABLE C-2

Diameter: 0.20 cm I.D.

Flow Rate: 0.3196 cm³/sec

Axial Location (z/D) (No. of Dia.)	Radial Location (r) (cm)	Axial Velocity (V _z) (cm/sec)
0.0	0.003	16.20
	0.009*	15.60
	0.012*	15.55
	0.021*	15.40
	0.013	15.30
	0.014*	15.00
	0.028*	14.80
	0.024*	14.65
	0.046*	14.20
	0.032*	14.15
	0.032	13.80
	0.029*	13.80
	0.037*	13.75
	0.043	13.50
	0.031	13.50
	0.050*	13.20
	0.036*	13.20
	0.048*	13.10
	0.051*	13.00
	0.051*	12.25
	0.056	12.00

Continued.....

TABLE C-2 (continued)

Axial Location (z/D) (No. of Dia.)	Radial Location (r) (cm)	Axial Velocity (V _z) (cm/sec)
0.0	0.066	11.00
	0.073*	9.60
	0.077	9.40
	0.088	7.00
	0.100	3.65
1.0	0.006	13.80
	0.014*	13.30
	0.010*	13.20
	0.023*	12.96
	0.019	12.96
	0.015	12.80
	0.016*	12.75
	0.030*	12.40
	0.028*	12.30
	0.038*	11.90
	0.047*	11.88
	0.038	11.80
	0.032*	11.70
	0.028	11.60
	0.043*	11.60
	0.031	11.43
	0.041*	11.20

Continued.....

TABLE C-2 (continued)

Axial Location (z/D) (No. of Dia.)	Radial Location (r) (cm)	Axial Velocity (V _z) (cm/sec)
1.0	0.053*	11.10
	0.051	11.09
	0.045	11.00
	0.055*	11.00
	0.057*	10.97
	0.058*	10.20
	0.062	9.80
	0.074	8.80
	0.080	7.86
	0.084*	7.65
	0.084	7.40
	0.094	5.60
	0.101	5.53
	0.108	3.35
2.0	0.010	11.53
	0.015*	11.13
	0.011	10.97
	0.018	10.72
	0.025*	10.65
	0.021	10.65
	0.019*	10.64
	0.031*	10.15

Continued.....

TABLE C-2 (continued)

Axial Location (z/D) (No. of Dia.)	Radial Location (r) (cm)	Axial Velocity (V _z) (cm/sec)
2.0	0.032*	10.00
	0.038*	9.80
	0.041*	9.80
	0.050*	9.70
	0.040	9.60
	0.032	9.60
	0.048*	9.60
	0.031	9.50
	0.060*	9.20
	0.046*	9.20
	0.065*	9.00
	0.056	9.00
	0.062*	8.95
	0.052	8.60
	0.065*	8.40
	0.068	7.79
	0.083	6.95
	0.085	6.53
	0.095*	5.90
	0.094	5.78
	0.103	4.55
	0.107	4.46

Continued.....

TABLE C-2 (continued)

Axial Location (z/D) (No. of Dia.)	Radial Location (r) (cm)	Axial Velocity (V _z) (cm/sec)
2.0	0.114	3.05
3.0	0.011	9.55
	0.018*	9.41
	0.015*	8.88
	0.022*	8.77
	0.027*	8.75
	0.023	8.75
	0.019	8.63
	0.033*	8.40
	0.047*	8.28
	0.054*	8.14
	0.035*	8.05
	0.044*	8.00
	0.034	8.00
	0.033	7.92
	0.043	7.80
	0.052*	7.80
	0.052*	7.60
	0.067*	7.50
	0.072*	7.25
	0.063	7.20
	0.069*	7.10

Continued.....

TABLE C-2 (continued)

Axial Location (z/D) (No. of Dia.)	Radial Location (r) (cm)	Axial Velocity (Vz) (cm/sec)
3.0	0.073*	6.80
	0.061	6.75
	0.075	6.10
	0.093	5.30
	0.092	5.25
	0.106*	4.70
	0.103	4.43
	0.111	3.93
	0.112	3.63
	0.120	2.80

TABLE C-3

Diameter: 0.20 cm I.D.

Flow Rate: 0.6392 cm³/sec

Axial Location (z/D) (No. of Dia.)	Radial Location (r) (cm)	Axial Velocity (V _z) (cm/sec)
0.0	0.000	32.30
	0.008*	31.00
	0.011*	30.00
	0.048*	26.50
	0.038	25.90
	0.051*	25.00
	0.056	23.00
	0.065	22.60
	0.068	21.70
	0.071	21.00
	0.074	20.30
	0.071*	20.00
	0.068	19.00
	0.084	15.10
	0.093*	11.20
	0.100	5.50
1.0	0.000	28.01
	0.010	27.52
	0.011*	26.86
	0.012*	26.45

Continued.....

TABLE C-3 (continued)

Axial Location (z/D) (No. of Dia.)	Radial Location (r) (cm)	Axial Velocity (Vz) (cm/sec)
1.0	0.003*	26.16
	0.027	25.39
	0.031*	25.39
	0.021	25.39
	0.032*	24.73
	0.035	24.57
	0.039*	23.00
	0.053*	23.00
	0.053	22.19
	0.059*	21.60
	0.057	20.50
	0.054*	20.31
	0.068	19.00
	0.072	18.50
	0.075	17.85
	0.074	17.42
	0.075*	17.40
	0.081	17.36
	0.077	16.30
	0.091	13.10
	0.097*	10.25
	0.105	5.02

Continued.....

TABLE C-3 (continued)

Axial Location (z/D) (No. of Dia.)	Radial Location (r) (cm)	Axial Velocity (V _z) (cm/sec)
2.0	0.000	24.40
	0.012	23.40
	0.014*	23.00
	0.015*	22.93
	0.004*	22.65
	0.032*	22.00
	0.023	21.95
	0.026	21.60
	0.036*	21.29
	0.038	21.29
	0.043*	20.20
	0.058*	19.70
	0.056	19.25
	0.066*	18.50
	0.063	17.99
	0.059*	17.80
	0.080	15.80
	0.081	15.70
	0.081	15.20
	0.081	15.05
	0.078*	14.80
	0.084	13.70
	0.096	11.50

Continued.....

TABLE C-3 (continued)

Axial Location (z/D) (No. of Dia.)	Radial Location (r) (cm)	Axial Velocity (V _z) (cm/sec)
2.0	0.101*	9.20
	0.110	4.83
3.0	0.000	21.10
	0.018*	19.60
	0.017*	19.60
	0.013	19.50
	0.006*	19.25
	0.025	18.80
	0.039*	18.70
	0.041	18.50
	0.031	18.43
	0.040*	18.30
	0.046*	17.35
	0.064*	16.79
	0.059	16.54
	0.072*	15.72
	0.066	15.60
	0.061*	15.60
	0.088	13.00
	0.083	13.00
	0.083*	12.53
	0.090	11.50

Continued.....

TABLE C-3 (continued)

Axial Location (z/D) (No. of Dia.)	Radial Location (r) (cm)	Axial Velocity (V _z) (cm/sec)
3.0	0.095	11.10
	0.096	10.50
	0.102	10.10
	0.104*	8.19
	0.115	4.25

TABLE C-4

Diameter: 0.30 cm I.D.

Flow Rate: 0.1598 cm³/sec

Axial Location (z/D) (No. of Dia.)	Radial Location (r) (cm)	Axial Velocity (V _z) (cm/sec)
0.0	0.010	3.56
	0.011	3.50
	0.021	3.50
	0.033	3.32
	0.049	3.32
	0.029	3.31
	0.034*	3.08
	0.042*	3.07
	0.057	2.97
	0.070*	2.77
	0.068	2.63
	0.077	2.57
	0.053*	2.55
	0.073	2.53
	0.074*	2.45
	0.077*	2.36
	0.105*	2.15
	0.108	2.15
	0.085*	2.15
	0.098	2.06
	0.100	2.04

Continued.....

TABLE C-4 (continued)

Axial Location (s/D) (No. of Dia.)	Radial Location (r) (cm)	Axial Velocity (V _z) (cm/sec)
0.0	0.088*	1.98
	0.087*	1.97
	0.116	1.88
	0.100*	1.83
	0.106*	1.80
	0.109*	1.59
	0.121	1.53
	0.119	1.44
	0.116*	1.38
	0.125	1.23
	0.126*	1.13
	0.139*	0.91
	0.141	0.89
	0.142	0.78
	0.150*	0.63
1.0	0.016	1.81
	0.028	1.73
	0.057*	1.60
	0.017	1.60
	0.045	1.60
	0.049	1.60
	0.075	1.53

Continued.....

TABLE C-4 (continued)

Axial Location (z/D) (No. of Dia.)	Radial Location (r) (cm)	Axial Velocity (V _z) (cm/sec)
1.0	0.060*	1.50
	0.083	1.47
	0.051*	1.47
	0.108	1.35
	0.084*	1.33
	0.103	1.30
	0.105*	1.27
	0.121	1.26
	0.114*	1.22
	0.134*	1.10
	0.123*	1.09
	0.135*	1.05
	0.145*	1.02
	0.153	1.01
	0.154	1.00
	0.166*	0.90
	0.170	0.90
	0.158*	0.90
	0.166*	0.88
	0.168*	0.82
	0.181	0.78
	0.188	0.77
	0.182*	0.75

Continued.....

TABLE C-4 (continued)

Axial Location (z/D) (No. of Dia.)	Radial Location (r) (cm)	Axial Velocity (V _z) (cm/sec)
1.0	0.184*	0.72
	0.198	0.69
	0.194*	0.65
	0.203*	0.52
	0.214	0.50
	0.214*	0.48
	0.216*	0.41
2.0	0.026	0.85
	0.070	0.72
	0.090*	0.70
	0.028	0.70
	0.077	0.70
	0.044	0.68
	0.095*	0.67
	0.079*	0.67
	0.130	0.63
	0.117	0.63
	0.132*	0.60
	0.161	0.57
	0.171	0.55
	0.166*	0.52
	0.179*	0.47

Continued.....

TABLE C-4 (continued)

Axial Location (z/D (No. of Dia.))	Radial Location (r) (cm)	Axial Velocity (V _z) (cm/sec)
2.0	0.191*	0.45
	0.210*	0.45
	0.227*	0.45
	0.240	0.42
	0.244	0.42
	0.212*	0.41
	0.259*	0.37
	0.260*	0.36
	0.247*	0.35
	0.293	0.34
	0.308	0.32
	0.280*	0.30
	0.300*	0.30
	0.316*	0.26
	0.328	0.25
	0.328*	0.24
	0.329*	0.23

TABLE C-5

Diameter: 0.30 cm I.D.

Flow Rate: 0.3196 cm³/sec

Axial Location (z/D) (No. of Dia.)	Radial Location (r) (cm)	Axial Velocity (V _z) (cm/sec)
0.0	0.000	7.33
	0.010	7.33
	0.005*	7.26
	0.020	7.10
	0.013*	7.01
	0.011*	7.00
	0.030*	6.89
	0.020	6.85
	0.051	6.60
	0.028	6.30
	0.027*	6.30
	0.074	6.20
	0.069	6.10
	0.038*	6.07
	0.045	6.07
	0.076	5.90
	0.064*	5.90
	0.070	5.90
	0.071*	5.65
	0.065*	5.64
	0.085	5.57

Continued.....

TABLE C-5 (continued)

Axial Location (z/D) (No. of Dia.)	Radial Location (r) (cm)	Axial Velocity (V _z) (cm/sec)
0.0.	0.082	5.38
	0.092	5.37
	0.082*	4.95
	0.096	4.70
	0.083*	4.70
	0.088*	4.68
	0.110*	4.54
	0.094*	4.38
	0.094*	4.35
	0.111*	3.68
	0.118*	3.22
	0.143*	2.43
1.0	0.150	1.65
	0.000	4.81
	0.013	4.80
	0.006*	4.71
	0.019*	4.65
	0.011	4.64
	0.017*	4.58
	0.022	4.58
	0.016*	4.50
	0.023	4.40

Continued.....

TABLE C-5 (continued)

Axial Location (z/D) (No. of Dia.)	Radial Location (r) (cm)	Axial Velocity (Vz) (cm/sec)
1.0	0.146*	2.36
	0.158*	2.20
	0.176*	1.70
	0.186	1.29
2.0	0.000	2.97
	0.017	2.94
	0.009*	2.83
	0.019*	2.75
	0.029	2.70
	0.021*	2.60
	0.030	2.54
	0.046*	2.51
	0.067*	2.50
	0.083	2.50
	0.042	2.42
	0.102*	2.42
	0.077	2.40
	0.044*	2.34
	0.108	2.30
	0.115	2.20
	0.121	2.18
	0.115*	2.18

Continued.....

TABLE C-5 (continued)

Axial Location (z/D) (No. of Dia.)	Radial Location (r) (cm)	Axial Velocity (V _z) (cm/sec)
1.0	0.035*	4.30
	0.062	4.25
	0.051*	4.10
	0.034	4.08
	0.035*	4.02
	0.076*	3.97
	0.058	3.96
	0.083	3.92
	0.098	3.83
	0.088	3.76
	0.096	3.75
	0.088*	3.69
	0.106	3.61
	0.107	3.41
	0.120*	3.32
	0.114	3.22
	0.105*	3.12
	0.108*	3.10
	0.111*	3.00
	0.127	2.88
	0.124*	2.82
	0.123*	2.65
	0.147*	2.42

Continued.....

TABLE C-5 (continued)

Axial Location (z/D) (No. of Dia.)	Radial Location (r) (cm)	Axial Velocity (V _z) (cm/sec)
2.0	0.136	2.14
	0.123	2.14
	0.140	1.92
	0.159*	1.92
	0.138*	1.88
	0.137*	1.77
	0.147	1.76
	0.162*	1.70
	0.162	1.60
	0.188*	1.48
	0.201*	1.40
	0.188*	1.40
	0.226*	1.18
3.0	0.236	0.94
	0.020	1.74
	0.000	1.64
	0.027*	1.58
	0.041	1.52
	0.061	1.46
	0.107	1.43
	0.092	1.39
	0.113	1.39

Continued.....

TABLE C-5 (continued)

Axial Location (z/D) (No. of Dia.)	Radial Location (r) (cm)	Axial Velocity (V _z) (cm/sec)
3.0	0.032*	1.35
	0.137*	1.33
	0.041	1.31
	0.157	1.24
	0.144	1.24
	0.169	1.21
	0.060*	1.21
	0.161*	1.18
	0.185*	1.05
	0.191*	1.03
	0.173	1.02
	0.218*	0.96
	0.268*	0.87
	0.321	0.67

TABLE C-6

Diameter: 0.30 cm I.D.

Flow Rate: 0.6392 cm³/sec

Axial Location (z/D) (No. of Dia.)	Radial Location (r) (cm)	Axial Velocity (V _z) (cm/sec)
0.0	0.000	14.50
	0.007	14.50
	0.005	14.45
	0.022	14.40
	0.007	14.40
	0.030	14.00
	0.042	13.90
	0.037	13.80
	0.027*	13.75
	0.042*	13.40
	0.044	13.30
	0.042	13.00
	0.045*	12.85
	0.061*	12.45
	0.058	12.40
	0.076	12.20
	0.064*	12.00
	0.061*	11.95
	0.075	11.90
	0.064*	11.75
	0.083	10.45

Continued.....

TABLE C-6 (continued)

Axial Location (z/D) (No. of Dia.)	Radial Location (r) (cm)	Axial Velocity (V _z) (cm/sec)
0.0	0.085*	10.45
	0.074*	10.40
	0.086	10.20
	0.096	10.00
	0.089*	9.95
	0.110	7.35
	0.115	7.20
	0.104*	7.05
	0.110*	6.95
	0.115*	6.75
	0.118*	6.52
	0.121*	5.80
	0.132*	4.40
	0.142*	3.65
	0.150*	2.70
1.0	0.000	10.82
	0.010	10.81
	0.008	10.80
	0.000	10.75
	0.010	10.60
	0.024	10.48
	0.032	10.48

Continued.....

TABLE C-6 (continued)

Axial Location (z/D) (No. of Dia.)	Radial Location (r) (cm)	Axial Velocity (V _z) (cm/sec)
1.0	0.032*	10.30
	0.041	10.24
	0.046	10.20
	0.052	10.02
	0.051	10.00
	0.048*	9.90
	0.052	9.83
	0.047*	9.80
	0.053*	9.60
	0.076	9.28
	0.089	9.25
	0.066	8.90
	0.072*	8.80
	0.087	8.70
	0.075*	8.60
	0.080*	8.30
	0.099	7.70
	0.086*	7.70
	0.099*	7.60
	0.107*	7.45
	0.114	7.40
	0.120	7.20
	0.127*	5.45

Continued

TABLE C-6 (continued)

Axial Location (z/D) (No. of Dia.)	Radial Location (r) (cm)	Axial Velocity (Vz) (cm/sec)
1.0	0.137	5.41
	0.139	5.40
	0.125*	5.20
	0.137*	5.20
	0.145*	4.95
	0.140*	4.80
	0.147*	4.35
	0.154*	3.30
	0.165*	2.70
	0.172*	2.30
2.0	0.000	7.95
	0.010	7.80
	0.000	7.80
	0.038	7.66
	0.013	7.60
	0.012	7.60
	0.040*	7.50
	0.045	7.42
	0.054	7.40
	0.029	7.40
	0.051	7.30
	0.056*	7.10

Continued

TABLE C-6 (continued)

Axial Location (z/D) (No. of Dia.)	Radial Location (r) (cm)	Axial Velocity (V _z) (cm/sec)
2.0	0.062	7.00
	0.061	7.00
	0.061*	6.99
	0.057*	6.87
	0.089	6.80
	0.101	6.66
	0.078	6.25
	0.084*	6.20
	0.096*	6.15
	0.096*	5.86
	0.101*	5.60
	0.131*	5.50
	0.118	5.49
	0.119*	5.40
	0.131	5.03
	0.141	4.91
	0.150*	4.00
	0.166	4.00
	0.161*	3.80
	0.156	3.80
	0.175*	3.71
	0.164*	3.54
	0.172*	3.12

Continued.....

TABLE C-6 (continued)

Axial Location (z/D) (No. of Dia.)	Radial Location (r) (cm)	Axial Velocity (V _z) (cm/sec)
2.0	0.177*	2.59
	0.189*	2.05
	0.196*	1.91
3.0	0.000	5.86
	0.013	5.86
	0.000	5.75
	0.042	5.62
	0.012	5.60
	0.048*	5.49
	0.061	5.47
	0.070*	5.34
	0.054	5.26
	0.064	5.24
	0.015	5.20
	0.032	5.00
	0.069*	5.00
	0.107	4.99
	0.074	4.95
	0.070*	4.78
	0.073	4.70
	0.121	4.66
	0.094	4.64

Continued.....

TABLE C-6 (continued)

Axial Location (z/D) (No. of Dia.)	Radial Location (r) (cm)	Axial Velocity (V _z) (cm/sec)
3.0	0.117*	4.53
	0.100*	4.46
	0.111*	4.28
	0.153*	4.20
	0.122*	4.00
	0.144*	3.95
	0.138	3.80
	0.153	3.32
	0.170	3.30
	0.178*	2.91
	0.213*	2.87
	0.194*	2.66
	0.194*	2.66
	0.190	2.60
	0.210*	2.25
	0.226*	1.90
	0.232*	1.60

C.2 Centerline Velocities

Contained in this section are the axial velocities at the flow centerline determined from the plots of the axial velocity profiles such as Figures (IV-1) and (IV-2) at several upstream axial locations and for various flow rates. For example, considering the 0.30 cm I.D. capillary tube at flow rate $0.6392 \text{ cm}^3/\text{sec}$ and at axial location of two diameters ($z/D = 2$), the data points are plotted in Figure (IV-2). By drawing an eye-fit solid line through the data points, the centerline velocity was estimated at $\gamma = 0$ and was found to be 7.95 cm/sec . This is the value tabulated in Table (C-7).

For the axial locations where a complete velocity profile was not measured, the centerline velocities were determined by the same procedure except the incomplete velocity profiles near the centerline were used instead of the complete profiles.

TABLE C-7

Diameter (cm)	Flow Rate (cm ³ /sec)	Axial Location (z/D) (No. of Dia.)	Centerline Velocity (V _z , cm/sec)
0.20	0.1598	0.0	8.25
		0.5	7.32
		1.0	6.38
		1.5	5.52
		2.0	4.85
		2.5	4.00
		3.0	3.60
	0.3196	0.0	16.30
		0.5	15.00
		1.0	13.80
		1.5	12.60
		2.0	11.53
		2.5	10.40
		3.0	9.55
	0.6392	0.0	32.30
		0.5	30.30
		1.0	28.01
		2.0	24.40
		3.0	21.10
		4.0	18.00

Continued.....

TABLE C-7 (continued)

Diameter (cm)	Flow Rate (cm ³ /sec)	Axial Location (z/D) (No. of Dia.)	Centerline Velocity (V _z , ft) (cm/sec)
0.20	0.6392	5.0	15.50
		6.0	13.40
		7.0	11.55
0.30	0.1598	0.0	3.60
		0.5	2.52
		1.0	1.85
		1.5	1.26
		2.0	0.85
	0.3196	0.0	7.33
		0.5	6.01
		1.0	4.75
		1.5	3.75
		2.0	3.00
	0.6392	2.5	2.26
		3.0	1.80
		0.0	14.50
		0.5	12.55
		1.0	10.82
		1.5	9.15

Continued.....

TABLE C-7 (continued)

Diameter (cm)	Flow Rate (cm ³ /sec)	Axial Location (z/D) (No. of Dia.)	Centerline Velocity (V _{z,¢}) (cm/sec)
0.30	0.6392	2.0	7.95
		2.5	6.75
		3.0	5.86

APPENDIX D

CONE ANGLES AND CENTRAL CORE DIAMETERS

The cone semi-angle was defined in Chapter III, Section III.3-3b, as the angle formed by the line tangent to the outermost streamline that enters into the capillary tube. The cone semi-angles which were measured in degrees and the central core diameters which were measured in centimeters are tabulated in Table (D-1) for the 0.20 and 0.30 cm I.D. capillary tubes at several axial locations upstream of the contraction. The initial cone semi-angle (ϕ_0) was defined as the cone semi-angle at the contraction ($z/D = 0$).

TABLE D-1

Diameter (cm)	Flow Rate (cm ³ /sec)	Axial Location (z/D) (No. of Dia.)	Central Core Diameter (d) (cm)	Cone Semi-Angle(ϕ) (degrees)
0.20	0.1598	0.0	0.200	3.70
		1.0	0.220	4.10
		2.0	0.240	4.40
		3.0	0.276	5.30
		4.0	0.316	6.60
		5.0	0.364	9.70
		6.0	0.434	12.60

Continued....

TABLE D-1 (continued)

Diameter (cm)	Flow Rate (cm ³ /sec)	Axial Location (z/D) (No. of Dia.)	Central Core Diameter (d) (cm)	Cone Semi-Angle (ϕ) (degrees)
0.20	0.3196	0.0	0.200	2.30
		1.0	0.215	2.50
		2.0	0.228	2.60
		3.0	0.239	2.80
		4.0	0.261	3.20
		5.0	0.281	3.70
		6.0	0.305	4.30
		7.0	0.337	5.20
	0.6392	0.0	0.200	1.60
		1.0	0.209	1.66
		2.0	0.219	1.73
		3.0	0.230	1.84
		4.0	0.241	2.10
		5.0	0.255	2.40
		6.0	0.268	2.80
		7.0	0.287	3.30
0.30	0.1598	0.0	0.300	9.40
		0.5	0.363	11.80
		1.0	0.432	15.10
		1.5	0.526	19.40
		2.0	0.657	26.00

Continued.....

TABLE D-1 (continued)

Diameter (cm)	Flow Rate (cm ³ /sec)	Axial Location (z/D) (No. of Dia.)	Central Core Diameter (d) (cm)	Cone Semi-Angle (ϕ) (degrees)
0.30	0.3196	0.0	0.300	6.20
		0.5	0.333	7.50
		1.0	0.372	8.00
		1.5	0.416	9.20
		2.0	0.472	11.80
		2.5	0.546	15.30
		3.0	0.642	22.90
	0.6392	0.0	0.300	4.10
		0.5	0.325	4.50
		1.0	0.344	4.70
		1.5	0.369	4.90
		2.0	0.392	5.60
		2.5	0.424	6.60
		3.0	0.464	7.60
		3.5	0.503	9.40
		4.0	0.560	11.30

APPENDIX E
STRETCH RATES ALONG CENTERLINE

The stretch rates along the centerline were measured as the slope of the plot of axial centerline velocities ($V_z, \text{cm/sec}$) versus the axial locations (z). The data which were measured are tabulated in Table (E-1) at several axial locations upstream of the contraction.

TABLE E-1

Diameter (cm)	Flow Rate (cm^3/sec)	Axial Location (z/D) (No. of Dia.)	Centerline Stretch Rate (sec^{-1})
0.20	0.1598	0.5	- 10.39
		1.0	- 9.16
		1.5	- 8.12
		2.0	- 7.13
		2.5	- 6.06
		3.0	- 5.14
	0.3196	0.5	- 13.33
		1.0	- 12.57
		1.5	- 11.45
		2.0	- 10.81
		2.5	- 9.78
		3.0	- 8.99

Continued.....

TABLE E-1 (continued)

Diameter (cm)	Flow Rate (cm ³ /sec)	Axial Location (z/D) (No. of Dia.)	Centerline Stretch Rate (sec ⁻¹)
0.20	0.6392	0.5	- 21.71
		1.0	- 20.63
		2.0	- 17.96
		3.0	- 15.64
		4.0	- 13.61
		5.0	- 11.60
		6.0	- 10.00
		7.0	- 7.75
0.30	0.1598	0.5	- 5.89
		1.0	- 4.43
		1.5	- 3.11
		2.0	- 2.26
	0.3196	0.5	- 9.23
		1.0	- 7.57
		1.5	- 6.05
		2.0	- 4.94
		2.5	- 3.57
		3.0	- 2.60

Continued.....

TABLE E-1 (continued)

Diameter (cm)	Flow Rate (cm ³ /sec)	Axial Location (z/D) (No. of Dia.)	Centerline Stretch Rate (sec ⁻¹)
0.30	0.6392	0.5	- 12.84
		1.0	- 11.24
		1.5	- 9.61
		2.0	- 8.19
		2.5	- 6.86
		3.0	- 5.62

APPENDIX F

SAMPLE CALCULATION

Contained in this section is a sample calculation which converts the measured streak length into axial velocity. For example, consider the following:

$$\begin{aligned}
 \text{I. D. of capillary tube} &= 0.30 \text{ cm} \\
 \text{flow rate} &= 0.3196 \text{ cm}^3/\text{sec} \\
 \text{rotational speed of the 20 slits and spokes chopping disc} \\
 &= 242 \text{ R.P.M.} \\
 \text{magnification of streaks project onto the graph paper} \\
 &= 47.8
 \end{aligned}$$

Typical streak lengths along several streamlines for this run were shown in Figure (III-6). Consider the streamline number 8 in Figure (III-6) at the axial location of one diameter ($z/D = 1$).

- (i) The streak lengths were measured by using the leading edge to leading edge technique or distance A to B.



In this case the length of AB was equal to 3.70 cm on the graph paper. Then the length of streak (ΔL) at this axial location can be found by dividing this value by 2.

$$\Delta L = \frac{3.70}{2} = 1.85 \text{ (cm)}$$

- (ii) The time interval for this example can be calculated by using the following Equation (G-1)

$$\bar{t} = \frac{60}{N\omega} \text{ sec} \quad (\text{G-1})$$

where

N = number of slit and spokes on the chopping disc

ω = number of revolution per minute.

Therefore,

$$\begin{aligned} \bar{t} &= \frac{60}{20 \times 242} \\ &= 0.0124 \text{ sec} \end{aligned}$$

- (iii) By using Equation (III-1), the axial velocity can be calculated.

$$V_z = \frac{\Delta L}{M\bar{t}} \quad (\text{III-1})$$

where

ΔL = length of streak

M = magnification of streaks on the graph paper

\bar{t} = time for the slit to cut the beam of light

Therefore,

$$\begin{aligned} V_z &= \frac{1.85}{47.8 \times 0.0124} \\ &= 3.12 \text{ cm/sec} \end{aligned}$$

This axial velocity was plotted in Figure (III-7) and also tabulated in Appendix C, Table (C-5).

B30171